Department Chemie und Pharmazie

FRIEDRICH-ALEXANDER UNIVERSITÄT ERLANGEN-NÜRNBERG
NATURWISSENSCHAFTLICHE FAKULTÄT

Reactions of Porphyrin Molecules and Anchor Groups on Single-Crystal Surfaces

Reaktionen von Porphyrinen und Ankergruppen auf Einkristalloberflächen

Der Naturwissenschaftlichen Fakultät der
Friedrich-Alexander-Universität Erlangen-Nürnberg

zur Erlangung des Doktorgrades Dr. rer. nat.

vorgelegt von

Julia Köbl

Department Chemie und Pharmazie

FRIEDRICH-ALEXANDER UNIVERSITÄT ERLANGEN-NÜRNBERG
NATURWISSENSCHAFTLICHE FAKULTÄT

Reactions of Porphyrin Molecules and Anchor Groups on Single-Crystal Surfaces

Reaktionen von Porphyrinen und Ankergruppen auf Einkristalloberflächen

Der Naturwissenschaftlichen Fakultät der

Friedrich-Alexander-Universität Erlangen-Nürnberg

zur Erlangung des Doktorgrades Dr. rer. nat.

vorgelegt von

Julia Köbl

Als Dissertation genehmigt von der

Naturwissenschaftlichen Fakultät

der Friedrich-Alexander-Universität Erlangen-Nürnberg

Tag der mündlichen Prüfung: 11.03.2022

Vorsitzende Person des

Promotionsorgans: Prof. Dr. Andrea Büttner

Gutachter/in: PD Dr. Ole Lytken

Prof. Dr. Oliver Diwald

Contents

1. Introduction

Porphyrins play a central role in many essential processes in nature, and the most prominent examples of porphyrins are chlorophyll a and heme b, depicted in Figure 1. Chlorophyll is a green natural pigment consisting of a magnesium(II) porphyrin derivative and it is responsible for light absorption and electron transfer in photosynthesis. Heme b in comparison is an iron(II) porphyrin complex and a central component of hemoglobin. Hemoglobin is responsible for the oxygen transport in blood, and thus for the respiration process of almost all vertebrates [1-3].

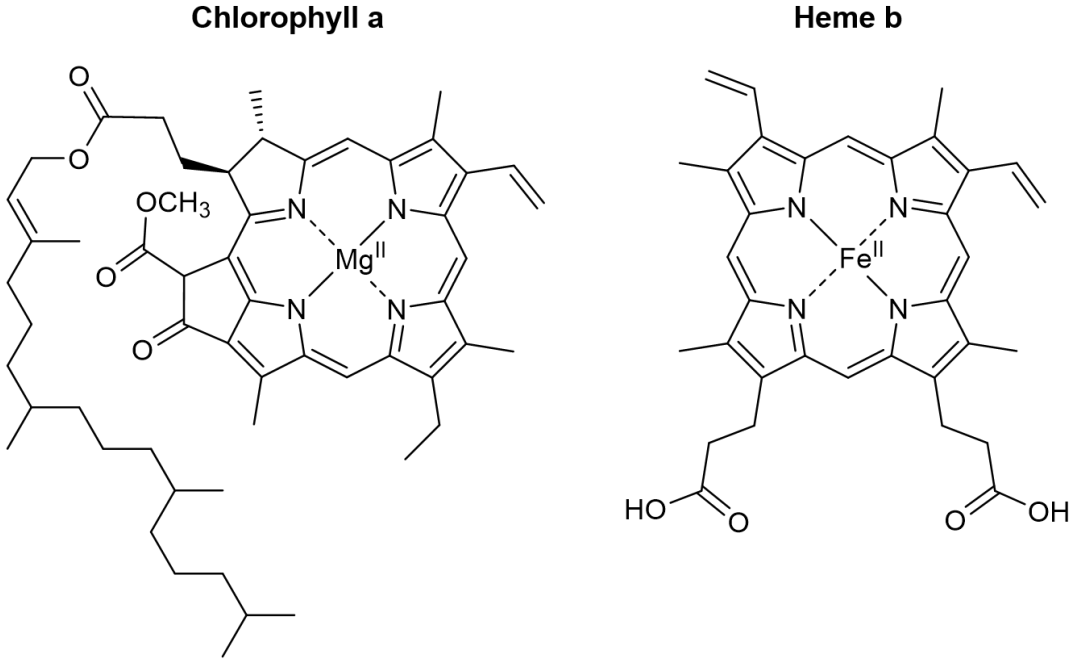

Figure 1 Two prominent examples of the natural occurrence of porphyrins: Chlorophyll a is the molecule responsible for light absorption, and electron transport in photosynthesis, and heme b is one of the main components of hemoglobin.

The role of porphyrins in nature and their interesting characteristics such as structural versatility and stability inspired many researchers to apply them in a wide field of applications, such as dye-sensitized solar cells (DSSCs), organic light-emitting diodes (OLEDs) and organic-field effect transistors (OFETs). The use of dye-sensitized solar cells as a renewable energy source is one promising approach to face the challenge of environmental problems with all its severe consequences. Porphyrins are interesting as dye molecules because of their strong colors and were for instance used in dye-sensitized solar cells, also referred to as Grätzel cells [4-11].

The central unit of a porphyrin molecule is the porphine core. As depicted in Figure 2, this porphine unit consists of four pyrrole rings interconnected by methine bridges. At these methine bridges, functional groups of different complexity can be attached. In the simplest case hydrogen atoms

are present. Still comparably simple is the attachment of four phenyl rings. In that case, the molecule is called tetraphenylporphyrin and this is probably the most-studied porphyrin molecule in Surface Science [12, 13]. Metalation is one straight-forward and often used method to tailor the chemical and electrical properties of a porphyrin, beside the already mentioned introduction of peripheral functional groups. In the metalated molecule, the two central protons of the free-base molecule have been replaced by a metal ion typically in oxidation state +2. Metalation can happen on a surface by co-deposition of reactive metal atoms or through a reaction directly with substrate atoms also called self-metalation [12-20].

For many applications, the porphyrin molecules need to be supported on solid substrates. In the dye-sensitized solar cell for instance [9, 21] porphyrin molecules are bonded to the titania substrate using anchor groups that form covalent bonds between the dye and the surface. The anchor groups are responsible for the charge transfer to the titania substrate, and they are therefore critical for the performance of the solar cell. Many different functional groups can be used as anchor groups, for example carboxylic acids (-C(=O)(OH)), phosphonic acids ($-P(=O)(OH)_2$), hydroxamic acids (-(C=O)-NH(OH)) or cyano (-CN) groups [22-24].

However, dye-sensitized solar cells are still not as efficient and reliable as silicon-based solar cells [25, 26]. In particular, the long-term stability needs to be improved [27, 28]. One approach when faced with a very complex problem is to look at all the subcomponents individually, understand each of them better and then improve them one at a time. So, the first step is understanding these subcomponents in detail: For dye-sensitized solar cells the dye-semiconductor interface can be considered as one subcomponent, affecting quantum efficiency, open circuit voltage and the long-term stability of the device. In the Grätzel solar cell, this is the interface between the porphyrin molecules and titanium dioxide [4, 6, 9]. Surfaces of powders and nanoparticles are complex and expose many different crystal facets. In Surface Science this complexity is reduced by studying only a single crystal facet at a time. By understanding these simpler, but often still complex, surfaces, we as researchers are able to understand elementary steps of chemical reactions and processes on surfaces on an atomic level. This knowledge can then be combined with knowledge from the other subcomponents to learn about the behavior of more complex surfaces and interfaces. At the end of these learning processes, we end up with a deep understanding of the important properties of the systems, and this will help us to design new materials and guide the design decisions by a knowledge-based approach instead of trial-and-error.

This thesis is very much focused on this approach where complex systems are split up into smaller, simpler subcomponents: The surfaces studied are single-crystal surfaces, exposing only a single crystal facet, and even the functionalized porphyrin molecules are split into subcomponents and

the anchor group and the porphyrin molecule studied separately. The thesis covers three main topics: (1) Cyano porphyrins on Cu(111), (2) tetraphenylporphyrin on TiO_2(110) and (3) phosphonic and hydroxamic anchor groups on TiO_2(110). Cu(111) is a much simpler surface than TiO_2(110) and is therefore a good surface to start with. In Chapter 3.1, we focused on the copper surface and the effect of cyano groups on the adsorption structure of porphyrins. Further, we studied the effect of the adsorption structure on the self-metalation reaction of cyano porphyrins deposited onto the surface. For Chapter 3.2, the self-metalation reaction of the porphyrin molecule with the TiO_2(110) surface was observed upon annealing, and in addition protonation of the tetraphenylporphyrin was observed at room temperature. In Chapter 3.3.1 and 3.3.2, the bond formation of two anchoring groups, phosphonic acid and hydroxamic acid, to the TiO_2(110) surface was investigated as a function of coverage and temperature.

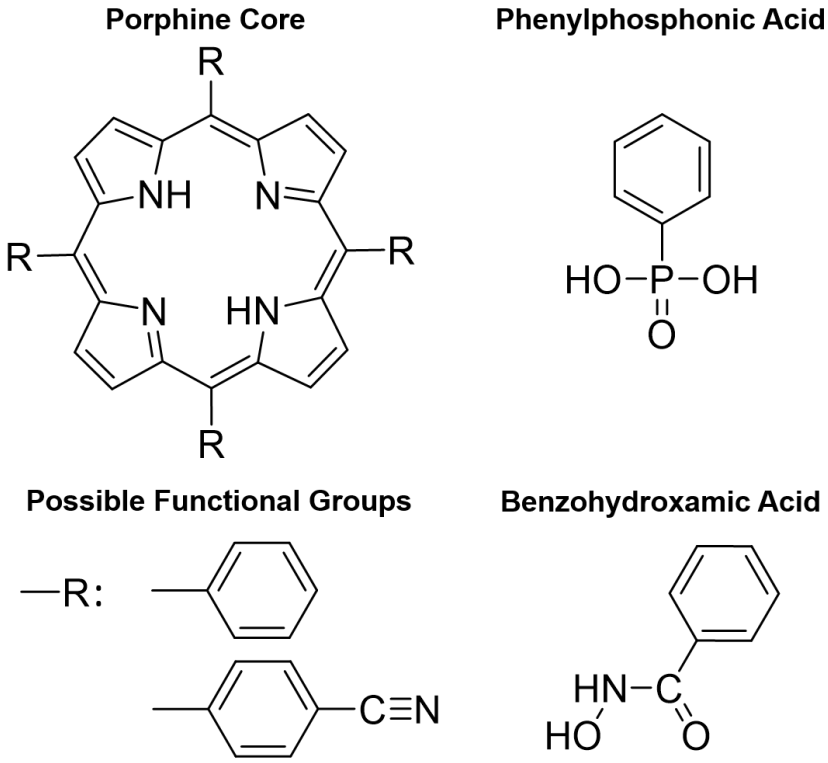

Figure 2 Molecular drawings of the studied molecules. The porphine core is depicted with four groups at the methine bridges. Different functional groups could be attached such as the examples phenyl rings or phenyl rings para-substituted with cyano groups. Further, molecular drawings of the two studied molecules with the respective anchor groups, namely the phosphonic acid and the hydroxamic acid, are shown.

2. Experimental and Methodology Section

All experiments in this work were performed in ultrahigh-vacuum (UHV) chambers. The concept of UHV is described in Chapter 2.1 and visualized by comparison of two important descriptive physical values, the impingement rate and the time it takes to build up a monolayer on a surface. In Chapter 2.2, the UHV setups are briefly presented, especially pointing out their outstanding features and benefits. In Chapter 2.3 and 2.4, Cu(111) and TiO_2(110), and how to prepare the respective surfaces are introduced. Sample mounting and how to acquire accurate temperatures for the TiO_2(110) crystals is also summarized in Chapter 2.4. The following Chapter 2.5 describes the molecules that were used and how to deposit them. In the last Chapter, 2.6, the experimental techniques used in this thesis are presented, including the most important fundamental principles of each.

2.1. Experimental Conditions - Ultrahigh Vacuum

All experiments in this work were performed in ultrahigh-vacuum chambers, implying that the pressure inside these chambers is below $1.0 \cdot 10^{-7}$ Pa or $1.0 \cdot 10^{-9}$ mbar. Using ultrahigh vacuum, a clean environment can be obtained and maintained in these UHV chambers. The importance of ultrahigh vacuum can be realized by calculating the flux of molecules hitting a wall or a surface in a certain time, also called the impingement rate. This impingement rate ${}^1Z_W$ is described by Equation 1 where p is the pressure, k_B Boltzmann's Constant, m the molecular mass and T the temperature [29].

$$ {}^1Z_W = p \cdot \sqrt{\frac{1}{2 \cdot \pi \cdot k_B \cdot m \cdot T}} \tag{1} $$

Table 1 lists the impingement rates for CO ($m = 4.65 \cdot 10^{-26}$ kg) at room temperature (293 K) and at three pressures: 1 bar corresponds to the ambient pressure outside an UHV chamber and 10^{-6} and 10^{-10} mbar are pressures typically found inside an UHV chamber.

If we assume a sticking probability of 1, meaning all molecules hitting the surface are adsorbed, and a typical density of sites on a surface (~10^{19} m^{-2}) we can calculate the time required until one full layer is formed on the surface, see Table 1. At ambient pressure only three nanoseconds are required to fully cover a surface with gas molecules, making it very clear why UHV chambers are required. Even at a pressure of 10^{-6} mbar it only takes three seconds to completely cover a clean

surface with one layer of CO. At a pressure of 10^{-10} mbar, however, it takes over 9 hours to fully cover a surface, enough time to perform our experiments.

Table 1 Impingement rates and the time t until one monolayer (1 ML) is formed are given for different pressures.

Pressure [mbar]	**Pressure [kg·m^{-1}·s^{-2} or Pa]**	**Impingement rate [s^{-1}m^{-2}]**	**Time t until 1 ML is formed [s]**
10^{3}	10^{5}	$2.9 \cdot 10^{27}$	$3.4 \cdot 10^{-9}$
10^{-6}	10^{-4}	$2.9 \cdot 10^{18}$	$3.4 \cdot 10^{0}$
10^{-10}	10^{-8}	$2.9 \cdot 10^{14}$	$3.4 \cdot 10^{4}$ (~9.5 h)

Noteworthy, the time frame of maintaining a clean sample is very important when it comes to experimental planning or data evaluation, especially when submonolayer coverages are to be investigated. Experimentalists often overestimate the time until the adsorption of relevant amount residual gas or contamination occurs. Assuming 9 h for a fully covered layer at 10^{-10} mbar, gives only roughly 1 h until 10% of a surface is covered by undesired contamination.

After baking the UHV setup to 130°C for several days while constantly pumping, the ion and turbo pumps of the chamber are able to maintain pressures $< 5 \cdot 10^{-10}$ mbar during the daily routine. Additional use of cryopumps showed promising results, decreasing the pressure to the 10^{-11} mbar range. This enable us to keep the amount of contamination neglectable even for submonolayer coverages and even after several hours of experiment.

2.2. The Ultrahigh-Vacuum Setups

Five different ultrahigh-vacuum setups were used in this work. (1), (2) and (3) are ultrahigh-vacuum chambers located in Erlangen. (1) The first chamber, at the Chair of Physical Chemistry II in Erlangen, has a base pressure below $5 \cdot 10^{-10}$ mbar and is equipped with a SES200 hemispherical energy analyzer, monochromatic Al Kα X-ray source, a quadrupole mass spectrometer and low-energy electron diffraction optics. Thus, X-ray photoelectron spectroscopy (XPS), low-energy electron diffraction (LEED), and temperature programmed desorption (TPD) can be combined to study sample properties such as surface structure, elemental surface compositions, and thermally-induced desorption products. In this thesis, LEED was used to confirm the (1 × 1) surface structure of TiO_2(110), being crucial for the following experiments, and XPS was applied to confirm the results obtained from the synchrotron and collect additional data, such as multilayer spectra. (2) The second setup at the Chair of Physical Chemistry II in Erlangen also has a base pressure in the low 10^{-10} mbar regime and is equipped with an RHK UHV VT STM 300 and RHK SPM 100 electronics. Applying STM, clean, large terraces, and thus a good quality of the surface, can be confirmed on the molecular scale. Offering local, molecular resolution, also parameters such as the adsorption geometry of different porphyrins molecules and island structures of deposited molecules can be investigated. These parameters are often investigated as a function of coverage and temperature. This setup also enables stabilized image acquisition of the same position over time, and thus, the movement of molecules can be acquired as short movies. (3) The third setup in Erlangen is the PHI Quantera II Scanning XPS Microprobe UHV chamber of the Helmholtz Institute Erlangen-Nuremberg and has a base pressure of $1 \cdot 10^{-9}$ mbar. The PHI Quantera II chamber is equipped with a monochromatic Al Kα X-ray source and a dual-beam charge neutralization setup. Applying neutralization, allows for the measurement of non-conductive samples, which is usually not possible with XPS. This allowed for several powders, such as benzohydroxamic acid and potassium benzohydroxamate, to be measured as reference samples in the context of this work. (4) The fourth setup was at the photoemission endstation U20 in the National Synchrotron Radiation Laboratory, in Hefei, China. The chamber is equipped with LEED optics, a twin anode (Mg and Al) X-ray source, and a VG SCIENTA R3000 electron analyzer, and has a base pressure below $3 \cdot 10^{-10}$ mbar. The chamber is connected to a bending magnet and it is equipped with three gratings that enable access to photon energies from 60 to 1000 eV with high energy resolution. However, at the time of the experiments, the photon flux was quite low for the higher photon energies, and thus the lab source (Al Kα) was mainly used for all experiments except for the valence-band measurements (not shown in the paper / unpublished results).

(5) The fifth setup was at the endstation of the Materials Science Beamline at synchrotron facility Elettra Sincrotrone in Trieste, Italy. The chamber base pressure is $2 \cdot 10^{-10}$ mbar or better, especially when using cryopumps. Furthermore, it has access to synchrotron radiation and is equipped with a SPECS PHOIBOS 150 hemispherical energy analyzer and LEED. One of the big advantages of synchrotron radiation is the high photon flux that enables fast measurements. Fast measurements have the advantage that contamination from the background gas becomes less important, and thus more data can be collected in a shorter time even on the same sample, for example on subsequent deposition of submonolayer coverages. The second, maybe even bigger advantage, is the tunability of the light source. Tuning the photon energy has many advantages such as that by using of smaller photon energies, smaller kinetic energies and thus higher surface sensitivity can be obtained. For more detailed information on surface sensitivity, the interested reader is referred to the Universal Curve as depicted with description in Chapter 2.6.1. In addition, further techniques, such as near-edge X-ray-absorption fine-structure spectroscopy (NEXAFS), can be applied utilizing the tunability of the photon energies. For a more detailed description on the principle of NEXAFS, please see Chapter 2.6.3.

A more detailed description on the different chambers is found in the respective publications and references therein.

2.3. Copper Single-Crystal Surface - Cu(111)

In this thesis, scanning tunneling microscopy (STM) experiments were performed on a Cu(111) surface. As shown in Figure 3, the crystal structure for copper is face-centered cubic with lattice parameter of 0.3615 nm at 293 K [26] and the close-packed (111) facet has nearest neighbor distances of 0.256 nm and a hexagonal structure. This is basic information, but it is extremely important when interpreting the adsorption and orientation of organic molecules from scanning tunneling microscopy images.

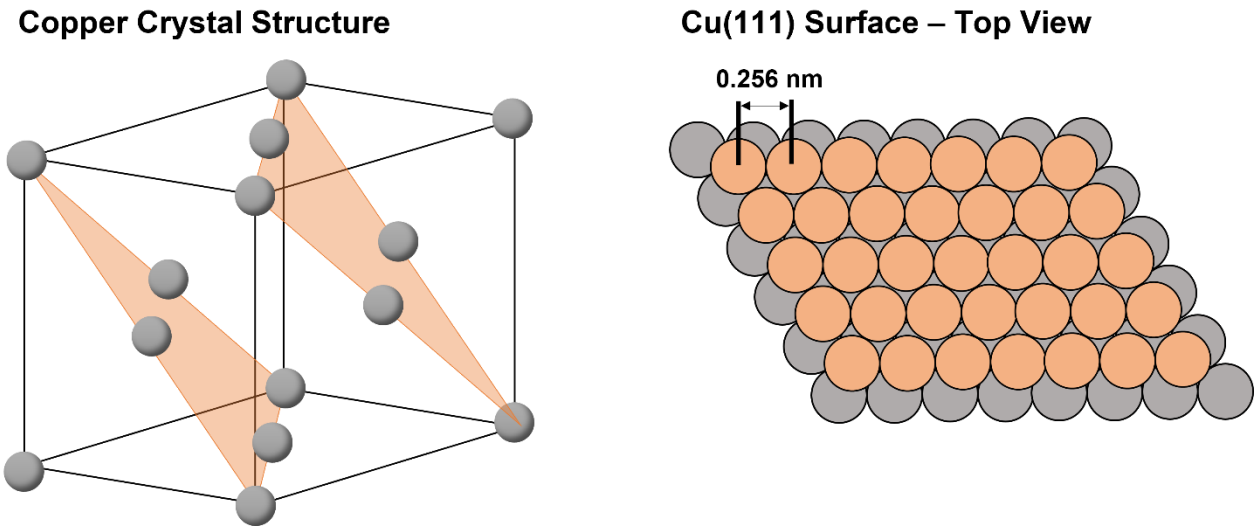

Figure 3 The face-centered cubic crystal structure of copper and a ball model of the Cu(111) surface with its typical hexagonal structure resulting in a three-fold symmetry.

The one-side-polished crystal was purchased by MaTeck and cleaned by Ar^+ sputtering and annealing to 850 K in ultrahigh vacuum. The crystal temperature was acquired via a K-type thermocouple, fixed in a small hole at the side of the crystal. A clean surface was confirmed by STM.

2.4. Rutile Titania Single-Crystal Surfaces

2.4.1. TiO_2(110) - (1 × 1)

Rutile TiO_2 is often used as a model substrate when it comes to oxides, since its conductivity is easily obtained by bulk reduction, its most stable facet the (110) surface was often studied experimentally and theoretically, and its surface shows many interesting features [30]. A model of the TiO_2(110) - (1 × 1) surface and the respective LEED pattern, observed for this surface, are shown in Figure 4. Characteristic for the (110) surface, is the alternating structure of bridging bonded oxygen rows and fivefold coordinated Ti^{4+} atom rows along the ⟨001⟩ direction. Relaxation such as found in previous studies [30] is not included in this scheme.

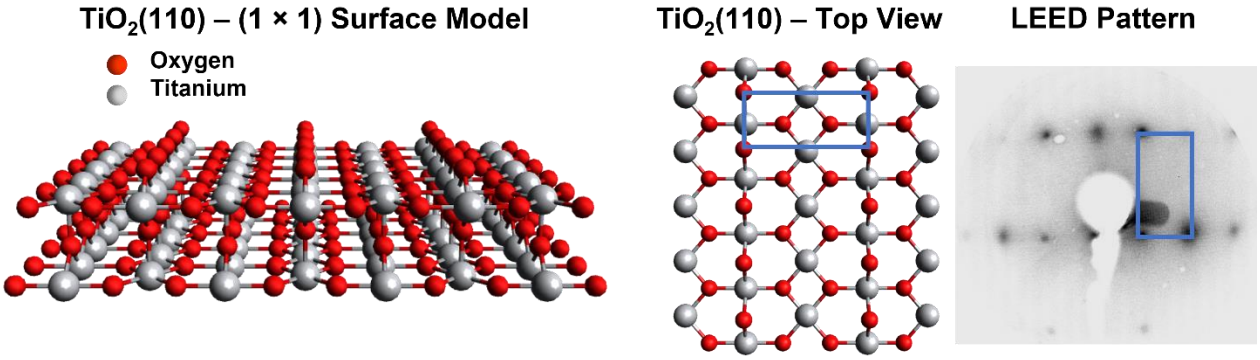

Figure 4 A ball-stick model of a rutile TiO_2(110) - (1 × 1) single crystal surface. Titanium atoms are depicted in grey while the oxygen atoms are shown as red balls. A top view of the TiO_2(110) - (1 × 1) surface is shown next to a picture of the LEED pattern observed for this surface. The LEED pattern was acquired with 110 eV.

The real surface is not as perfect as shown in Figure 4. A variety of defects affect the chemical and physical properties of TiO_2 and have a large impact on applications in photocatalysis and photoelectronics [30-33]. These defects are usually divided into four classes, point defects, line defects, interfacial defects, and bulk defects. Point defects, such as vacancy defects, interstitial defects, and substitutional defects, are often the matter of research due to their high relative abundance in the slightly reduced TiO_2 crystals [32].

Vacancy defects are positions in the crystal lattice, where in the case of a perfect crystal an atom would be expected, however an atom is missing. Noteworthy, for TiO_2(110) prepared by sputtering and annealing in ultrahigh-vacuum oxygen vacancies, as depicted Figure 5, are quite characteristic [30, 32]. It is well-known from literature that on the rutile TiO_2(110) surface oxygen vacancies are more stable on the surface than in its bulk as described in [34] and references therein, and that oxygen vacancy sites are among the most reactive sites on TiO_2(110) surfaces [35]. They were not only found interesting for ultrahigh-vacuum experiments but also

during catalytical reactions closer to ambient conditions [36]. Thus, it becomes obvious that the reduction degree and with this annealing temperature and annealing time are crucial for the surface structure and its reactivity. Higher annealing temperatures such as > 1000 - 1100 K result in different surface structures such as (1 × 2) or others [30, 35]. In the studies performed in the context of this thesis, only (1 × 1) surfaces were investigated for TiO_2. For a (1 × 1) surface, the amount of oxygen vacancy sites per surface unit cell is typically in the range up to roughly 0.07 - 0.14, often given in ML, where 1 ML is one oxygen vacancy per one surface unit cell [30, 35]. The size of a surface unit cell is given in Figure 4 as indicated with the blue rectangular.

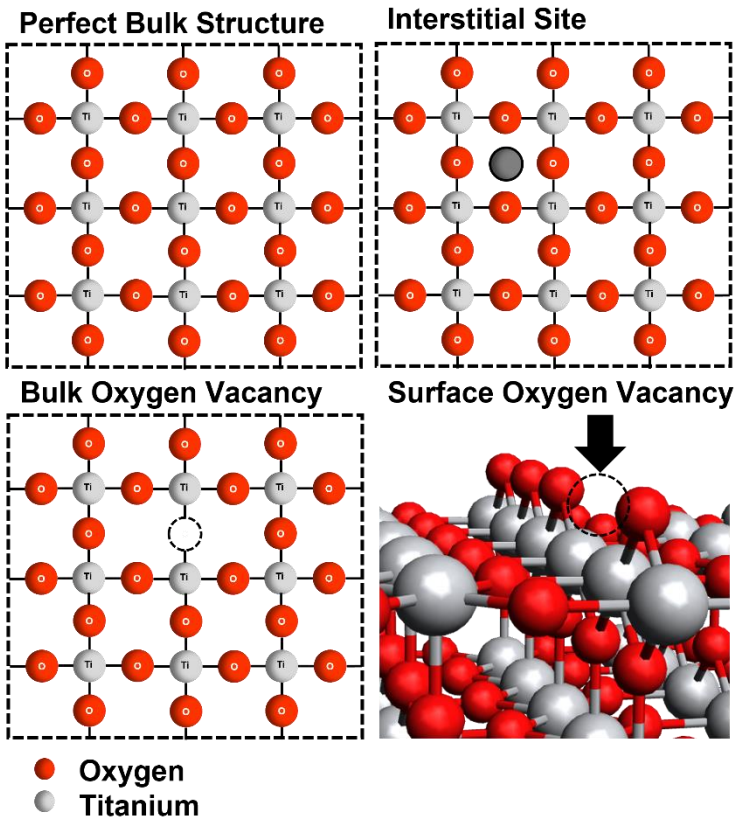

Figure 5 The perfect bulk structure of TiO_2 is shown and an interstitial site is depicted. Further oxygen vacancies are shown, a bulk oxygen vacancy and a surface bridging oxygen vacancy. This Figure is inspired by Figure 3.2 in [32].

A further type of defects commonly observed in rutile TiO_2 is Ti interstitials. In general, interstitials also belong to the group of point defects and, as depicted in Figure 5, the concept of this defect is that atoms occupy positions in a crystal lattice that would not be occupied in a perfect lattice. The type of atom occupying an interstitial site can either be an atom also comprised in the crystal or a foreign atom. Dependent on that, it is either called self-interstitial or impurity interstitial, respectively. Thus, the Ti interstitials in TiO_2, belong to the group of self-interstitials [36].

Ti interstitials are also formed during sputtering and annealing in ultrahigh vacuum [30]. They can be either in a 3+ or in a 4+ state. According to [35] and references therein, the Ti^{3+} is predominant in reduced TiO_2. It has been recognized in literature that Ti interstitial sites are also important for many surface reactions [30, 35, 36]; however, the role of Ti interstitials on surface processes has not been fully understood yet [37]. Further discussion in this direction is beyond the scope of this thesis and the interested reader is referred to the references that were just mentioned.

Hydroxyl groups are also often observed when it comes to TiO_2(110) surfaces. One way to create hydroxyl groups on TiO_2(110) is upon dissociative adsorption of water at defect sites [30]. Noteworthy, water is omnipresent in almost all TiO_2 applications under ambient conditions [38] and the water - TiO_2 interface is principally interesting for many applications, such as for instance water splitting, air or water purification and water-based solar cells. This promoted the frequent study of adsorption of water on TiO_2 and with this also the characterization of OH groups. Even though ultrahigh vacuum is applied to prepare surfaces, OH groups are often obtained by residual water adsorption at defect sites and subsequent water splitting reaction, since water is one of the major contributions in the residual gas of ultrahigh-vacuum chambers [30, 39-41]. Thus, the amount of OH groups on the surface is largely dependent on the water concentration in the residual gas, the defect concentration on the TiO_2 surface, and the time the clean surface is exposed to the residual gas.

The time until all oxygen vacancies are filled up with OH groups can roughly be estimated using Equation 1 from Chapter 2.1. The impingement rate for H_2O ($m = 2.99 \cdot 10^{-26}$ kg) at room temperature (293 K) at $1 \cdot 10^{-10}$ mbar or $1 \cdot 10^{-8}$ Pa is $3.62 \cdot 10^{14}$ s^{-1} m^{-2} and the number of free sites per area must be determined, in this case the number of oxygen vacancy sites per surface area. From literature it is known that the number of defects varies between 7 to 14 % per surface unit cell [30, 35]. The size of one surface unit cell of a rutile (110) crystal surface can be calculated by the crystal parameter, given as a = b = 4.587 Å, $\sqrt{(a^2 + b^2)}$ = 6.487 Å and c = 2.953 Å [30], and yield a unit cell size of $1.915 \cdot 10^{-19}$ m^2. This is equal to $5.2 \cdot 10^{18}$ unit cells per m². If 7 to 14 % include oxygen vacancies, the density of oxygen vacancies is 3.6 to $7.3 \cdot 10^{17}$ m^{-2}. Dividing the oxygen vacancies per surface area by the impingement rate gives the time until all oxygen vacancies are filled. Further assuming a sticking coefficient of 1, it takes roughly 17 min for 0.07 ML and 34 min for 0.14 ML of oxygen vacancies to be occupied at a partial pressure of water of $1 \cdot 10^{-10}$ mbar.

Oxygen vacancies, Ti interstitials and OH groups are probably the most important point defects that affect or are present at a reduced rutile TiO_2(110) surface, as prepared under ultrahigh-

vacuum conditions. Thus, in summary, the complexity of the TiO_2(110) - (1 × 1) surface is higher compared with a Cu(111) surface, since (1) protruding oxygen rows define the surface, (2) the reduced bulk affects the surface and (3) additional surface features such as oxygen vacancies and hydroxyl groups strongly influence the surface properties. This information needs to be kept in mind when studying the adsorption and reaction of molecules on TiO_2(110) - (1 × 1).

2.4.2. Improved TiO_2 Sample Mounting

TiO_2 sample mounting showed many unexpected challenges, in particular when it comes to accurate temperature reading and thermocouple mounting. For metal single crystals, typically, the thermocouples are often either spot-welded or fixed in a hole at the side of the crystal. For oxide single crystals spot-welding is not possible and manufacturing of a hole is very difficult. One typical way of mounting oxide single crystals is mounting them in a tantalum boat, see scheme Figure 6, and spot-weld the thermocouple to the tantalum boat instead of directly to the crystal, such as for the experiments in our lab in Erlangen. Noteworthy, in vacuum the thermal conductivity between the tantalum boat and the crystal is very bad and, as a consequence, the temperature of the boat can be very different compared to the temperature of the crystal.

What we needed was a firmly mounted thermocouple with good thermal contact to the crystal. Our solution was to glue the thermocouple directly to the side of the crystal [P4], using an aluminum-oxide-based high-temperature glue, called Ceramabond 569 (T-E-Klebetechnik). After glueing the thermocouple in air, the glue had to be hardened at 120°C for 2 h and after introduction into vacuum, a slow heating ramp was used to degas the glue and this resulted in very accurate temperature readings.

For the STM experiments on Cu(111) [P1], the crystal had a hat-shaped form and was pressed onto the sample holder as shown in Figure 6. The thermocouple was mounted as part of the sandwich structure, being pressed together. A very similar approach was used 2015 in China for TiO_2 [P2] and 2018 at Elettra-Sincrotrone Trieste [P3] but with a flat geometry instead of hat-shaped. This resulted in the tantalum mount pressing down on the crystal to be at a higher position than the crystal, and, therefore, tantalum was found on the crystal after sputtering. This was solved by using very narrow strips of tantalum to hold down the crystal. Similar to that is mounting the crystals in a tantalum envelope pressing from the top and thermocouples only touching from the backside, as for our mounting at the synchrotron measurements in [P3]. The measurements in [P3] showed a strong difference, as high as 300 K at 950 K and that forced us to do a linear correction with a resulting temperature of 650 K.

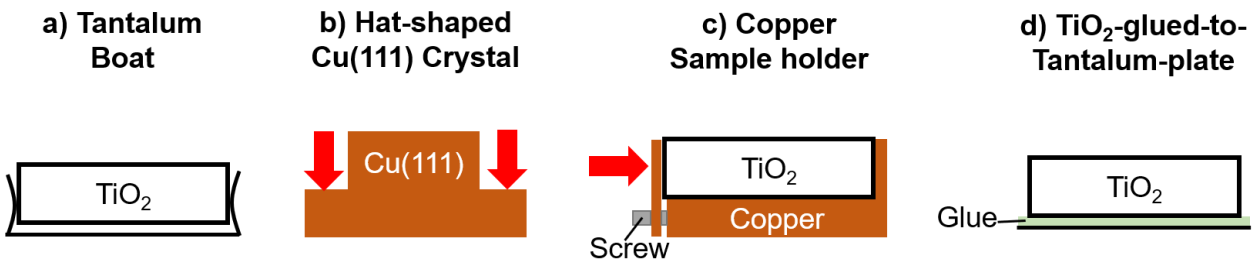

Figure 6 Different sample mountings. (a) In our best approach, the TiO_2 crystal is mounted in a tantalum boat with the sides acting as a spring, pressing against the crystal. The thermocouple for this approach was glued to the side of the crystal. (b) The Cu(111) hat-shaped crystal was pressed to the sample holder from the top, at the lower lying plateau of the crystal by a screwed plate, as indicated by the red arrows. (c) A copper sample holder was used, where a screw pressed the two sides of the holder against the TiO_2 crystal. The thermocouple was clamped between the crystal and the copper sample holder. (d) The TiO_2 was glued to a tantalum plate and the thermocouple was glued to the side of the crystal.

Before arriving at the solution with the glued thermocouples we tried several other options: One option was a copper sample holder, manufactured by our machine shop, see Figure 6. The copper sample holder consisted of two parts pressing against the sides of the crystal thereby providing a good thermal contact between the crystal and the copper. The thermocouple was pressed between the copper and the crystal. Noteworthy, annealing and temperature reading worked well the first time, but the expansion coefficient of copper and of titania differed and the crystal came loose.

Another option was gluing the TiO_2 crystal directly to a tantalum plate using the same Ceramabond 569 as mentioned above, see Figure 6. The glue worked well and bound the crystal strongly to the tantalum plate, but due to the different expansion coefficients of titania and tantalum the crystal broke in pieces after several annealing cycles.

2.4.3. TiO_2(110) - From Insulating to Conducting

As purchased, the crystal is mostly a perfect rutile TiO_2 crystal, a semiconductor with a band gap of 3 eV and thus absorption of visible light is only occurring to a very limited amount in the UV regime [42]. In contrast, the reduced TiO_2 crystal shows coloring, see Figure 7. The color is often referred to as a qualitive measure of the reduction degree of the crystal [35, 43]. According to literature, the color is due to bulk reduction and the resulting color centers [30]. Color centers are point defects, unoccupied sites in the crystal lattice, related with trapped electrons or holes [44]. Generally, the trend is, the higher the degree of reduction the more the color changes from light blue to dark blue [30].

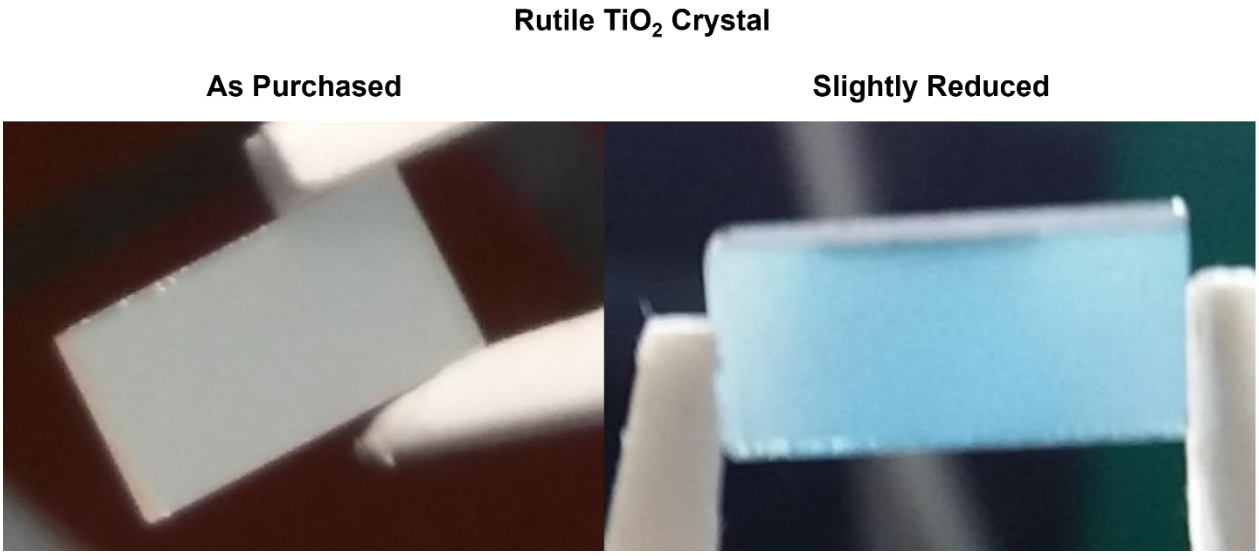

Figure 7 Picture of a TiO_2(110) crystal before and after the experiment. The picture on the right was acquired at the end of our beamtime at the synchrotron facility Elettra (Triest, Italy) in October 2019.

The correlation of the TiO_2 crystal color with the number of bulk defects, conductivity, and the surface structure was studied by Li et al. in 2000 [45]. They found that for darker rutile crystals the concentration of crystallographic shear planes, extended Ti^{3+} related bulk defects, is larger, while comparable to the brighter crystals, the amount of interstitial and substitutional defects is lower. Here substitutional refers to Ti^{3+} states derived from oxygen vacancies. Resonant excitation of electrons from both oxygen vacancies and Ti interstitials was expected to play a major role for the adsorption spectra [45]. The defects causing the coloring effect are also classified as intrinsic dopants and are well-known to modify the electronic structure by inducing bandgap electronic state at 0.8 – 1.0 eV below the Fermi level, with the Fermi level being close to the conduction band minimum [46]. Thus, the crystal is n-doped and becomes not only colored but also sufficiently conductive to investigate it with techniques such as X-ray photoelectron spectroscopy and scanning tunneling microscopy [47]. The source of the bandgap state is controversially discussed in literature and more recent results indicated that both, the bridging oxygen vacancies and the Ti interstitial sites contribute to this bandgap state, as concluded in [40] and references therein. Other studies [48, 49] showed that hydroxyl groups, have a major impact on the band gap state. Further studies described that small polarons generated by the excess electrons of the defects induce this band gap state [47, 50].

2.4.4. Preparation of TiO_2(110) - (1 × 1) Surfaces

All TiO_2(110) single crystals used in this thesis were purchased from CrysTec GmbH (Berlin, Germany) or Princeton Scientific (Easton, PA, USA). 5 × 10 mm^2 and 10 × 10 mm^2 crystals with a thickness of 0.5 or 1.0 mm were used, dependent on the available sample holder and setups. At Elettra-Sincrotrone in Trieste, 5 × 10 mm^2 crystals (CrysTec GmbH) with a thickness of 1.0 mm were used while for the other setups 10 × 10 mm^2 crystals were used with a thickness of 0.5 mm. For the work of 2HTPP on TiO_2(110) crystals, the crystals were purchased from Princeton Scientific, while for the other experiments, the crystals were obtained from CrysTec GmbH.

The TiO_2(110) crystal surfaces related to this thesis were single-side-polished and cleaned upon Ar^+ sputtering and annealing under ultrahigh-vacuum conditions. The most crucial point to obtain the reduced crystals and the desired (1 × 1) surfaces is the annealing temperature and with this the temperature acquisition. For information on the surface structure and the surface unit cell, see Chapter 2.4.1 and for more details on improvements in sample mounting and temperature acquisition, see Chapter 2.4.2. The sample typically also changes with the number of annealing cycles and become further reduced.

The crystals used for the benzohydroxamic acid experiments at the synchrotron facility Elettra as describe in paper [P4] were pre-reduced by annealing in one bar hydrogen until color of the crystal turned blue. Prereduction of the crystals was done to save precious time at the synchrotron facility, that would otherwise have been necessary for the reduction of the crystal by annealing in ultrahigh vacuum.

For new samples, independent of the mounting approach, the annealing temperature was increased stepwise carefully for the first annealing steps of a new crystal until the sample was conductive enough to perform X-ray photoelectron spectroscopy measurements without charging and the (1 × 1) LEED pattern was observed. Noteworthy, upon annealing it is well-known that the color changes from white/transparent to slightly yellow, green, light blue and eventually dark blue [30].

Notably, the crystals used for the experiments in most cases ended up with a light-blue color as shown in Figure 7. The only exception was the preparation of one of the TiO_2(110) crystals for the benzohydroxamic acids experiments as described in the respective paper. Interestingly, the results obtained from the dark blue crystal showed hardly any difference in comparison to the light blue crystal.

2.5. Information on the Molecules

In the context of this thesis, two groups of molecules were used: (1) tetraphenylporphyrins and (2) phenyl rings with functional groups, namely phenylphosphonic acid and benzohydroxamic acid. In the introduction, the motivation for the investigation of porphyrins was generally described, and the choice of these linker groups was specified in Chapter 3.3. In addition, the general structure of porphyrins and possibilities of functionalization were also shown the introduction.

All molecules were deposited on the clean crystal surfaces under ultrahigh-vacuum conditions, using a homebuilt evaporator equipped with a shutter. Different temperatures were used for evaporation as shown in Table *2*. In Table 3, information about the purchase of the molecules used in this thesis and the respective purity of the powders is given.

Table 2 Evaporation temperatures of the different molecules used in the context of this thesis.

Molecule Name	Evaporation Temperature
Meso-Tetraphenylporphyrin (2HTPP)	300°C
Meso-Tetraphenylporphyrin-Ti(IV)O (TiOTPP)	350°C
Mono(para-cyanophenyl)-triphenylporphyrin (2HMCNTPP)	300°C
Cis-di(para-cyanophenyl)-diphenylporphyrin (2HcisDNMDPP)	370°C
Tetrakis(para-cyanophenyl)-porphyrin (2HTCNPP)	450°C
Phenylphosphonic acid (PPA)	130-140°C
Benzohydroxamic Acid (BHA)	35-45°C

Table 3 Information about the purchase and the purity of the molecules used in the context of this thesis. For information about abbreviation of the molecule names, see Table 2.

Molecule Name	Information on Purchase	Cleanliness
2HTPP	Porphyrin Systems Hombrecher e. K. (Halstenbek, Germany)	> 97%
TiOTPP	Porphyrin Systems Hombrecher e. K. (Halstenbek, Germany)	> 95 %
2HMCNTPP	Synthesized by Jux group*	> 95 %
2HcisDNMDPP	Synthesized by Jux group*	> 95 %
2HTCNPP	Synthesized by Jux group*	> 95 %
PPA	Sigma-Aldrich (Saint Louis, MO, USA)	98 %
BHA	Sigma-Aldrich (Saint Louis, MO, USA)	99 %

* Synthesized by the group of Apl. Prof. Norbert Jux at the Chair of Organic Chemistry II at the University of Erlangen (FAU)

Noteworthy, the evaporation temperatures of phenylphosphonic acid and benzohydroxamic acid, as shown in Table 2, are close to or below the bakeout temperatures of ultrahigh-vacuum setups (130°C). Thus, the water cooling of the evaporators needs to be switched on during the bakeout process, to avoid emptying the evaporator. Usually for porphyrins, the evaporator is (1) annealed during the bakeout and (2) annealed after the bakeout to 180°C for more than 8 h with a closed shutter to pump off water and other contamination being present in traces in the powder. This further purifies the given powder. This is not possible for phenylphosphonic acid and benzohydroxamic acid. So, these were degassed for at least 15 min at the evaporation temperature before the first actual deposition. For benzohydroxamic acid, in addition, the background pressure of the preparation chamber was quite high, most likely due to the high vapor pressure of benzohydroxamic acid at room temperature. To decrease the background pressure during the deposition and to achieve submonolayer coverages cryopumps were used

2.6. Methods and Fundamental Principles

2.6.1. X-ray Photoelectron Spectroscopy

In the early 1960s, when stainless-steel ultrahigh-vacuum systems became available and pressures of 10^{-9} mbar could be maintained on the daily routine, clean surfaces could be prepared and kept clean for up to one hour. More information on ultrahigh vacuum is given in the Chapter 2.1. Based on this ultrahigh-vacuum environment, several techniques were developed in the past 60 years. Among them, XPS developed one of the most widespread applications.

Basic Principles

The photoelectric effect, especially the outer photoelectrical effect, the main principle XPS is based on, was first discover by Hertz in 1887. Subsequently it was understood in more detail and extended to photon energies in the X-ray regime, by Einstein and Innes. Briggs and Grant summarized the most important milestones in reference [51], which is strongly recommended to the interested reader.

Acquiring XP spectra requires, besides a sample, a radiation source, a monochromator (optional) and an electron-energy analyzer, all inside an ultrahigh-vacuum chamber. By irradiation of the sample with light of a chosen wavelength, in the laboratory usually Al Kα (1486.7 eV) or Mg Kα (1253.6 eV), electrons are ejected from core levels into the vacuum. These emitted photoelectrons are detected by the analyzer as a function of kinetic energy. The kinetic energies of the emitted photoelectrons are detected by the analyzer, thereby giving information about the binding energies of the core levels the electrons originated:

$$E_B = h\nu - E_K - \phi \qquad (2)$$

where $h\nu$ is the photon energy, E_K the kinetic energy of the detected electrons and the ϕ is the work function of the analyzer. The acquired intensity as a function of binding energy gives qualitative and quantitative information on the sample.

Outstanding Properties of X-ray Photoelectron Spectroscopy

The main reasons why XPS became an important technique for surface analysis:

(a) XPS is **surface sensitive**: Even though X-rays penetrate several micrometers into the specimen, the low inelastic mean free path of the emitted photoelectrons make XPS one of

the most surface sensitive techniques. An electron traveling through solid matter undergoes several scattering events and these scattering events are divided into two groups, namely elastic and inelastic scattering [51]. The attenuation rate of photoelectron intensities by inelastic scattering can be described by the electron inelastic mean free path (IMFP). The IMFP is a quantity defined as the “average distance that an electron with a given energy travels between successive inelastic collisions” [52], and from this quantity the information depth can be estimated, that is in the regime of only a few nanometer [51]. A universal correlation was found 1979 by Seah and Dench, relating the energy of electrons to the electron inelastic mean free path. Visualizing this correlation leads to the “Universal Curve” as shown in Figure 8, with the respective experimental data points [53]. The curve possesses a minimum mean free path in the range of 30 to 100 eV. In XPS the energies of detected photoelectrons are typically in the range of 100 to roughly 1500 eV, yielding mean free paths of 0.5-3 nm and thus very high surface sensitivities.

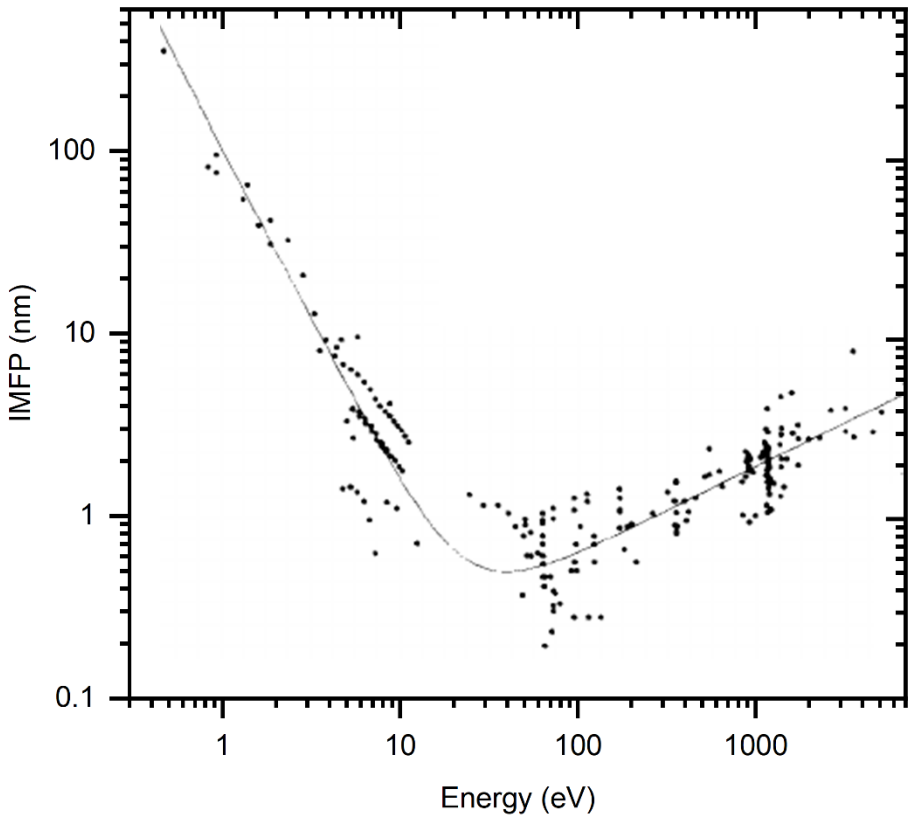

Figure 8 The “Universal Curve” visualizes the relationship between the electron inelastic mean free path and the energy of the electrons. This Figure is adapted with permission from the publication by Seah and Dench [53].

Noteworthy, the “Universal Curve” should only be taken as a guideline [51, 53]. The exponential attenuation of the detected substrate signal as a function of layer thickness for layer-by-layer growth, which was found in experimental studies in the early times of XPS and

Auger-electron spectroscopy, is not entirely valid. Elastic scattering also should be considered. Thus, the term effective attenuation length was introduced to describe the non-exponential behavior of the attenuation of XPS intensities due to elastic electron scattering [54]. However, for film thicknesses of up to four times of the IMFP, the effective attenuation length and the IMFP were found in good agreement [54], if the emission angle for the electrons is chosen far away from grazing emission, such as 60° or lower with respect to the surface normal [51].

(b) XPS is **element specific**. The binding energy of core levels are characteristic for each element, and thus XPS gives information on the elements present in the near surface region. Binding energies and sensitivity factors for the elements can be found for example in the database of the National Institute of Standards and Technology (NIST) and in the XPS Handbooks by Moulder, Stickle, Sobol and Bomben [51, 55]. The overview spectra of phenylphosphonic acid deposited on TiO_2 - (1 × 1) depicted in Figure 9 shows all the elements of the molecule and substrate and illustrates well the element-specific character of XPS.

(c) XPS **is sensitive to the chemical state of the element**. In Figure 10, an O 1s XP spectrum of phenylphosphonic acid deposited on TiO_2 - (1 × 1) is shown as an example. For this spectrum, the different chemical environments of the oxygen atoms result in four peaks in the O 1s spectrum. On the left and on the right of the O 1s spectrum the different possible binding modes of phenylphosphonic acid on the surface are shown to illustrate the different chemical environment of the oxygen atoms.

XPS is furthermore quantitative and can through comparison with known reference samples be used to identify not just the elements present in the near-surface region, but also the amount of each element present. Scanning tunneling micrographs are often used as references of known coverage [48, 52]. More information of coverage calculations from XPS will be given in the next subchapter.

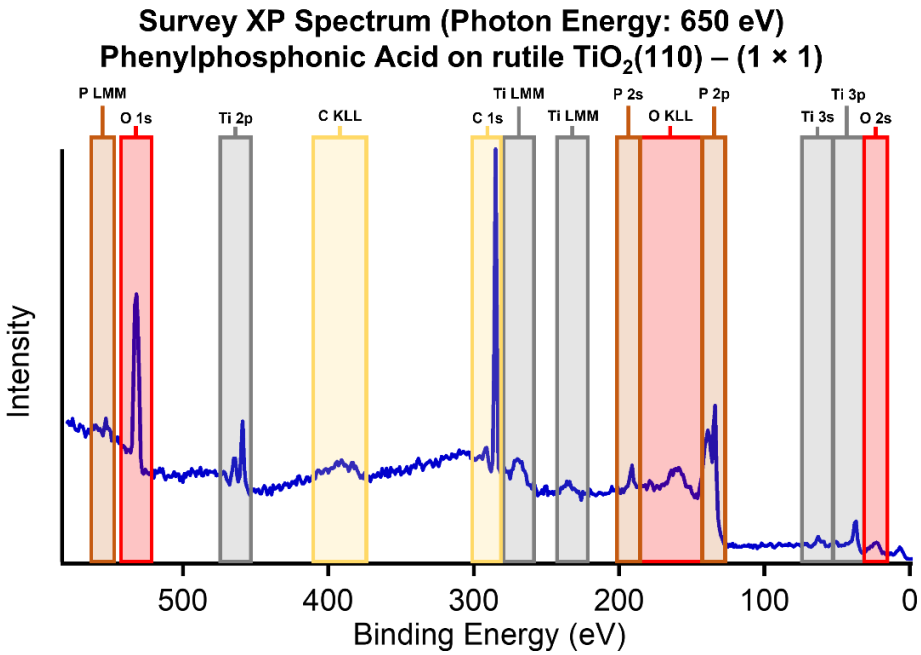

Figure 9 Survey XP spectrum of phenylphosphonic acid multilayer on rutile TiO_2(110) - (1 × 1) acquired with a photon energy of 650 eV. The characteristic peaks for the elements present are color-coded: brown for phosphorus, red for oxygen, grey for titania and yellow for carbon.

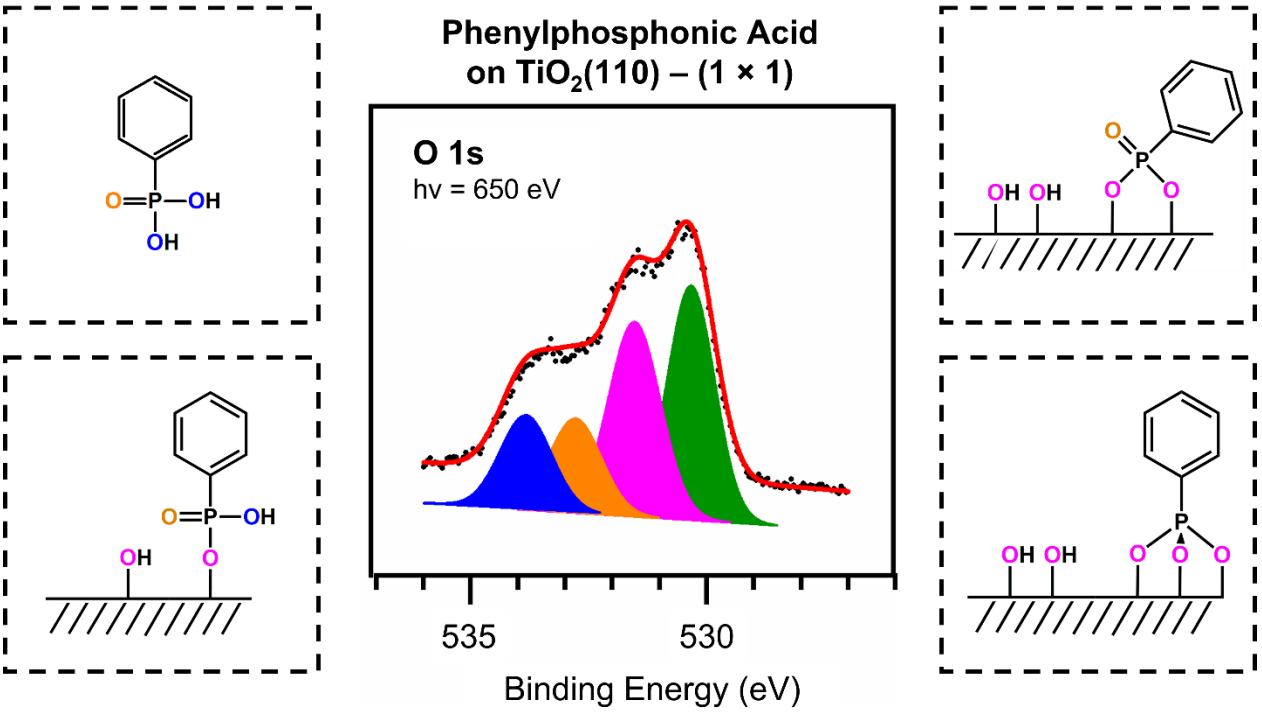

Figure 10 O 1s XP spectrum of phenylphosphonic acid on rutile TiO_2(110) – (1 × 1) acquired with a photon energy of 650 eV. Four oxygen species with different chemical environment can be identified: The green peak is assigned to the substrate oxygen atoms in TiO_2, while the pink peak is assigned to Ti-OH/P-O-Ti, the orange peak to Ti=O and the blue peak to P-OH.

Further reasons for the success of XPS summarized by Watts and Wolstenholm are the investigation of thin films on surfaces, especially its thickness, the uniformity of the thickness and the uniformity of the chemical composition. For these reasons among others, XPS became one of the most useful techniques for chemical surface analysis [51, 56].

The thesis in hand is not able to cover all the relevant and interesting aspects of XPS, and the interested reader is therefore referred to books by Briggs and Grant [51] or Watts and Wolstenholm [56].

Coverage Calculations

As already mentioned not only qualitative but also quantitative information can be obtained from XPS. Similar to the Lambert Beers' law, the number of photoelectrons that escape from a given depth in a sample and reach the analyzer without losing energy can be estimated to decrease exponentially with the distance traveled in the solid [57]. In the following, 2D growth is estimated upon deposition. Further, we assume a homogeneous adsorbate layer with a thickness x on a flat substrate, see Figure 11.

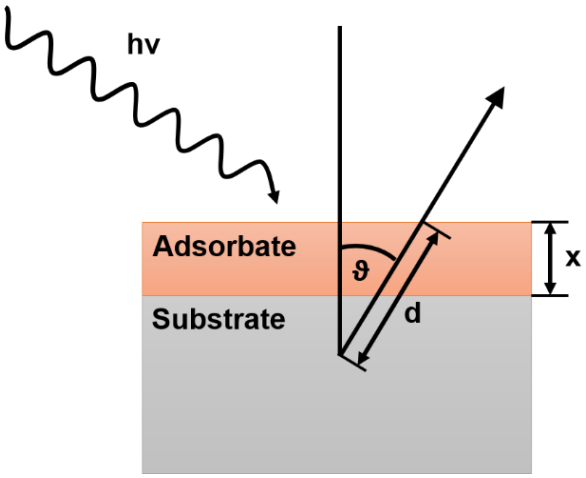

Figure 11 Scheme of a homogeneous adsorbate layer with a thickness x grown on a substrate. For further description see text.

The photoelectrons emitted from the substrate are now attenuated because of the distance they have to travel through the adsorbate layer [58-60] and the observed intensity I^S therefore becomes:

$$I^S = I^S_\infty \cdot e^{\frac{-x}{\cos\vartheta \cdot \lambda_s}} \tag{3}$$

where I_{∞}^{S} is the unattenuated signal of the clean substrate, ϑ is the emission angle with respect to the surface normal, x is the thickness of the layer and λ_S is the inelastic mean free path of the photoelectrons. The distance an electron travels through the sample is often given with d, and d equals $x/\cos\vartheta$.

Similarly, the observed intensity of the adsorbate layer I^{ad} can be described as the intensity from a pure, infinitely-thick adsorbate film I_{∞}^{ad} minus the intensity missing because of the limited thickness of the film:

$$I^{ad} = I_{\infty}^{ad} \cdot (1 - e^{\frac{-x}{\cos\vartheta \cdot \lambda_{ad}}}) \tag{4}$$

In this thesis, the intensity of the infinite thick molecule film I_{∞}^{ad} is estimated by measurements of very thick organic film as obtained from multilayer deposition.

Both of the above equations can be used to calculate coverages. Especially in the beginning of this thesis all of three options were used and overall similar results were obtained. The substrate signal is usually better for larger coverages, while the adsorbate signal is better for smaller coverages. However, a better option is to use the ratio of the adsorbate and substrate intensities:

$$\frac{I^{ad}}{I^{s}} = \frac{I_{\infty}^{ad} \cdot (1 - e^{-\frac{x}{\cos\vartheta \cdot \lambda_{ad}}})}{I_{\infty}^{S} \cdot e^{-\frac{x}{\cos\vartheta \cdot \lambda_S}}} \tag{5}$$

This works for a wider coverage range and is less sensitive to changes in intensity caused by positioning or photon flux. The electron inelastic mean free path is dependent on the material the detected electrons travel through and on the kinetic energy of these electrons, see the Universal Curve in Figure 8 [61]. For many materials, the inelastic mean free path can also be found in different databases based on calculated or experimentally determined values [60, 62, 63]. In the example above in Equations 3-5 the mean free paths always refer to photoelectrons travelling through the adsorbate layer. If, additionally, the kinetic energies of the photoelectrons emitted by the substrate and adsorbate are identical or very similar, their mean free paths become identical $\lambda = \lambda_S = \lambda_{ad}$ and Equation 5 can be rewritten as:

$$\frac{I^{ad}}{I^{s}} = \frac{I_{\infty}^{ad} \cdot \left(1 - e^{-\frac{x}{\cos\vartheta \cdot \lambda_{ad}}}\right)}{I_{\infty}^{S} \cdot e^{-\frac{x}{\cos\vartheta \cdot \lambda_{S}}}} \tag{6}$$

For synchrotron measurements, the photon energies can be chosen so that the kinetic energies are the same or very similar, and thus equation (6) becomes valid. Using a laboratory X-ray source, such as an Al Kα source, we are restricted to one photon energy, 1486.7 eV for Al Kα. To show, if equation (6) is still valid, a comparison of two typically used kinetic-energy regions is done. This could for example be Ti 2p for the substrate and C 1s for the adsorbate signal. The respective kinetic energies of the photoelectrons, as generated upon photoionization applying an Al Kα source, are 1028 eV and 1202 eV. Based on [53] the Universal Curve, see Figure 8, we can estimate the inelastic mean free path for C 1s at a kinetic energy of 1202 eV to be roughly 8 % higher than the inelastic mean free path for Ti 2p at a kinetic energy of 1028 eV. This deviation is sufficiently small that equation (6) can also be used for lab-source XPS for coverage calculations involving C 1s and Ti 2p.

Generally, the equation (6) can be solved for λ:

$$\lambda = \frac{x}{\ln\left(\left(\frac{I^{ad}}{I^{S}} \cdot \frac{I_{\infty}^{S}}{I_{\infty}^{ad}}\right) + 1\right) \cdot \cos\vartheta} \tag{7}$$

Since we assume 2D growth, the number of layers can be given in multiples or fractions of layers. One layer of organic molecules on the surface, also referred to as monolayer or 1 ML, is the coverage we most often use as a known coverage reference. Therefore, the thickness of molecules x is 1 ML, while I^{s} and I^{ad} are the substrate and adsorbate signals from a sample with one monolayer of molecules on the surface, which we will call I_{mono}^{S} and I_{mono}^{ad}. Equation 7 thus can be written as:

$$\lambda[in\ ML] = \frac{1\ ML}{\ln\left(\left(\frac{I_{mono}^{ad}}{I_{mono}^{S}} \cdot \frac{I_{\infty}^{S}}{I_{\infty}^{ad}}\right) + 1\right) \cdot \cos\vartheta} \tag{8}$$

When annealing a multilayer of porphyrins to temperatures above 470 - 550 K [15, 64-66], the multilayer desorbs and a monolayer remains on the surface, which can use used as coverage reference. For absolute coverages STM measurements are needed. STM was used in the past to

determine the number of porphyrin molecules in a monolayer to be 0.51 molecules/nm^2 on Ag(111) [15, 65, 67] and 0.46 molecules/nm^2 on Cu(111) [68].

For benzohydroxamic acid, evaporation onto TiO_2(110) while holding the sample at room temperature always resulted in the same saturation coverage, and we used this as our monolayer reference. For phenylphosphonic acid annealing multilayer samples to temperatures above 380 K lead to a constant coverage that we used as monolayer reference.

With the inelastic mean free path determined in units of monolayers, the next step is to calculate the coverage from an unknown sample using Equation 7 and solve it for x:

$$x = \ln\left(\left(\frac{I^{ad}}{I^{S}} \cdot \frac{I^{S}_{\infty}}{I^{ad}_{\infty}}\right) + 1\right) \cdot \cos\vartheta \cdot \lambda \tag{9}$$

To sum up, the term monolayer can be defined as the number of molecules per surface substrate atoms, molecules per surface unit cell or molecules per nm^2, but this requires references where the coverage is known, typically derived from STM. When only performing XPS, this is not possible, and a monolayer is often defined as the coverage remaining when annealing a multilayer or as the saturation coverage at a certain temperature. From this reference coverage, λ can be calculated using Equation 8, and, from this λ, the coverage of an unknown sample can be calculated using Equation 9.

2.6.2. Scanning Tunneling Microcopy

Scanning tunneling microscopy (STM) has become a very powerful surface analysis technique, starting with the imaging device by Young et al. [69, 70] and the first practical implementation of STM by Binnig, Rohrer and coworkers at IBM in 1981 [71, 72].

The main reason for the success of STM is that by using this technique and mapping surfaces with atomic resolution a variety of information can be obtained. To name just a few examples, the size of the unit cell of clean and adsorbate covered surface structures [73, 74], location of defects such as oxygen vacancies and surface OH groups [75, 76] and topography of nanosized structure [77] can be derived by STM measurements. Further very interesting applications of STM are the mapping of molecular orbitals [78, 79] and the mechanism of picking up [80] and rearranging molecules [81], in mostly any desired way, just to name a few examples.

Comparing STM to XPS, STM gives a local resolution of the surface, while XPS averages over a large area. STM cannot directly give chemical information, while XPS is specialized on that. Thus, STM and XPS is a very good match for complementary methods, especially in combination with theoretical calculations.

STM is mainly based on one quantum-mechanical phenomena, the tunneling effect [82]. Bringing an extremely-sharp conductive tip close to a surface while applying a bias voltage between tip and sample results in tunneling of electrons through the vacuum gap, see Figure 12. Tunneling occurs, even though in a classical model the kinetic energy of the electron is not sufficient to overcome the barrier, and thus a so-called tunneling current can be detected [72, 82, 83]. The tip is often composed of pure metal such as tungsten, iridium or a platin-iridium alloy, and in the ideal case contains one atom at its sharpest point [84]. The shape of the tip becomes especially critical for high-resolution images [84-86]. The sample is must be conductive or semi-conductive and only thin insulating surface layers can be investigated [84, 87]. The measured tunneling current is related to several parameters, such as the tip position relative to the sample position, the voltage applied and the local density of states [85, 86, 88, 89]. Dependent on the applied bias voltage one can either tunnel electrons from the sample to the tip or vice versa and thus gain information on the occupied or the unoccupied states, as shown in Figure 12 right [86]. The extracted current map as a function of x and y position of the surface is called a scanning tunneling micrograph. The image includes information on both the physical topography landscape and the local electronic structure [90-92]. Thus, one needs to be careful interpreting the measured micrographs solely by topography or solely by electronic structure.

To move the tip with precision in the angstrom regime the piezoelectric effect is used. Upon applying a voltage, a piezoelectric crystal extends or contracts in the angstrom to µm range. Three mutually perpendicular crystals are used, the x, y, and z piezo crystals, in combination with a feedback loop, to achieve the small movements. Before using this so-called piezo drive, a coarse positioner is used for the coarse approach of the tip [72, 86, 93].

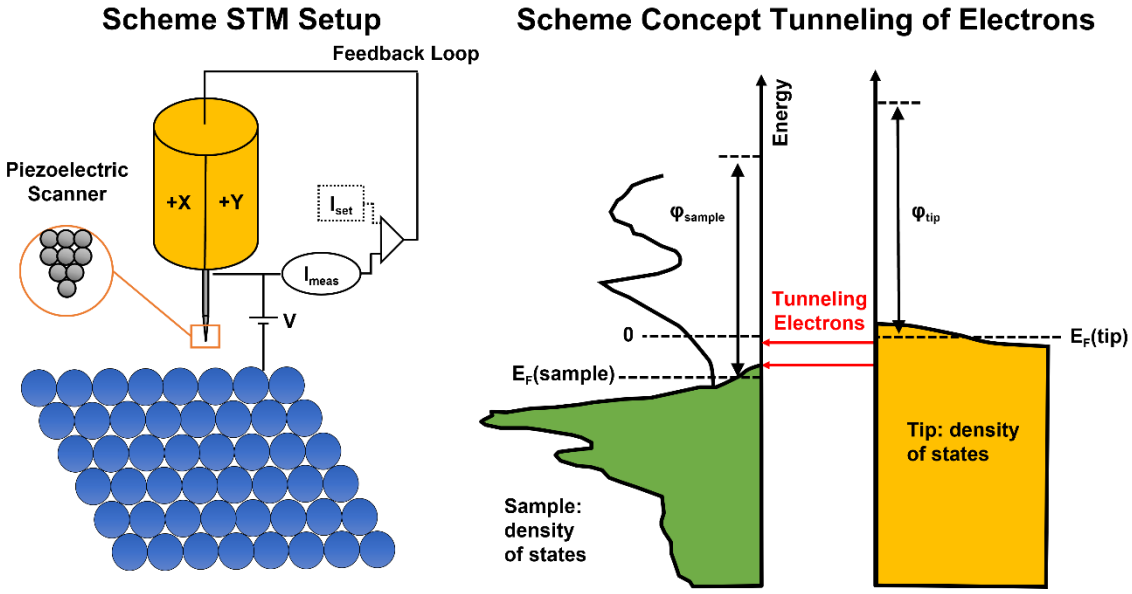

Figure 12 Scheme of an STM setup containing a sample, a piezoelectric scanner with an atomically sharp tip and a feedback loop. Scheme, that describes the tunneling of electrons through a tunneling barrier from the occupied states of the tip to the unoccupied states of a positively-biased sample. Reversing the polarity of the sample will reverse the tunneling direction.

Further information on the tunneling effect can be found in [72, 83, 84, 89, 94]. Also, detailed description of STM principles and typical STM setups is given in literature [86].

Noteworthy, the STM images acquired in the context of this thesis, were acquired in a constant-current mode and the bias voltage given, refers to the sample. The STM data was processed using WSXM [95], by linear-background subtraction and moderate low-pass filtering.

2.6.3. Near-Edge X-Ray-Adsorption Fine-Structure spectroscopy

NEXAFS-Background

Near-edge X-ray-adsorption fine-structure (NEXAFS) spectroscopy, also called X-ray-absorption near-edge structure spectroscopy (XANES), is an X-ray absorption spectroscopy (XAS). XAS is an element-specific technique and investigates the absorption of X-rays close to an absorption edge of choice by varying the photon energy. Thus, XAS can be divided into two categories according to the photon energies applied: NEXAFS, which ranges from the absorption onset to a few tens of eV, and extended X-ray absorption fine-structure spectroscopy (EXAFS), which ranges up to 1000 eV above the adsorption edge. While NEXAFS spectroscopy probes the unoccupied states accessible to the target atom, EXAFS probes the local structural environment of the investigated atom [96].

NEXAFS spectroscopy is a synchrotron-based technique involving transitions of core level electrons into states near the vacuum level. The position of the absorption edge is characteristic for different chemical elements, and NEXAFS spectroscopy is thus element sensitive. The non-ionizing transitions to electronic states just below the vacuum level include transitions to the lowest unoccupied molecular orbitals (π* resonances), Rydberg states and quasi bound continuum states (σ* resonances). Photon energies close to the ionization potential of the element are applied and results in an excited electron and a core hole, as depicted in Figure 13. Subsequent relaxation of this electron-hole pair occurs via emission of a fluorescent photon or an Auger electron, as also shown in Figure 13.

The absorbance can be measured directly as the transmission of X-rays through a thin sample or indirectly as the decay of the excited state through fluorescence yield or electron yield. Electron yield can again be acquired differently as either Auger yield (AEY), partial electron yield (PEY) or total electron yield (TEY). Auger yield (AEY) and partial electron yield (PEY) are both very surface sensitive, total electron yield (TEY), as compared, is less surface sensitive and fluorescence yield is more bulk sensitive [96-98].

Noteworthy, when it comes to the resonant excitation of electrons, in literature, two different Auger decays can be found: the spectator and the participator Auger decay. For the participator Auger decay, the core electron that was originally excited in the photoexcitation process, participates in the Auger process, as shown in Figure 14. In contrary, for spectator Auger decay, the excited core

electron is not participating. For both, participator and spectator Auger decay, in total only a single ionization occurs.

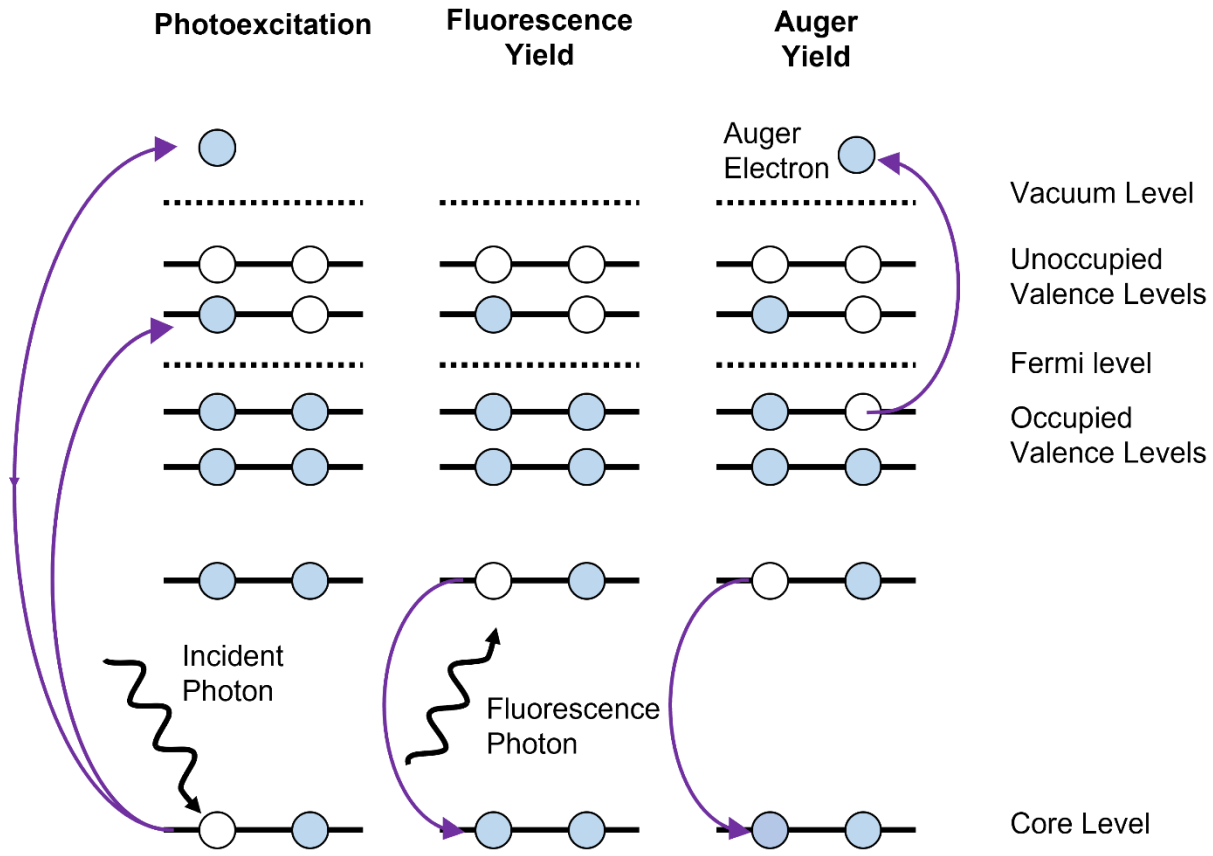

Figure 13 Absorption of an incident photon with subsequent excitation of a core electron into unoccupied levels or the continuum level is shown. Two possible follow-up processes are depicted, both resulting in filling up of the empty core level by an electron from a higher occupied level. This process is then either accompanied by release of a fluorescence photon or emission of an Auger electron.

NEXAFS spectroscopy specifically addresses the local electronic structure and bonding environment of the investigated target atom and has been used to study functional groups in polymers [99-101] as well as small molecules used in solar cells [102]. Applying well-known reference spectra, unknown species can be identified and even quantification of surface species is possible by comparison with normalized reference spectra [103]. NEXAFS spectroscopy can also be acquired as a function of the polar and azimuthal angles of the incoming polarized light, and by making certain symmetry assumptions even the orientation can be determined [98, 104].

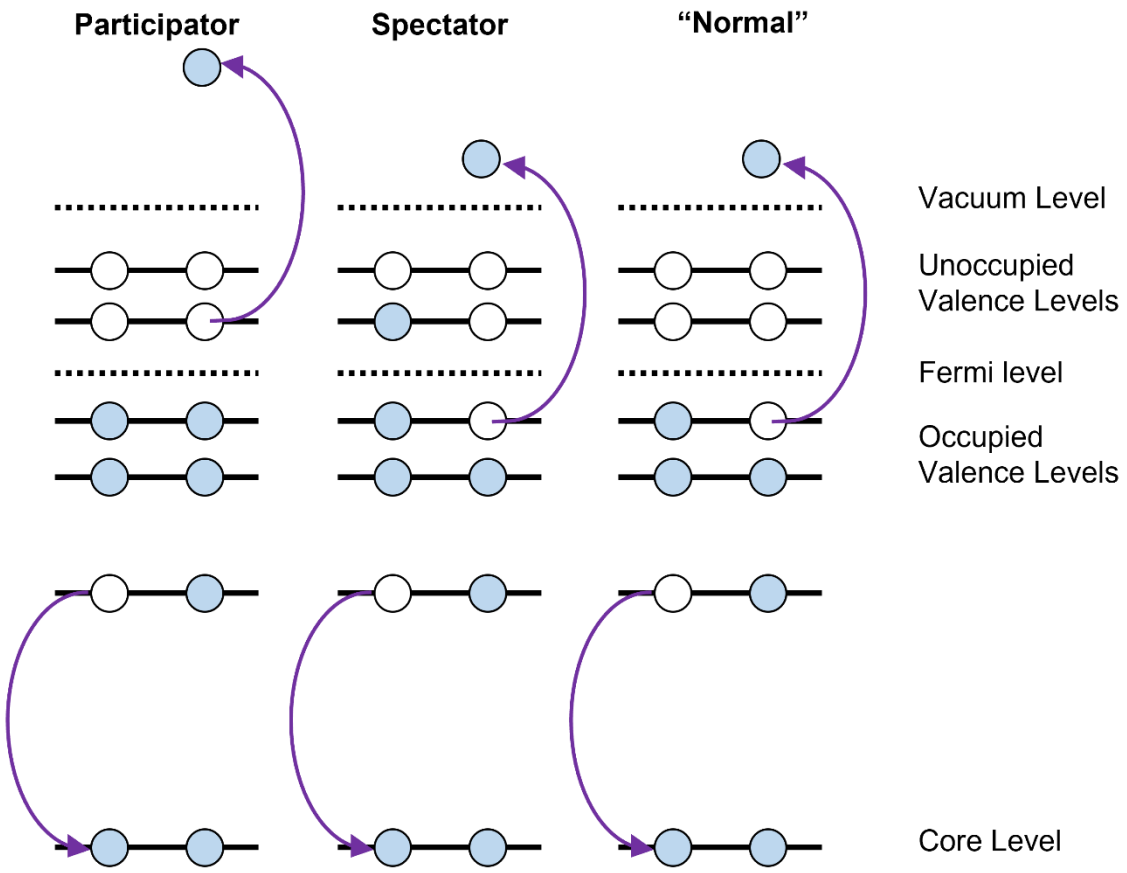

Figure 14 Three different types of Auger decay are shown. For all three, a nonradiative decay occurs: The previously generated core hole is filled by an electron of an occupied level with a smaller binding energy than the core level and an Auger electron is created. The participator Auger decay is shown, where the excited core electron participates the Auger process. Further, the spectator Auger decay is depicted where the excited core electron does not participate the Auger process. For comparison, the “normal” Auger process is shown.

Another interesting field of application for the highly surface-sensitive Auger detection mode [97] is the charge transporting region in OFETs, which consists of the first 1-3 nm of the surface. NEXAFS spectroscopy is also often applied when it comes to resolution of chemically similar states such as sp^2- and sp^3- hybridization states of carbon, that are difficult to resolve in XPS [100].

The main challenges for Auger-yield NEXAFS spectroscopy are removal of XPS features and determination of the photon flux [105]. Correction of intensity via the photon flux is often performed by simply dividing by the mesh current of a gold mesh. However, carbon and oxygen contamination if present on the gold mesh complicate the correction [101, 105, 106]. To overcome this issue and be more accurate, we measured the peak intensity of the Ti 3p peak of a clean surface as a function of excitation energy. The NEXAFS spectra were then corrected by the intensity of this photoemission line.

Description of the Applied Clean-Up Procedure

To remove photoemission features from Auger-yield NEXAFS, the cleanup procedure reported by Lytken et al [107] was applied. This procedure was used to remove photoemission features from two-dimensional Auger-yield-NEXAFS (2D) spectral images. These kinds of images can be described as the sum of an XPS image and a NEXAFS image, see Figure 15 top. The XPS image can be described by a single, one-dimensional (1D) X-ray photoelectron spectrum, see Figure 15 right, while the NEXAFS image can be described as the matrix product of a 1D NEXAFS spectrum in horizontal direction and a 1D Auger spectrum in vertical direction, see Figure 15 left.

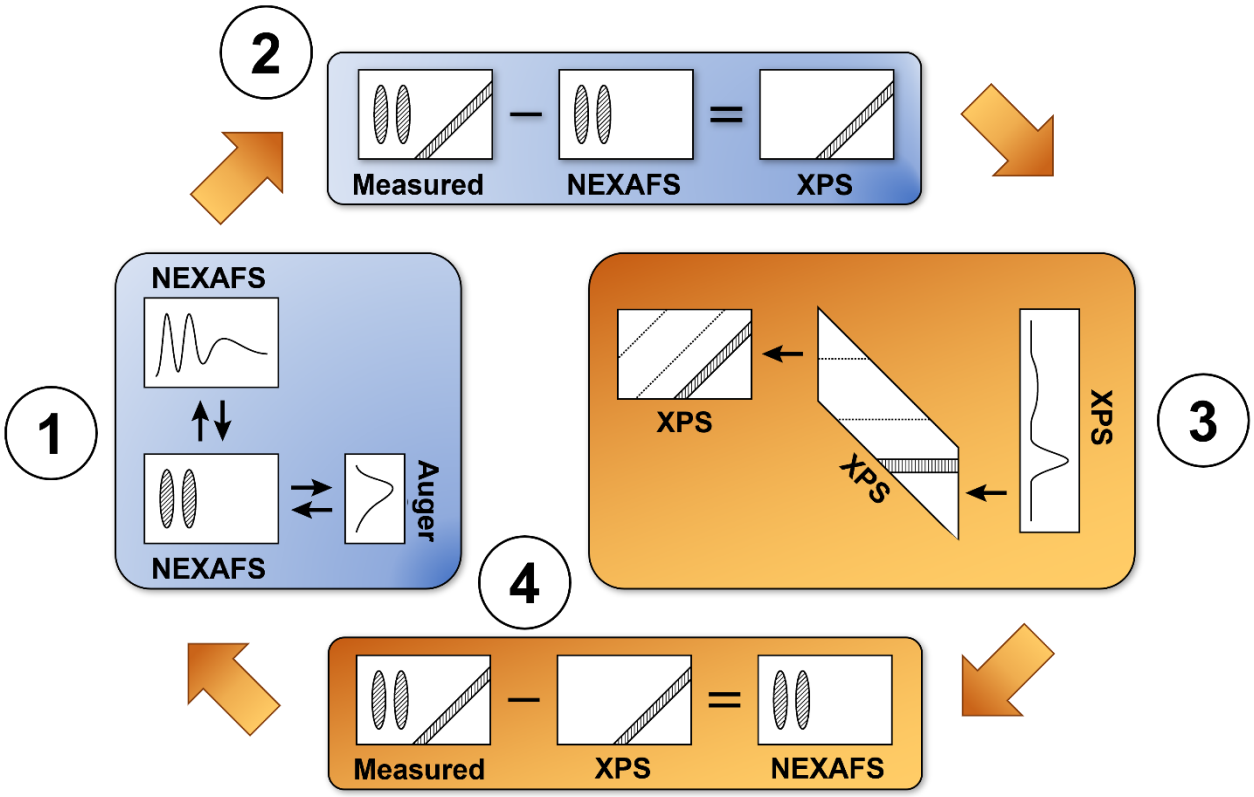

Figure 15 The four-step iterative cycle applied to the 2D spectral images to remove the photoemission feature. Dependent on the intensity of the photoemission features compared to the NEXAFS features, the cycle is either started with step 1 or 3. The four steps are described in detail in the text. The image was adapted with permission from [81].

Before starting the first cycle the measured image is normalized to the photon flux [107] and the offset before the first resonance is subtracted. Four-steps are then iteratively used, as shown in Figure 15, to extract the one-dimensional NEXAFS, Auger and photoemission spectra from the measured image. In step (1), see Figure 15, the measured image is averaged vertically, along the kinetic energy axis, to get the one-dimensional NEXAFS spectrum, and then horizontally, along the photon energy axis, to extract the Auger spectrum. These two spectra are now multiplied to

create a new NEXAFS image with smeared out XPS features. In step (2), the generated NEXAFS image can be subtracted from the original measured image to obtain an image with mostly XPS features remaining. (3) The kinetic-energy scale of the XPS image obtained from (2) is now changed to a binding-energy scale, and this results in horizontal XPS features. The one-dimensional XP spectrum can be obtained from averaging the resulting image along the photon energy axis. Further, this 1D XP spectrum is used to get an XPS image but this time with smeared out NEXAFS features. (4) Subtracting the XPS image with smeared out NEXAFS features, obtained from (3), from the measured images gives an improved image, that can be used in (1) to repeat the four steps iteratively. If the XPS features in the measured image are particularly strong the iterative process can be started at Step 3 instead of Step 1.

An example of this procedure applied to a real measured image is shown in Figure 16. The example is a carbon K-edge measurement of phenylphosphonic acid on rutile TiO_2(110) – (1 × 1) acquired at 80° with respect to the surface normal. Noteworthy, all angles given here and in the publications are respective to the surface normal.

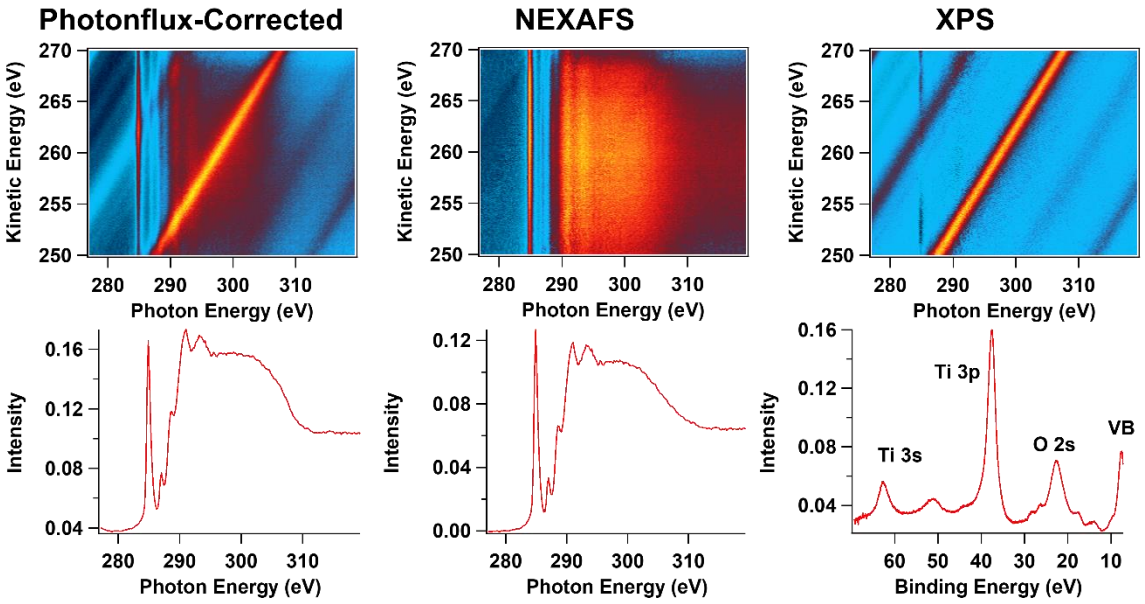

Figure 16 80° grazing incidence, carbon K-edge measurement of phenylphosphonic acid on TiO_2(110) – (1 × 1) after annealing at 400 K. Shown are the photon-flux-corrected measured image as well as the NEXAFS and XPS images and spectra after applying 30 iterative cycles of the cleanup procedure. The procedure was started at step 3 since the photoemission line is quite pronounced in the as measured image. The results show that the procedure worked nicely and removed all photoemission contributions from the NEXAFS image, although as can be seen from the two NEXAFS spectra the relatively strong photoemission feature had a surprisingly small effect on the one-dimensional spectra.

As mentioned in literature [107], the simplified description of the cleanup procedure ignores several important effects, such as changing photoemission cross sections and different escape

depths of photoelectrons. Also, modifications of the Auger spectra by effects, including resonant excitation and participator and spectator Auger decay, as depicted in Figure 14, are neglected [107]. Even though several effects are neglected, the results are very good [107]. Further approaches to overcome the mentioned challenges are described in literature [101, 106].

3. Results and Discussion

3.1. 4-Cyanophenylporphyrins on Cu(111) [P1]

3.1.1. Adsorption Structure of 4-Cyanophenylporphyrins

During my Bachelor thesis, I already studied the reactions of free-base tetraphenylporphyrin (2HTPP) on Cu(111). In the following years, three different reactions were found for 2HTPP on Cu(111) [16, 68, 108-113]: (1) self-metalation, the process of inserting copper atoms from the Cu(111) surface into the porphyrin macrocycle, (2) ring fusion, the bond formation between the pyrrole rings and the phenyl rings by a dehydrogenation reaction, and (3) finally complete dehydrogenation of the periphery of the molecule. (1) and (2) are strongly coverage-dependent; and upon deposition of coverages close to one molecular layer, a complex checkerboard-like structure is formed on the surface.

This inspired me to work on the first project for my PhD thesis, where we investigated three functionalized tetraphenylporphyrins on Cu(111) with 1, 2 and 4 cyano groups, see Figure 17. Cyano groups are chosen, because they can induce surface-supported molecular structures [114, 115] as well as acting as electron-withdrawing groups.

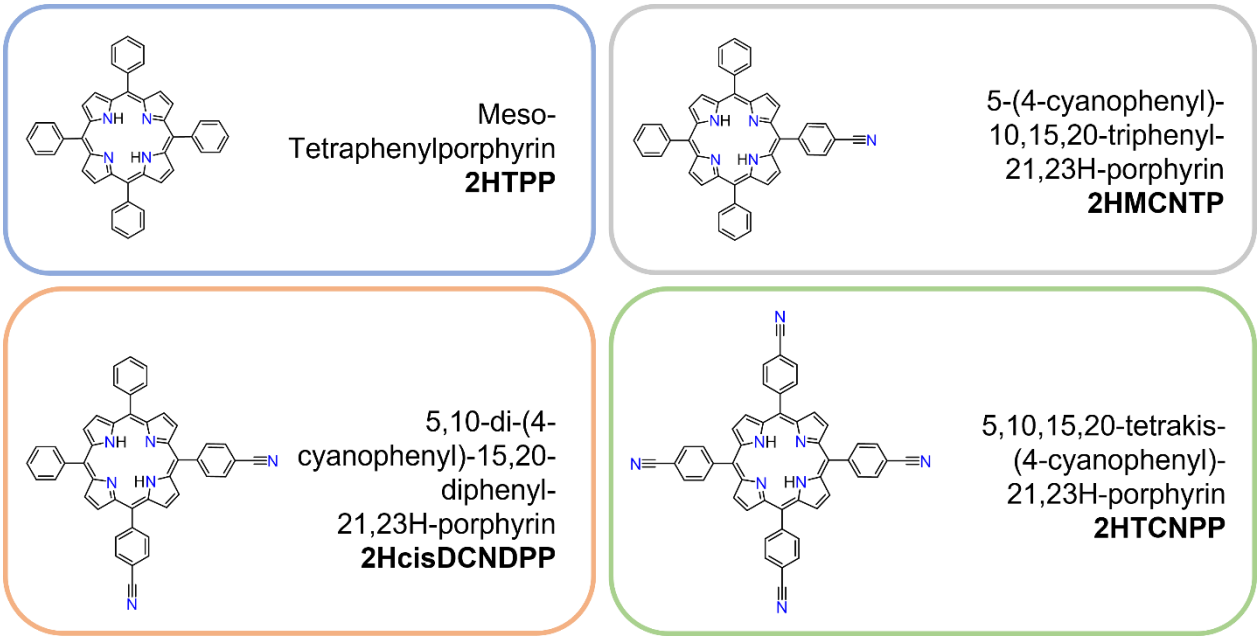

Figure 17 Structures of the non-functionalized and cyano-functionalized tetraphenylporphyrins studied in this thesis.

Figure 18 shows our STM images of the three different CNTPPs on Cu(111) as deposited at 300 K and after annealing to 400 K. As deposited at 300 K the molecules are somewhat disordered on the surface, but annealing results in the formation of molecular chains: This is especially visible

for 2HTCNPPs with four cyano groups where longer chains are formed, but less apparent for 2HMCNPP with only one cyano group where dimers are formed.

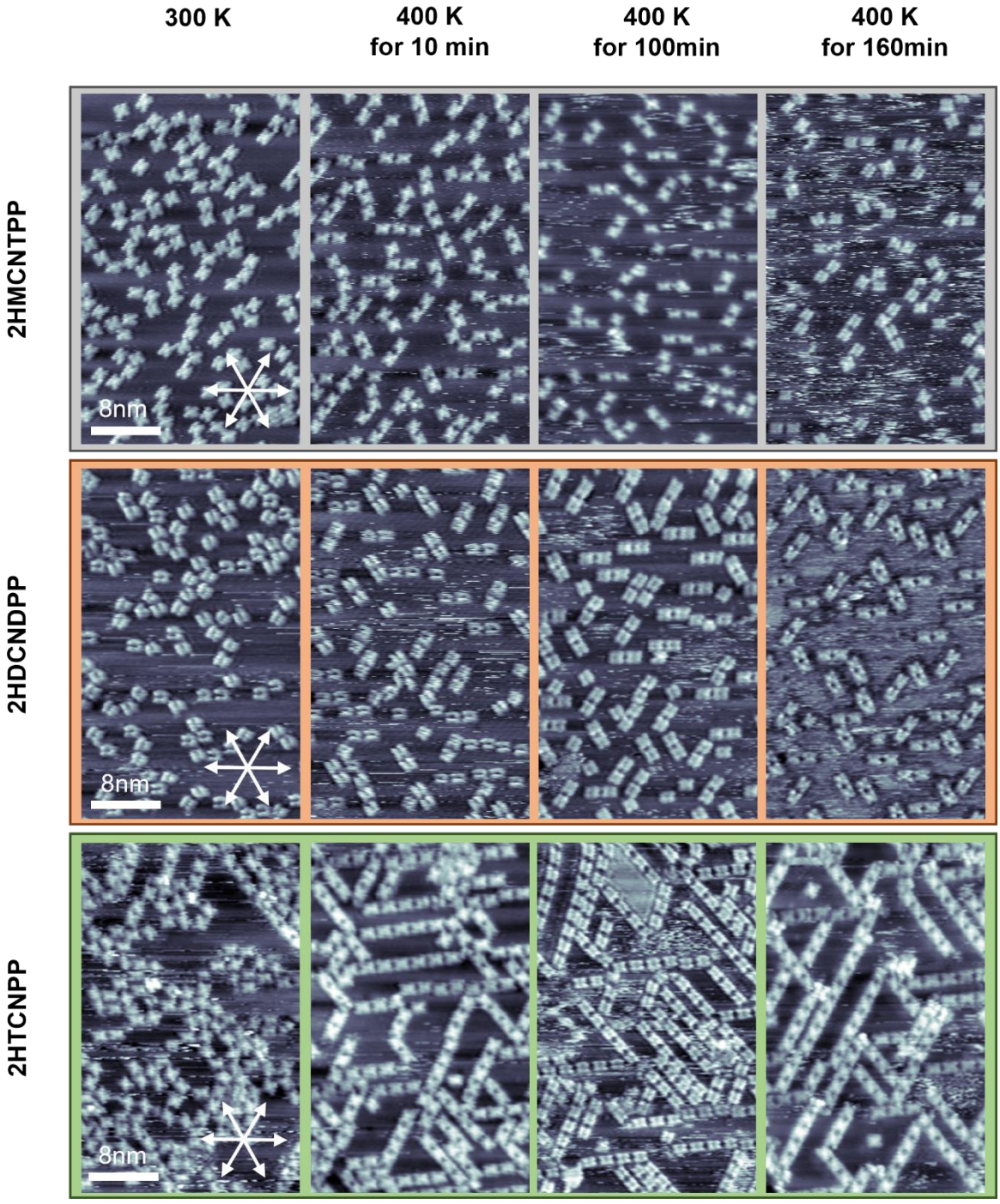

Figure 18 STM images of 2HMCNTPP (first row, grey), 2HcisDCNDPP (second row, orange), and 2HTCNPP (third row, green) on Cu(111) with a coverage of 0.16 molecules/nm^2 (equivalent to roughly 0.32 ML) were acquired at room temperature, before and after annealing at 400 K for in total 10, 100 and 160 min. The formation of a 2D gas phase and the decreasing number of immobile molecules with annealing time is most dominant for 2HMCNTPP and 2HcisDCNDPP. Details about the acquisition parameters can be extracted from the supporting information of the paper [P1]. This Figure was adapted and printed with permission from [P1].

The intermolecular bond distances of the dimers and chains were found to be too long for carbon-carbon bonds. Further, nitrogen atoms in two neighboring cyano groups would be expected to repel each other, so cyano-cyano bonds are not expected, but the bond lengths fit with those expected for CN-Cu-NC bonds [114, 116, 117]. Similar CN-Metal-NC bonds were previously observed for functionalized polyphenyls, such as dicarbonitrile-polyphenyl on Cu(111) and Ag(111) [114, 117, 118]. Further, also for cyano-functionalized porphyrins CN-Metal-NC bonds were observed by Bischoff et al. [116] for tetra[(4-cyanophenyl)phen-4-yl]porphyrin on Ag(111) and by Fendt et al.[115] for cis-bis(4′-cyanobiphenyl)-substituted Zn(II) porphyrins on Cu(111). In case of Ag(111), co-deposition of copper, iron or cobalt was necessary to form CN-Metal-NC chains [117]. We, therefore, attribute the chain formation in Figure 18 to Cu adatom induced linkages between cyano groups of neighboring porphyrin molecules. Further binding motives, presumably dictated by hydrogen bonding or dipole-dipole interactions, were found for all cyanoporphyrins in particular at room temperature [P1][119].

As apparent from Figure 18, heating is required in order to form the chains. This could be because heating is necessary for the copper adatoms to be created or because heating is required for the strongly-interacting molecules in the “inverted structure” [119, 120] to become mobile.

3.1.2. Self-Metalation of 4-Cyanophenylporphyrins

Noteworthy, the STM images in Figure 18 show stripy, noisy features in between the island structures upon annealing to 400 K. At the same time the number of apparent molecules on the surface decreases, even though 400 K is too low for desorption [13, 111, 112]. The appearance of stripy features is indicative of highly-mobile molecules on the surface.

On Cu(111) free-base 2HTPP has previously been observed to be comparably immobile at room temperature, because of strong bonds formed between the iminic nitrogen atoms and the copper surface [108, 109]. For CuTPP, however, the interaction between the nitrogen atoms and the substrate is lifted. Thus, the molecules become highly mobile, form a 2D gas phase and are imaged as stripy features in STM [113, 121]. This is exactly what we observe for our cyanoporphyrins after annealing. We therefore expect the stripy features to be caused by metalated molecules. Noteworthy, the CuTPP molecules in the 2D gas phase only show the appearance of individual molecules after cooling the sample to 200 K for the un-functionalized CuTPP [122].

The explanation for this observation is related to the interplay between (1) the inter- and intramolecular molecule-molecule and (2) the adsorbate-substrate interactions that mainly dictate

the formation of surface structures. Previously, in agreement with literature, we found that 2HTPP on Cu(111) forms strong site-specific interactions with the surface, and that this leads to a distortion of the porphyrins macrocycle, so that the two opposing pyrrole rings are tilted by 100° with respect to the surface plane, forming a strong bond between the iminic nitrogen atoms and the copper surface. Further, the phenyl rings are oriented almost parallel to the surface, what is expected to hinder intermolecular T-type and π- π interactions between molecules. This intramolecular structure is called the “inverted” structure [123, 124].

Our STM results, supported by DFT calculations [119, 123][P1], suggested that all cyano-functionalized porphyrins also adopt this “inverted” structure over a wide bias voltage range, independent of polarity.

The analysis of the images shown in Figure 18 already shows that the number of molecules decreases with annealing time [P1]. Upon annealing to 400 K for 160 min 2HMCNTPP shows the most pronounced decrease in the apparent number of molecules visible on the surface.

To quantify the rate of the metalation, we used the approach by Ditze et al. [121]. They counted individual non-metalated molecules from STM images after well-defined heating steps. This enabled us to quantify the number of metalated molecules indirectly. From isothermal heating experiments with four different temperatures and an Arrhenius analysis, Ditze et al. [121] learned about the reaction kinetics and activation barriers of 2HTPP on Cu(111).

To determine the rate of the metalation reaction of our cyano porphyrins on Cu(111) with respect to 2HTPP, we counted the number of stationary molecules on the surface as a function of annealing time. In total, 15,000 to 20,000 molecules for each molecule were counted to get representative data points with a sufficiently small error bar. The rate of metalation of the three cyano porphyrins as well as the unsubstituted tetraphenylporphyrin can be derived from Figure 19. The results show a strong correlation between the number of cyano groups in the tetraphenylporphyrin molecule and the decrease in metalation rate. In the extreme case of the four cyano groups in 2HTCNPP, in comparison to the unsubstituted 2HTPP, the metalation rate decrease by a factor of 22.

Noteworthy, conducting experiments with the metalated CuTCNPP also showed that the Cu porphyrins appear differently in the STM images compared to the free base porphyrins and this proves that the molecules in the linear chains are not metalated. In addition, the apparent free base molecules do not change the molecular conformation upon annealing at 400 K as expected for metalloporphyrins.

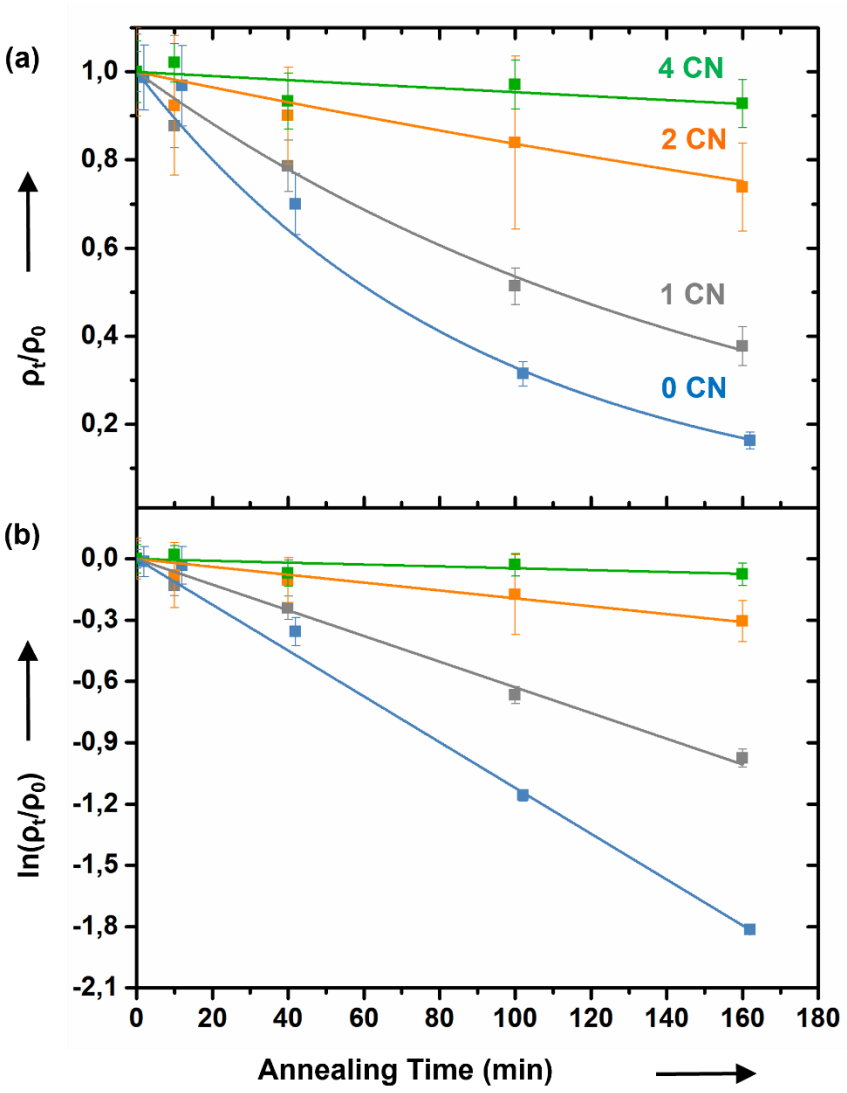

Figure 19 Plots depicting the development of the normalized coverage of free-base porphyrin (reactant) with annealing time at 400 K (a) on a linear and (b) on a logarithmic scale. From these the metalation rate was deduced: 2HMCNPP (grey), 2HcisDCNPP (orange), and 2HTCNPP (green) compared with 2HTPP (blue).

For the cyano-functionalized porphyrins several follow-up scanning tunneling microscopy experiments were already performed in the group of Hubertus Marbach and their cooperation partners in Brasil [125-128]. For example, in 2020, vacuum-deposited copper-metalated and free-base cyano-functionalized tetraphenylporphyrins on Cu(111) were studied by Adhikari et al. [125]. They found that two-dimensional networks were formed for CuTCNPP and CucisDCNPP for submonolayer coverages. Different adsorption structures as a function of temperature were found by hydrogen bonding and also cyano-metal bonds. Only one year later, free-base tetracyanophenyl tetrabenzoporphyrin on Cu(111) were studied by scanning tunneling microscopy and three types of network structures were observed on the surface by Adhikari et. al. [126].

3.2. Tetraphenylporphyrin on TiO_2(110) - (1 × 1) [P2]

Inspired by our findings on metal surfaces on molecular conformation, adsorption structure and surface reactions, in the recent years, we extended our knowledge to more complex surfaces, such as oxides. When we talk about complexity, we refer to a more difficult surface structure, such as the oxygen row structure on rutile TiO_2(110) - (1 × 1) and the defects, such as oxygen vacancies that occur upon annealing in ultrahigh vacuum.

The adsorption and self-metalation of tetraphenylporphyrin on rutile TiO_2(110) - (1 × 1) was studied by X-ray photoelectron spectroscopy (XPS) and scanning tunneling microscopy (STM). The left panel of Figure 20 shows the XP spectra of subsequently deposited 2HTPP on TiO_2(110) - (1 × 1) at room temperature up to two layers. Only one surface species is observed for the first 80 to 90 % of a molecular layer. Upon further increasing the coverage to roughly two layers, two well-known additional peaks in the N 1s XP region, with a 1:1 ratio, were observed. We compare these high-coverage N 1s peaks to the peaks of free-base tetraphenylporphyrin from literature [12, 13, 16], with its two aminic (**-**NH-) and two iminic (-N=) nitrogen atoms, and we conclude that they are in perfect agreement. Thus, we learn that the free-base tetraphenylporphyrin adsorbs intact in the second layer.

In the next step, we assign the submonolayer-coverage species: As depicted in Figure 20, we observe only one nitrogen species from the N 1s XP spectra. That means, that all detected nitrogen atoms at the surface are chemically equivalent. This is typically a sign of a metalated porphyrin molecules, because in a metalloporphyrin all four nitrogen atoms are bound to the metal center and thus appear chemically equivalent in XPS [12, 13]. Metalation of free-base 2HTPP has previously been observed on several oxide surfaces, such as MgO(100) [129, 130], Co_3O_4(111) [131] and oxygen-terminated CoO(111) [131] at room temperature.

In the following, we asked ourselves: Does 2HTPP metalate on TiO_2(110) at room temperature. If yes, what species would be formed, and what would the N 1s XP spectra of this species look like? To find the answers to these questions, we gathered information about titanium complexes and their stability: Typically, the metal center in the porphyrin pocket has a 2+ oxidation state, but for titanium the 2+ oxidation state is very unstable, especially in the presence of oxygen [132]. Thus, Ti^{2+} is unlikely to be formed. The most stable titanium complexes are in a 4+ oxidation state. Thus, we propose titanyl $(Ti{=}O)^{2+}$ porphyrin as the most probable species formed on TiO_2(110) - (1 × 1).

Inspired by these considerations, we addressed these questions by preparing 1.0 ML of (Ti=O)TPP on TiO_2(110) - (1 × 1), see bottom Figure 20, as a reference. The conclusion was that the surface species for the as-deposited 2HTPP on TiO_2(110) is not titanyl porphyrin, since the binding energy position is completely different.

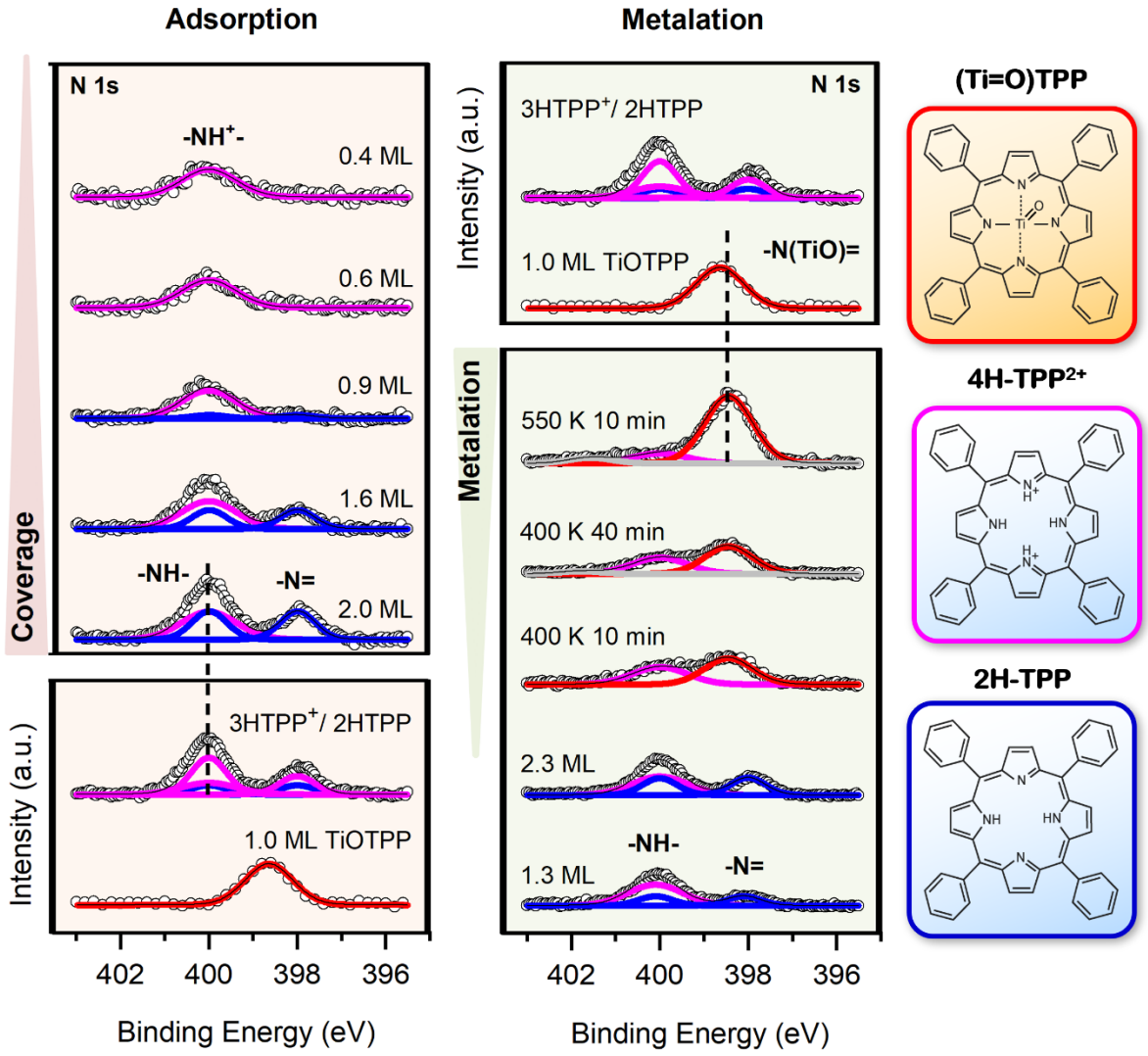

Figure 20 N 1s XP spectra of different coverages of vacuum-deposited 2HTPP on TiO_2(110) - (1 × 1) at room temperature. Further, N 1s spectra of 2.3 ML of 2HTPP after annealing at 400 K and 550 K are shown. Reference spectra of 1.0 ML (Ti=O)TPP on TiO_2(110) and multilayers of liquid-deposited mixture of porphyrin acid chloride and porphyrins ($3HTPP^+$/2HTPP) on Au-coated silica are shown for comparison. Molecular Drawings of 2HTPP, $4HTPP^{2+}$ and (Ti=O)TPP are depicted in addition.

From Figure 20, it is clear that the position of the submonolayer N 1s species is at the same binding-energy position as the aminic (-NH-) nitrogen atoms of the free base molecule. In addition, it is well-known from liquid-phase chemistry that a protonated porphyrin diacid species $4HTPP^{2+}$ is formed for pH values < 3 [133]. To clarify, whether the same species is formed on the TiO_2(110)

surface, we performed a reference measurement of wet-chemically prepared 5,10,15,20-tetraphenylporphyrin diacid chloride, see Figure 20. This measurement shows that a protonated $4HTPP^{2+}$ molecule is fully consistent with the submonolayer species found for 2HTPP on TiO_2(110). This was also suggested by Lovat et al. [134], who were the first to observe the single peak for deposited 2HTPP on TiO_2(110) - (1 × 1).

But where do the protons come from? One source of protons that is almost always present on the TiO_2(110) surface is OH groups. These are created upon adsorption and dissociation of water molecules from the residual gas, see Chapter 2.1. From the XP spectra, 0.8 ML of 2HTPP is found to be fully protonated and for this double the amount of OH groups are necessary. 0.8 ML of 2HTPP equals roughly 0.40 molecules/nm^2 [12, 135, 136] and one oxygen vacancy can create two OH groups upon adsorption and dissociation of water molecules [30, 137]. From this, 0.40 oxygen vacancies/nm^2 (~8%) are expected to be necessary to cause the observed effect. The estimated value is in the range expected for vacuum-prepared TiO_2(110) - (1 × 1) surfaces and could therefore fully explain this effect. However, Lovat et al suggested bulk-dissolved hydrogen atoms to be the hydrogen source [134, 138].

In the next step, 2.3 ML 2HTPP were prepared on TiO_2(110) and annealed to 550 K, see Figure 20, and a new single N 1s peak was observed. The position of the new peak this time agrees well with the titanyl-porphyrin reference, and we therefore assign this process to metalation. The onset of metalation was already found at 400 K. However, at 400 K only the free-base porphyrin was found to be metalated, while the diacid species was still intact. This suggested that the diacid species is more resistant towards metalation, while the unprotonated molecules in the second layer are already metalated.

We base the assignment exclusively on the N 1s binding energy position, but most metalloporphyrins have similar N 1s binding energy positions. To strengthen our assignment, we attempted to desorb the metalated species into a mass spectrometer but were unsuccessful. A definitive assignment therefore remains elusive from our results.

Lovat et al. also studied the self-metalation reaction of tetraphenylporphyrin on TiO_2(110) [138, 139] and they bring up the idea that titanium atoms were extracted from the substrate upon annealing and incorporated into the macrocycle. They also tried to approach the question on the self-metalated species by co-deposition of titanium onto one monolayer of tetraphenylporphyrins on TiO_2. The result was a peak at the same binding energy as the self-metalated species [138].

When we compare our results to the studies on other oxides, such as MgO(100) [129, 130], Co_3O_4(111) [131] and oxygen-terminated CoO(111) [131], the most outstanding differences are that on other oxides at room temperature no protonated species was observed for submonolayer coverages, and instead metalation occurred at room temperature. We presently think that is related to the oxidation state of the metal atom. While magnesium and cobalt atoms are present in 2+ oxidation state, titanium possess a 4+ oxidation state. Further, we know from liquid-phase studies that the coordinated metal atom in the metalloporphyrins is usually 2+. So, for MgO(100), magnesium is easily available in 2+ state at edges, ready to be coordinated, while on the TiO_2(110) surfaces the situation is more complex and ions are expected to be only available upon annealing.

3.3. Anchoring Organic Molecules to Rutile TiO_2(110) - (1 × 1) Surfaces [P3, P4]

Motivation for Phosphonic and Hydroxamic Acids as Anchoring Groups

The phosphonic acid anchor group was found especially interesting, since it forms very stable bonds with oxide surfaces, such as TiO_2. The bonds were found to be even stronger than that of the carboxylic acid anchor group. Thus, molecules cannot easily be removed by solvents used in practical applications, and usage of phosphonic acid can improve the long-time stability of several applications. One noteworthy drawback is for example the loss in efficiency in the case of dye-sensitized solar cells for present investigations, since the electronic structure at the interface seems too unfavorable [140].

The benzohydroxamic acid, another interesting anchoring group, was compared to carboxylic acid and similar electronic properties were found. The bond was found stronger, especially in the basic regime, and also more resistant towards hydrolysis. Thus, the hydroxamic acid anchor group is found equally or partly more suitable for many applications compared to a carboxylic acid anchor group [141-144].

In the scope of this thesis, anchoring groups with phenyl rings were chosen as model molecules to extend the knowledge about the anchoring of organic molecules onto oxide surfaces, such as on rutile TiO_2(110) - (1 × 1) surfaces. In this context, especially the influence of the respective anchoring groups was addressed. Phenylphosphonic acid and benzohydroxamic acid were vacuum-deposited on TiO_2(110) - (1 × 1) surfaces and important surface properties such as the binding mode and/or molecular geometry were studied applying photoelectron and photoemission-based techniques.

3.3.1. Phenylphosphonic Acid on Rutile TiO_2(110) - (1 × 1) Surfaces [P3]

The Binding Mode of Phenylphosphonic Acid

The binding mode of phenylphosphonic acid on a TiO_2(110) - (1 × 1) surface was studied with synchrotron-radiation photoelectron spectroscopy. All experiments were performed at the synchrotron and thus, the kinetic energy of the electron was tuned especially low to achieve high surface sensitivity. Furthermore, in comparison to lab-source measurements, at the synchrotron the energy resolution is far better. For the O 1s spectra, the entrance and exit slits widths were

decreased to get an even higher resolution as compared with larger slits widths for the same photon-energy range.

2.7 ML of phenylphosphonic acid multilayers were prepared on TiO_2(110) - (1 × 1) by vacuum-deposition. Ti 2p, C 1s, P 2p and O 1s XP spectra were acquired, as depicted in paper [P3]. Upon annealing to 380 K, the substrate signals increase, while the molecule signals decrease. This indicates multilayer desorption. Higher annealing temperatures did not affect the spectra, indicating the formation of a compact, intact phenylphosphonic acid monolayer that is stable up to 780 K.

We assigned the binding modes of phosphonic acid on TiO_2(110) - (1 × 1) by evaluating the high-resolution O 1s XP spectra in Figure 21. The data was fitted with four peaks, one substrate peak at 530.4 eV, and three molecule peaks at 531.6, 532.7 and 533.8 eV.

To understand the heat-induced changes of the phenylphosphonic acid monolayer on TiO_2(110) - (1 × 1), it is very helpful to illustrate how the different binding modes from literature [140, 145] would look like in O 1s XP spectra, see Figure 21. For the monodentate binding mode, upon deprotonation of the P-OH group, one P-O-Ti bond and one Ti-OH group are formed. For the bidentate binding mode, two subclasses exist, the onefold-deprotonated and the twofold-deprotonated bidentate binding mode. For the onefold-deprotonated bidentate binding mode, an additional P-O-Ti bond is formed upon interaction of the P=O with the surface, resulting in two P-O-Ti bonds, one Ti-OH bond and one P-OH bond. For the twofold-deprotonated bidentate binding mode, both P-OH groups are deprotonated when forming the two P-O-Ti bonds and two Ti-OH groups, while the P=O bond is still intact. Finally, the tridentate binding mode consists of three P-O-Ti bonds and two Ti-OH surface groups.

The O 1s XPS binding-energy positions for the different species extracted from our measurements agree very well with the values found in literature [145-150], especially with the peaks observed by Wagstaffe et al. [151]. The assignment was thus done in the following way: the peak at 533.8 eV was assigned to P-OH, the peak at 532.7 eV to P=O, and the peak at 531.6 eV corresponds to P-O-Ti overlapping with Ti-OH. The expected ratios, from high to low binding energy, are thus, 1:1:2 for monodentate, 1:0:3 for onefold-deprotonated bidentate, 0:1:4 for twofold-deprotonated bidentate and 0:0:5 for tridentate.

The temperature development can be divided again in three parts. The first part from 430 to 460 178.44K, results in a 1.0:1.0:2.1 ratio for the P-OH:P=O:(P-O-Ti + Ti-OH) components, as summarized in Table 4. A comparison of the experimentally determined ratio with the expected

ratios, as shown in Figure 21, indicates that the binding mode of phenylphosphonic acid is dominated by the monodentate configuration.

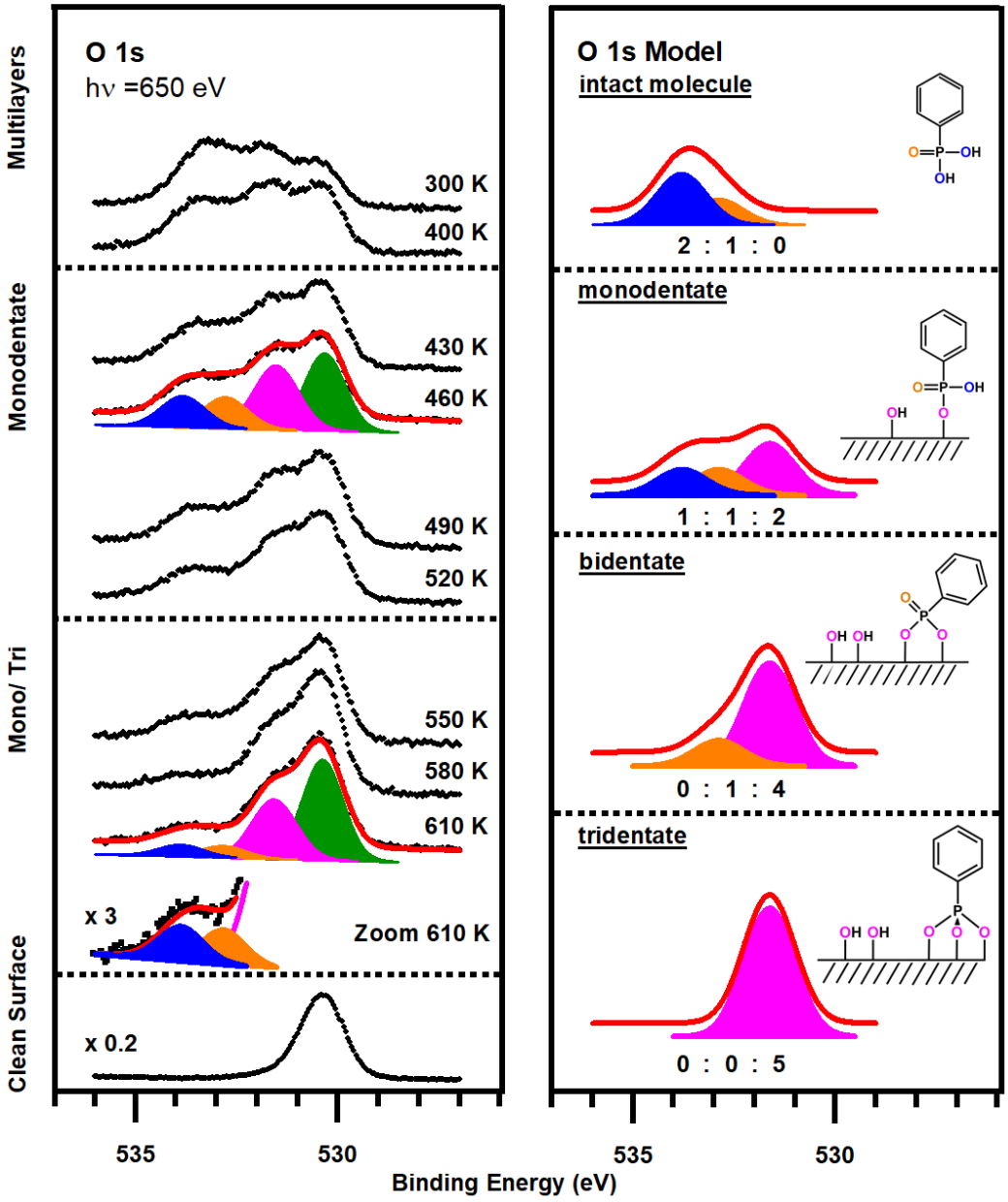

Figure 21 High-resolution O 1 s XPS spectra of phenylphosphonic acid deposited on TiO_2(110) - (1 × 1), followed by incremental annealing steps, measured with a photon energy of 650 eV. Schematic sketch of the different binding configurations of phenylphosphonic acids to oxide surfaces with the corresponding schematic XP spectra.

The second temperature region is a transition region from 490 to 520 K that finally results in the third region, another plateau with similar curve shapes. In the transition region, the P-OH and P=O species at the high-binding-energy shoulder decrease, while the P-O-Ti/Ti-OH peak remains constant, and the substrate peak intensity increases.

For the resulting third region, the extracted peak ratio is 1.3:1.0:5.8. This ratio can be explained either by an equal mixture of onefold- and twofold-deprotonated bidentate species, resulting in 1:1:7 ratio, or by an equal mixture of monodentate and tridentate species, also resulting in a 1:1:7 ratio. The deviation between the experimentally determined ratio and the expected theoretical ratios is most likely related to a loss of Ti-OH groups. According to literature recombination of two Ti-OH groups at defect sites results in the desorption of water in this temperature range [152-154]. This correlates with a decrease of the Ti-OH signal and an increase of the substrates signal. In addition, the desorption results in unoccupied surface sites, and this could be the driving force to form bidentate or higher binding mode configurations. Assuming partial loss of OH groups upon annealing, the expected 1:1:7 ratio would decrease and could approach the observed ratio.

Table 4 O 1s peak positions of substrate and adsorbate signals (with an error of +/-0.1 eV), and their relative contributions to the total signal.

	P-OH	P=O	Ti-OH/ P-O-Ti	TiO_2
Binding Energy	533.8 eV	532.7 eV	531.6 eV	530.4 eV
FWHM	1.19 eV	1.19 eV	1.19 eV	1.18 eV
Contribution to O 1s signal 430 – 520 K	15 %	15 %	31 %	39 %
Contribution to O 1s signal 580 – 610 K	7 %	5.5 %	32 %	55.5 %

Presently, in agreement with further studies on similar molecules on TiO_2(110), the bidentate binding mode is favored [155-157]. Studies about methyl phosphonate on rutile TiO_2(110) by Pang et al. [155] included DFT calculations, which showed that both monodentate and onefold-deprotonated bidentate are less stable than the twofold-deprotonated bidentate binding mode. Further DFT studies by Skibinski et al. [156] proposed the twofold-deprotonated bidentate binding mode as the most favored one. Further theoretical calculations predicted, that both bidentate species were calculated to have a comparable stability, and this would be in agreement with the approximate 1:1 ratio between the two bidentate species [157]. The tridentate binding mode was even calculated to be unfavored on an ideal TiO_2(110) surface [157]. Thus, this third region from 550 to 610 K is called the mixed-bidentate region.

Carbon K-edge-NEXAFS and How to Extract Adsorption Angles

To gain insights into the dependency of the molecular electronic structure on the temperature-dependent changes of the binding mode, valence-band photoemission spectra and NEXAFS spectra were acquired. Valence band spectra (shown in [P3]) give information on the occupied states while NEXAFS spectroscopy addresses the unoccupied states.

For the phenylphosphonic acid monolayers, prepared on TiO_2(110) with subsequent annealing steps, C K-edge NEXAFS spectral images were acquired. The C K-edge NEXAFS spectral images were measured for five different polar angles and two different azimuthal angles, 0° and 90° with respect to the [001] crystallographic directions, to reveal the angle dependence of the respective transitions. Noteworthy, the polar angles are given relative to the surface normal. Thus, 0° refers to normal incidence for the linear-polarized light and an electric-field vector parallel to the substrate, and 80° is grazing incidence of the incoming light and an electric-field vector close to perpendicular to the substrate surface.

Since both the X-ray optical elements of the beamline and the gold mesh that is used for photon-flux measurements were strongly contaminated with carbon, the measured C K-edge NEXAFS images had to be normalized to a photon flux. However, the gold mesh current could not be used. Instead, the intensity of the Ti 3p peak was measured in the same photon energy range as the C K-edge NEXAFS images and used as the photon flux.

Furthermore, photoemission peaks were removed from the spectral images by applying the clean-up procedure for Auger-yield NEXAFS as described by Lytken et al. [107] and in the NEXAFS section of this thesis. In Figure 22, the obtained C K-edge NEXAFS spectra were grouped into four different panels according to their annealing temperature and azimuthal angle. For each group of temperature and azimuthal angle, the measurements at five different polar angles are shown. The spectra in panel 1 and panel 2 were measured after annealing at 380 K with an azimuthal angle of 0° and 90°, respectively. The spectra in panel 3 were acquired after annealing at 780 K with an azimuthal angle of 0° and those in panel 4 after annealing at 650 K with an azimuthal angle of 90°. The spectra in panel 1 and 2 refer the temperature range where phenylphosphonic acid is expected in the monodentate binding mode, while the spectra in panel 3 and 4 are assigned to the mixed-bidentate (or monodentate plus tridentate) configuration. Noteworthy, all temperatures had to be corrected, because the originally measured temperatures were overestimating the real crystal temperatures by 200 to 300 K dependent on the sample mounting. For improvement of sample mounting and temperature acquisition see Chapter 2.4.2.

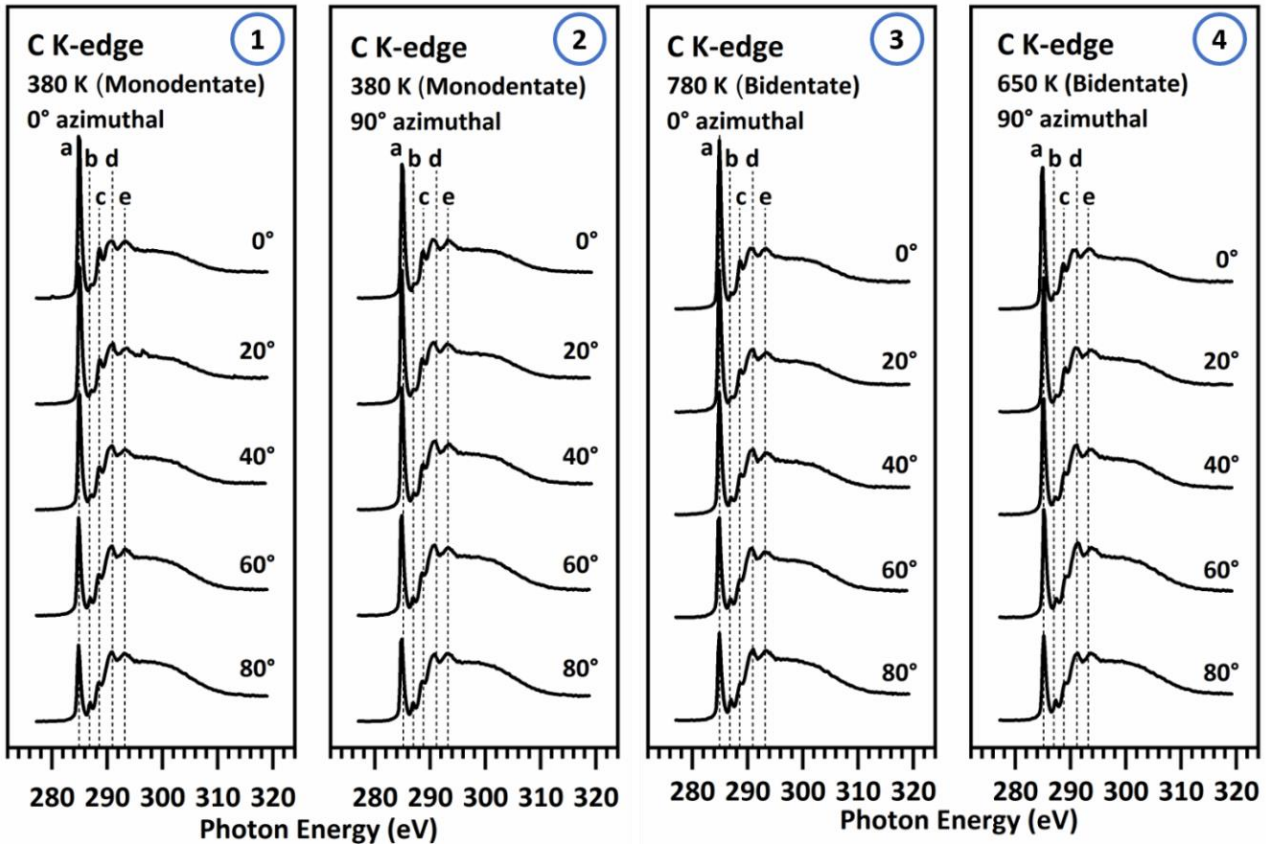

Figure 22 NEXAFS C K-edge spectra of a monolayer of phenylphosphonic acid on TiO_2(110) after annealing to different temperatures for five different polar angles and for two different azimuthal angles of the incoming radiation are depicted. Normal incidence corresponds to 0º incidence angle and grazing incidence to 80º. The panels 1 and 2 show the spectra after annealing to 380 K (monodentate) for 0° azimuthal and 90° azimuthal (with respect to the [001] direction), respectively. The panels 3 and 4 show the spectra after annealing to 780 K for 0° azimuthal and after annealing to 650 K for 90° azimuthal (with respect to the [001] direction), respectively. Differences in annealing temperatures are related to different sample mounting and resulting differences in temperature reading for the sample preparations.

Several distinct peaks are visible in the C K-edge NEXAFS spectra shown in Figure 22, correlating with electronic transitions from the C 1s core level to different unoccupied states: (a) a π* resonance at 284.9 eV, (c) a transition to a state related to a mixture of Rydberg and -CH σ* states at 288.6 eV, and σ* resonances at (d) 290.7 and (e) 293.2 eV [151]. The small peak (b) at 286.9 eV has also been detected in previous measurements of phenylphosphonic acid on an anatase surface and was assigned to be substrate-related [151]. Noteworthy, in comparison, phenylphosphonic acid on rutile TiO_2(110) and on anatase TiO_2(101) show a quite similar trend concerning the peak positions of the different transitions [151]. Comparing the C K-edge spectra for the different azimuthal angles and the annealing temperatures, overall, the spectra show the same transitions and are very similar.

Information on the orientation of molecules or parts of molecules can be obtained by angle-dependent NEXAFS spectroscopy, as acquired in Figure 22. Electron transitions from one orbital to another usually follow the selection rules, and thus for allowed transitions the orbital angular momentum changes by +1 or -1. As a result, from an s orbital, the only allowed transitions are to p orbitals. Considering only one molecule and perfectly linear-polarized light, the NEXAFS intensity for these transitions are dependent on the square of the scalar product of the electric-field vector $\vec{E}$ and the molecule orbital vector $\vec{O}$ [98, 145].

$$f(\theta_E, \varphi_E, \theta_O, \varphi_O) \propto \left(\vec{E}(\theta_E, \varphi_E) \cdot \vec{O}(\theta_O, \varphi_O)\right)^2 \tag{10}$$

θ_E and θ_O are the polar angles of the electric-field vector $\vec{E}$ and the molecular orbital vector $\vec{O}$ given relative to the surface normal, and $\varphi_O$and φ_E are the azimuthal angles for the respective vectors, given relative to a defined axis in the surface plane. The angles are also visualized in the scheme in Figure 23. In the following, this equation will be used as the basic building block to describe more complex situations, such as when the light is elliptically polarized and multiple molecular domains are formed [98, 145].

The components of the vectors can also be written as cosine and sine functions of the polar and azimuthal angles. Here the z direction is defined as normal to the surface.

$$\vec{E}(\theta_E, \varphi_E) = \begin{bmatrix} E_x \\ E_y \\ E_z \end{bmatrix} = \begin{bmatrix} \sin(\theta_E) \cdot \cos(\varphi_E) \\ \sin(\theta_E) \cdot \sin(\varphi_E) \\ \cos(\theta_E) \end{bmatrix}$$

$$\vec{O}(\theta_O, \varphi_O) = \begin{bmatrix} O_x \\ O_y \\ O_z \end{bmatrix} = \begin{bmatrix} \sin(\theta_O) \cdot \cos(\varphi_O) \\ \sin(\theta_O) \cdot \sin(\varphi_O) \\ \cos(\theta_O) \end{bmatrix}$$

Inserting the components, for equation 10 the following equation results

$$f(\theta_E, \varphi_E, \theta_O, \varphi_O) \propto \left(\vec{E}(\theta_E, \varphi_E) \cdot \vec{O}(\theta_O, \varphi_O)\right)^2 = \left(E_x O_x + E_y O_y + E_z O_z\right)^2 = \quad (11)$$

$$= (\sin(\theta_E) \cdot \cos(\varphi_E) \cdot \sin(\theta_O) \cdot \cos(\varphi_O) + \sin(\theta_E) \cdot \sin(\varphi_E) \cdot \sin(\theta_O) \cdot \sin(\varphi_O) + \cos(\theta_E) \cdot \cos(\theta_O))^2 =$$

$$= \sin^2(\theta_E) \cdot \cos^2(\varphi_E) \cdot \sin^2(\theta_O) \cdot \cos^2(\varphi_O) + \sin^2(\theta_E) \cdot \sin^2(\varphi_E) \cdot \sin^2(\theta_O) \cdot \sin^2(\varphi_O) + + \cos^2(\theta_E) \cdot \cos^2(\theta_O) +$$

$$+ 2 \cdot \sin(\theta_E) \cdot \cos(\varphi_E) \cdot \sin(\theta_O) \cdot \cos(\varphi_O) \cdot \sin(\theta_E) \cdot \sin(\varphi_E) \cdot \sin(\theta_O) \cdot \sin(\varphi_O) +$$

$$+ 2 \cdot \sin(\theta_E) \cdot \cos(\varphi_E) \cdot \sin(\theta_O) \cdot \cos(\varphi_O) \cdot \cos(\theta_E) \cdot \cos(\theta_O) +$$

$$+ 2 \cdot \sin(\theta_E) \cdot \sin(\varphi_E) \cdot \sin(\theta_O) \cdot \sin(\varphi_O) \cdot \cos(\theta_E) \cdot \cos(\theta_O)$$

The polarized light given at the synchrotron is usually not perfectly linear polarized. Thus, the Material Science Beamline at Trieste, a bending magnet beamline, produces elliptically polarized light with a polarization P of 0.8. To get the NEXAFS intensity, integration over all polarization direction would be necessary. However, this integral is also given by the sum of two contributions of linear-polarized light perpendicular to each other, one contribution along the long axis and one along the short axis of the ellipsoid. For a bending magnet, the long axis of the ellipsoid is in the plane of the storage ring, and this contribution is typically called $\overrightarrow{E^{\parallel}}$, and the short axis of the ellipsoid is perpendicular to the plane of the storage ring, and usually called $\overrightarrow{E^{\perp}}$. The geometry of the Materials Science beamline determines the $\overrightarrow{E^{\perp}}$, and with this azimuthal vector of $\overrightarrow{E^{\perp}}$ is always 90° rotated in comparison to the azimuthal vector of $\overrightarrow{E^{\parallel}}$, while the polar angle of $\overrightarrow{E^{\perp}}$ is always 90° to the surface normal. Therefore, the function g is derived by extending the equation 10:

$$g(\theta_E, \varphi_E, \theta_O, \varphi_O, P) = P \cdot f(\theta_E, \varphi_E, \theta_O, \varphi_O) + (1 - P) \cdot f(90°, \varphi_E + 90°, \theta_O, \varphi_O) \quad (12)$$

This equation is only valid for one molecule and needs to be extended to be valid for several molecules on a surface. To do this we need to know how many molecules form the unit cell of the adsorption structure. For now, we assume one molecule per unit cell. Even for this simplified case

several mirror domains will result on the surface. If the molecules adsorb with a polar angle of θ_O, two mirror domains will form: One with a polar angle of $+\theta_O$ and the other with a polar angle of $-\theta_O$. Further domains are induced by the twofold symmetry of the TiO_2(110) surface. If molecules adsorb with an azimuthal angle of $+\varphi_O$, there will always be the same number of molecules adsorbing with an azimuthal angle of $-\varphi_O$. Thus, the measured NEXAFS intensity becomes the average intensity of the four molecular domains [98, 145].

$$h(\theta_E, \varphi_E, \theta_O, \varphi_O, P) = \tag{13}$$

$$\frac{1}{4} g(\theta_E, \varphi_E, \theta_O, \varphi_O, P) + \frac{1}{4} g(\theta_E, \varphi_E, \theta_O, -\varphi_O, P) + \frac{1}{4} g(\theta_E, \varphi_E, -\theta_O, \varphi_O, P) + \frac{1}{4} g(\theta_E, \varphi_E, -\theta_O, -\varphi_O, P)$$

Please note that in special cases, such as the adsorption of the molecules along the surface normal or along the high symmetry axis of the substrate, the number of domains can be reduced. If another surface is used or a different adsorption structure occurs, this approach can also be applied, however, the number of mirror domains changes. With increasing symmetry, such as to three-fold, the number of domains generally increases. For the three-fold symmetric substrate 12 domains result, which is usually simplified by assuming the presence of all azimuthal rotations on the surface. The NEXAFS intensity now becomes an integral over all the azimuthal angles, resulting in the following equation:

$$h(\theta_E, \varphi_E, \theta_O, P) = \frac{1}{360°} \int_0^{360°} g(\theta_E, \varphi_E, \theta_O, \varphi_O, P) d\varphi_O \tag{15}$$

Noteworthy, in this approach it is assumed that all four domains contribute equally to the NEXAFS intensity, which is true when the X-ray beam is large in comparison to the domain sizes. However, if the beam size is small in comparison to the domain sizes the equation for a single domain needs to be used, since only a single domain is investigated during the experiment. If the beam size and domain size are comparable, evaluation becomes difficult, and a determination of adsorption angles is usually not possible.

The spectra as shown in Figure 22 were normalized to the edge jump, and the extracted π* peak areas were fitted assuming a twofold-symmetric substrate with four molecular domains. The results of the fits are depicted in Figure 23. The fitting results in a polar angle of 25° with respect to the surface normal and an azimuthal angle of 42° for the phenyl ring of the monodentate phenylphosphonic acid binding mode, as acquired at 380 K. The mixed-bidentate (or mono- and tridentate) binding mode showed a polar angle of 26° with respect to the surface normal and an azimuthal angle of 43° for the phenyl ring of the molecules.

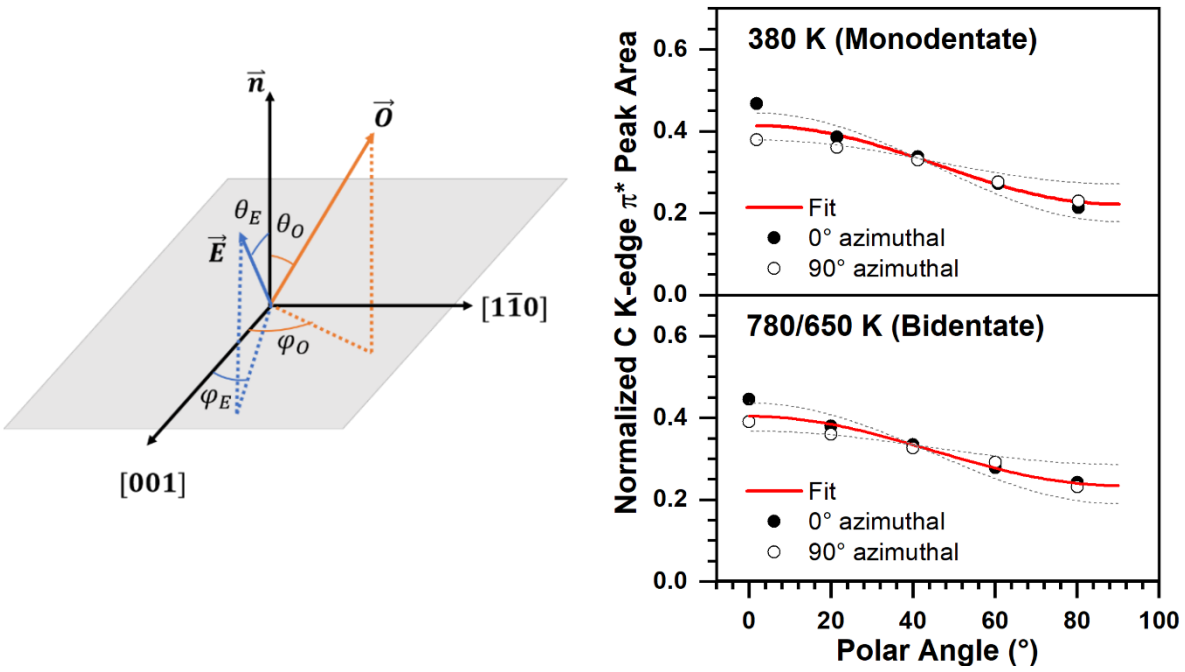

Figure 23 The angles for the electric-field vector $\vec{E}$ and the molecular orbital vector $\vec{O}$ are depicted in the scheme. The electric-field vector of the incoming light is described by the polar angle θ_E and the azimuthal angle φ_E. The molecular orbital vector is described by the polar angle θ_O and the azimuthal angle φ_O. The intensity of the π transition for different polar and azimuthal angles for phenylphosphonic acid on TiO_2(110) after annealing at 380 and 780/650 K are depicted. The data shown in Figure 22 was used. The extracted π* peak areas after normalizing to the edge jump were fitted applying the equation for twofold symmetric substrates with four molecular domains. These fits are shown in red while the dashed lines show fits with +/- 5° polar angles for comparison.*

Comparing the extracted polar angle with previous studies of phosphonic acid on rutile TiO_2(110) [156] and on anatase TiO_2(101) [151] shows that for all studies the molecules are neither upright standing nor flat lying. For the study by Skibinski et al. [156] one could estimate an angle from Figure 5 in Ref. [156], that is 37° with respect to the surface normal, which is very similar to the polar angle extracted here. On anatase TiO_2(101) [35], a polar angle of 25° relative to the surface normal was found. Noteworthy, the azimuthal angle of roughly 45° could either indicate, that the molecules align 45° relative to the [001] crystallographic direction or it could also mean that azimuthal orientation of the molecules is random.

We have unfortunately to denote here that Figure 23 (right) and the respective text related to the determination of polar and azimuthal angles had to be corrected and in [P3] the wrong version was printed originally. Figure 23 (right) and the angles are correct here and published in a Corrigendum related to [P3].

3.3.2. Hydroxamic Acid Linker Group on TiO_2(110) - (1 × 1) Surfaces [P4]

We studied the hydroxamic acid (see Figure 24, -C(=O)-N(-H)-OH) anchoring group on TiO_2(110) surfaces due to their interesting electron-transfer properties [22]. We addressed the adsorption properties of vacuum-deposited and liquid-deposited benzohydroxamic acid molecules on a clean TiO_2(110) - (1 × 1) surface under ultrahigh-vacuum conditions with synchrotron-radiation X-ray photoelectron spectroscopy (SRPES).

Figure 24 (top) shows the O 1s spectra for three different coverages of benzohydroxamic acid on a TiO_2(110) - (1 × 1) surface with and without substrate contribution, while Figure 24 (bottom) depicts O 1s XP spectra of benzohydroxamic acid and potassium benzohydroxamate powders. The O 1s XP spectra of the vacuum-deposited sample are described by two peaks, the titanium dioxide substrate peak at 530.1 eV and a second peak at 531.6 eV, assigned to the deposited molecules.

Comparing the powder and the vacuum-deposited spectra evidently only one molecule peak is visible in O 1s region after vacuum deposition. This would be consistent with the formation of a hydroxamate on the surface and should be accompanied by a surface Ti-OH groups, formed upon deprotonation of the N-OH group. Ti-OH groups are expected at 531.2-531.7 eV and will therefore overlap with the hydroxamate O 1s peak.

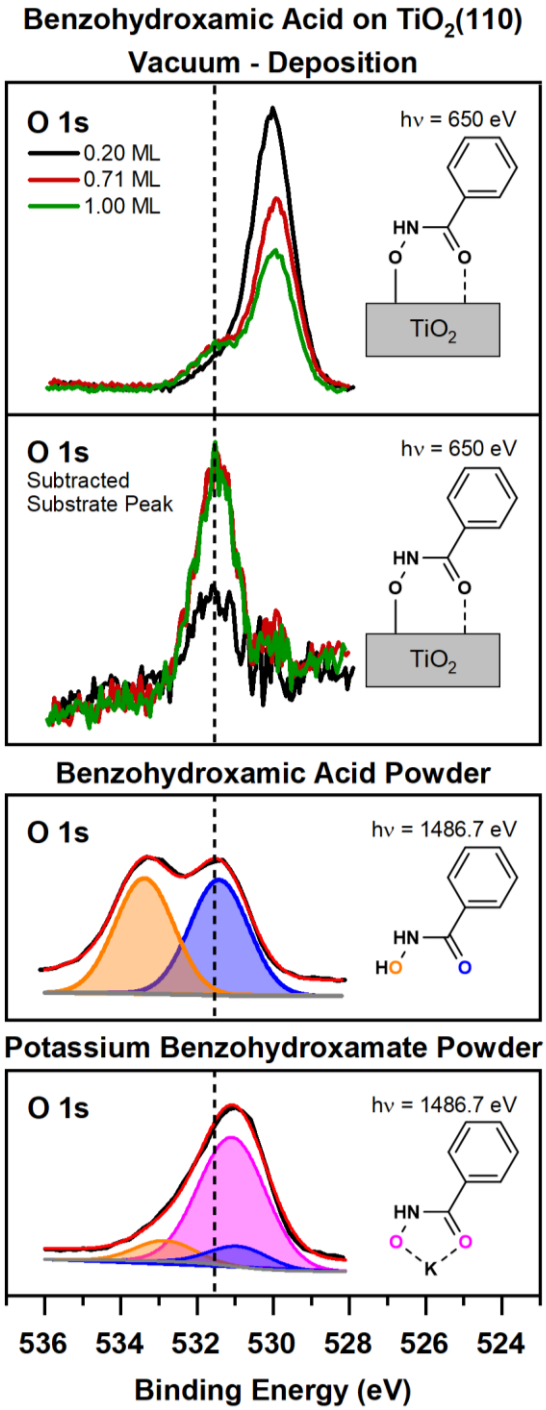

Figure 24 O 1s XP spectra for (top) vacuum-deposited benzohydroxamic acid on TiO_2(110) - (1 × 1) with and without substrate peak. O 1s XP spectra of the benzohydroxamic acid and potassium benzo-hydroxamate powder are shown for comparison.

Noteworthy, the adsorption of benzohydroxamic acid from vacuum-deposition is self-limiting at room temperature and the coverage saturates as shown in Figure 24 (top, green), because benzohydroxamic acid multilayer have a low evaporation temperature, close to room temperature. Noteworthy, the desorption of the multilayer was detected with temperature programmed desorption at 275 K. Thus, the maximum coverage that was reached upon vacuum-deposition at room temperature is referred to as one monolayer, also abbreviated with 1 ML.

For the same depositions, C 1s and N 1s spectra were acquired and depicted in Figure 25. The C 1s spectra show three species at 284.7, 287.6 and 289.4 eV. The peak at 284.7 eV is typically found for carbon atoms in a phenyl ring. The assignment of the peak at 287.6 eV as the hydroxamate group is supported by reference measurements of the two powders, the intact acid and the potassium benzohydroxamate, see bottom Figure 25, and literature values [158]. Comparing the C 1s peak at 289.4 eV to literature values, the binding energy is consistent with strongly oxidized carbon species, such as anhydride, lactone, orthoester or carbonate [159-163]. We think this species is a decomposition product, presumably formed at surface defect sites.

However, the N 1s spectrum at low coverage shows two features at 398.3 and 400.1 eV. The N 1s peak at 400.1 eV lines up with the N 1s peak of potassium benzohydroxamate. Thus, N 1s, C 1s and O 1s spectra agree on the formation of an hydroxamate. From density functional theory (DFT), the monodeprotonated bidentate bridging binding mode is the most stable. The second peak in the N 1s region at 398.3 eV is thus very likely related to the oxidized carbon species, presumably formed upon decomposition. Two possible options would be either a nitride-like species or atomic nitrogen [164, 165].

For high coverages, such as 0.71 and 1.00 ML, the feature at 287.6 eV (-N(H)-C(=O)-) dominates the C 1s spectra and the peak at 289.4 eV appears comparably weak. The N 1s spectra show a new species at 401.0 eV. In addition, the previously assigned hydroxamate peak shifts from 400.1 to 399.8 eV. From the O 1s one peak and thus only oxygen atoms with a similar chemical environment are observed. From this we conclude that the new N 1s high-binding energy species is most likely also a hydroxamate, but strongly shifted

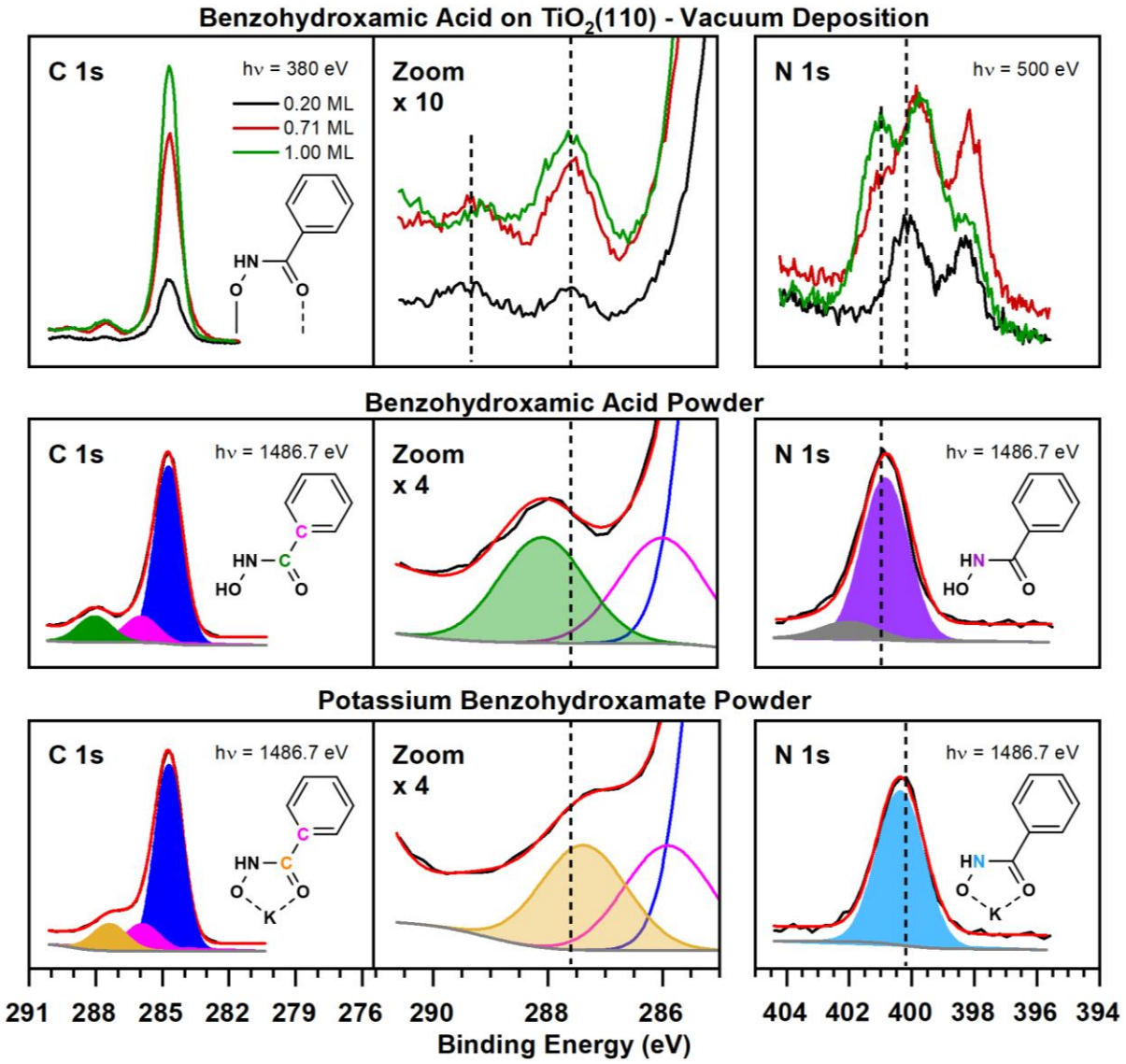

Figure 25 C 1s and N 1s XP spectra for benzohydroxamic acid deposited on TiO_2(110) - (1 × 1) at room temperature, see Figure 24 for the corresponding O 1s spectra. Reference spectra of benzohydroxamic acid powder and potassium benzohydroxamate powder are also included for comparison.

In addition, we compared vacuum-deposition to liquid deposition from ethanolic and acetonitrile solutions, see Figure 5 in [P4]. The main differences are in the N 1s spectra, where the solution-deposited structures lack the low-binding energy species we attribute to decomposition at defects. Specifically, oxygen vacancies would not be present on a surface exposed to air and liquid solutions. The defect responsible for the decomposition could therefore be oxygen vacancies.

Annealing series of the vacuum-prepared monolayer and the monolayer prepared from acetonitrile were performed and compared, see Figures 6 and 7 in [P4]. Interpretation of these annealing series is not entirely straight forward and gives the impression that the high-binding-energy species is bonded weaker to the surface as compared to the low-binding-energy species and

could thus be a monodentate-bonded species. Additional hydrogen bonding could explain the high binding energy N 1s species at high coverages at 401.0 eV, even though, compared to literature, hydrogen bonding to the nitrogen is assumed less likely than to the oxygen atoms. However, the exact assignment remains elusive and further experiments would be required. This is, however, out of scope of our present study and might be continued in the future.

4. Summary

In the present thesis, scanning tunneling microscopy (STM), X-ray photoelectron spectroscopy (XPS) and near-edge X-ray-absorption fine-structure spectroscopy (NEXAFS) were applied to study the adsorption behavior of organic molecules on single crystal surface under ultrahigh-vacuum conditions.

We were inspired to use porphyrins, because they are versatile, quite robust, and they have shown promising results for applications such as dye-sensitized solar cells. Improving applications based on organic dyes could for instance help in the future to face environmental problems. A first starting point for improvement is to understand and optimize the interfacial properties at the interfaces between organic molecule and the underlying substrate under very well-defined conditions, such as on single crystal surfaces under ultra-high vacuum conditions.

Our scanning tunneling microscopy study focuses on deepening the understanding of cyano-functionalized tetraphenylporphyrins on Cu(111), in particular in terms of adsorption structure, conformation and bottom-up fabrication of nanostructures. From our study, we learned that cyano-metal bonds and cyano-hydrogen interactions dictate the surface structure on Cu(111). Furthermore, cyano groups build up one-dimensional structures during annealing at 400 K, chains consisting of tetraphenylporphyrins, which are stable also at room temperature. Besides that, we have shown that the recently found inverted structure for tetraphenylporphyrin on Cu(111), which is induced by a very strong interaction between the iminic nitrogen atoms and the copper surface atoms, is also adopted for the three studied free base cyano porphyrins. Moreover, the functionalization of cyano groups in the periphery of tetraphenylporphyrins has a great impact on the self-metalation reaction of tetraphenylporphyrins.

In a next step, we transferred our knowledge of tetraphenylporphyrins on metal surfaces to oxide surfaces. Tetraphenylporphyrins were vacuum-deposited onto clean TiO_2(110) - (1 × 1) surfaces and studied as a function of coverage and temperature applying X-ray photoelectron spectroscopy. The study of tetraphenylporphyrin on TiO_2(110) - (1 × 1), when deposited at room temperature, revealed the formation of a diacid species, $4HTPP^{2+}$. In contrast to previously studied oxide surfaces, such as MgO(100), Co_3O_4(111) and CoO(111), no metalation occurs at room temperature. Annealing the sample up to 550 K leads to complete metalation of the first molecular layer.

For various applications, such as dye-sensitized solar cells, it is necessary to use anchoring groups to attach large organic molecules to substrates. Carboxylic acid has proven to be useful,

but the chemical bond is not strong enough, which is why the molecules can detach from the substrate in solution during application. Therefore, functional groups with stronger bonds while maintaining/improving electronic characteristics are required. In this field, the understanding of adsorption modes and electronic properties under well-defined conditions such as on single crystal surfaces under ultra-high vacuum conditions is also not very deep so far. For these reasons, we decided to study phenylphosphonic and benzohydroxamic acids on TiO_2(110) - (1 × 1).

Phenylphosphonic acid forms strong bonds to the surface and thereby increase the long-term stability of organic devices. Annealing series to investigate the thermal stability of phenylphosphonic acid showed that multilayers desorb at 380 K. Above this annealing temperature up to 460 K, phenylphosphonic acid binds in a monodentate binding mode, while further annealing leads to a transition of the binding mode, and in the range from 550 to 610 K a mixed-bidentate binding mode is proposed. For the monodentate and the mixed-bidentate phenylphosphonic acid on TiO_2(110) - (1 × 1), valence band and NEXAFS spectra were acquired to address the electronic structure of the molecules on TiO_2. These spectra show that the change in binding mode does not affect the electronic structure. The adsorption angles of the phenyl ring were derived from the π* transition by fitting the π* intensity as a function of five polar and two azimuthal angles and a polar angle of the phenyl ring relative to the surface normal of 25° was found.

The second interesting anchoring group that was studied is hydroxamic acid. Previous studies showed that they have similar electronic properties as carboxylic acids, but form a stronger bond to the surface, especially under basic conditions and in presence of water. We have studied benzohydroxamic acid on TiO_2(110) - (1 × 1) at room temperature as a function of coverage. For coverages below half of the molecular layer, an hydroxamate species is formed and coexists with a decomposed species, the latter presumably formed at oxygen vacancies or other surface defects. Upon deposition of a monolayer, the main species are intact hydroxamates. The N 1s X-ray photoelectron spectra showed that the hydroxamates appear as two different species with respect to the nitrogen atom. Different binding modes for hydroxamic acid have been proposed in the literature. Our photoelectron spectroscopy data, supported by density functional theory calculations, assign the low-coverage species to the monodeprotonated bidentate bridging binding mode while the species at high coverage remains elusive.

5. Zusammenfassung

In der vorliegenden Arbeit wurde mit Hilfe der Rastertunnelmikroskopie (STM), der Röntgenphotoelektronenspektroskopie (XPS) und der Nahkanten-Röntgenabsorptions-Feinstrukturspektroskopie (NEXAFS) das Adsorptionsverhalten organischer Moleküle auf Einkristalloberflächen unter Ultrahochvakuumbedingungen untersucht.

Wir haben uns entschieden Porphyrine zu untersuchen, da sie vielseitig und recht robust sind und vielversprechende Ergebnisse für Anwendungen, wie zum Beispiel in Farbstoffsolarzellen, gezeigt haben. Die Verbesserung von Anwendungen, die auf organischen Farbstoffen basieren, können in Zukunft beispielsweise helfen, Umweltprobleme zu bewältigen. Ein erster Ansatzpunkt für Verbesserungen ist das Verständnis und die Optimierung der Eigenschaften an den Grenzflächen zwischen organischen Molekülen und dem Substrat unter sehr gut definierten Bedingungen, wie auf Einkristalloberflächen unter Ultrahochvakuumbedingungen.

Unsere Rastertunnelmikroskopiestudie konzentriert sich auf die Vertiefung des Verständnisses von Cyano-funktionalisierten Tetraphenylporphyrinen auf Cu(111), insbesondere im Hinblick auf die Adsorptionsstruktur und -konformation sowie die Bottom-up-Herstellung von Nanostrukturen. Aus unserer Studie haben wir gelernt, dass Cyano-Metall-Bindungen und Cyano-Wasserstoff-Wechselwirkungen die Oberflächenstruktur auf Cu(111) bestimmen. Darüber hinaus bilden Cyanogruppen während des Heizens bei 400 K eindimensionale Strukturen, Ketten aus Tetraphenylporphyrinen, die wiederum auch bei Raumtemperatur stabil sind. Außerdem konnten wir zeigen, dass die gerade erst gefundene „invertierte“ Struktur für Tetraphenylporphyrin auf Cu(111), die durch eine sehr starke Wechselwirkung zwischen den iminischen Stickstoffatomen und den Kupferoberflächenatomen hervorgerufen wird, auch für die drei untersuchten Cyano-Porphyrine vorliegt. Darüber hinaus hat die Funktionalisierung von CN-Gruppen in der Peripherie von Tetraphenylporphyrinen einen großen Einfluss auf die Selbstmetallierungsreaktion von Tetraphenylporphyrinen.

In nächsten Schritt haben wir unser Wissen über Tetraphenylporphyrine auf Metalloberflächen auf Oxidoberflächen übertragen. Tetraphenylporphyrine wurden im Vakuum auf saubere TiO_2(110) - (1 × 1) Oberflächen abgeschieden und in Abhängigkeit der Bedeckung und der Temperatur mittels Röntgenphotoelektronenspektroskopie untersucht. Die Untersuchung von Tetraphenylporphyrin auf TiO_2(110) - (1 × 1) bei der Abscheidung bei Raumtemperatur ergab die Bildung einer zweifach-positive-geladenen Spezies, $4HTPP^{2+}$. Im Gegensatz zu früher untersuchten Oxidoberflächen, wie MgO(100), Co_3O_4(111) und CoO(111), findet bei

Raumtemperatur keine Metallierung statt. Erst das Heizen der Probe bei 550 K führt zu einer vollständigen Metallierung der ersten Molekularschicht.

Für verschiedene Anwendungen, wie z. B. Farbstoffsolarzellen, ist es nötig große organische Moleküle mit Hilfe von funktionellen Gruppen an einem Substrat zu immobilisieren. Carbonsäuregruppen haben sich als zweckmäßig erwiesen, jedoch ist die chemische Bindung nicht sehr stark, weswegen sich die Moleküle in Lösung von dem Substrat lösen können. Daher werden funktionelle Gruppen mit stärkeren Bindungen bei gleichbleibender/verbesserter elektronischer Charakteristik benötigt. In diesem Bereich ist bisher auch das Verständnis der Adsorptionsmodi und der elektronischen Eigenschaften unter wohl-definierten Bedingungen wie auf Einkristalloberflächen unter Ultrahochvakuumbedingungen nicht sehr tiefgreifend. Aus diesen Gründen haben wir uns entschieden Phenylphosphon- und Benzohydroxamsäure auf TiO_2(110) - (1 × 1) zu untersuchen.

Phenylphosphonsäure bildet starke Bindungen mit der Oberfläche und erhöht damit die Langzeitstabilität bei potenziellen Anwendungen. Heizserien von Phenylphosphonsäure zeigten, dass Multilagen bei 430 K desorbieren. Bei Temperaturen bis zu 460 K bindet Phenylphosphonsäure in einem monodentaten Bindungsmodus, während weiteres Heizen zum Übergang in einen anderen Bindungsmodus führt, und in einem gemischten einfach und zweifach deprotonierten bidentaten Bindungsmodus endet. Für beide Bindungsmodi wurden Valenzband- und NEXAFS-Spektren aufgenommen, um die elektronische Struktur der Moleküle auf TiO_2 zu untersuchen, und diese Spektren zeigen, dass der Bindungsmodus die elektronische Struktur nicht beeinflusst. Die Adsorptionswinkel des Phenylrings wurden aus dem π*-Übergang abgeleitet, indem die π*-Intensität als Funktion von fünf polaren und zwei azimutalen Winkeln angepasst wurden; für den Phenylring wurde ein polarer Winkel von 25° relativ zur Oberflächennormalen ermittelt.

Die nächste interessante Ankergruppe, die untersucht wurde, ist die Hydroxamsäuregruppe. Frühere Studien zeigten, dass sie ähnliche elektronische Eigenschaften wie die Carbonsäuregruppe besitzt und eine stärkere Bindung an die Oberfläche eingeht, insbesondere unter basischen Bedingungen und in Gegenwart von Wasser. Wir haben Benzohydroxamsäure auf TiO_2(110) - (1 × 1) bei Raumtemperatur als Funktion der Bedeckung untersucht. Bei einer Bedeckung von weniger als der Hälfte der Molekülschicht wird eine Hydroxamat-Spezies gebildet, die mit einer zersetzten Spezies koexistiert, wobei Letztere wahrscheinlich an Sauerstofffehlstellen oder anderen Oberflächendefekten gebildet wird. Bei der Abscheidung einer Monolage sind die wichtigsten Spezies intakte Hydroxamate. Die N 1s Spektren zeigen, dass die

Hydroxamate in Bezug auf das Stickstoffatom als zwei verschiedene Spezies auftreten. In der Literatur werden verschiedene Bindungsmodi für Hydroxamsäure vorgeschlagen. Unsere Photoelektronenspektroskopiedaten, unterstützt durch Berechnung basierend auf Dichtefunktionaltheorie, ordnen die Spezies mit geringer Bedeckung dem monodeprotonierten, bidentat-verbrückten Bindungsmodus zu, wobei die Spezies bei hoher Bedeckung umstritten bleibt.

6. Outlook

Further experiments on metalated and non-metalated functionalized porphyrins on metal and oxide single-crystal surfaces under ultrahigh-vacuum conditions will be performed at the Chair of Physical Chemistry II of Professor Steinrück at the University of Erlangen-Nuremberg.

The focus in the Lytken group will presumably be on TiO_2 and different other oxides that are relevant for current applications. Studying the anchoring behavior of organic molecules and the adsorption properties of porphyrins will further be an important topic. One open question is, if we really form titanyl tetraphenylporphyrin or if another metalated species is formed. One possibility would be to deposit a stronger-binding molecule on top of the self-metalated species. If the molecules are free to move between the layers, the stronger-binding molecules will displace the weaker-binding metalated porphyrin into the multilayer. It would now be possible to desorb the multilayer and thereby identify the metalated species with a mass spectrometer.

For phenylphosphonic acid on TiO_2, we have only studied the fully-covered surface. It would be interesting to also study submonolayer coverages on both fully-oxidized as well as reduced TiO_2(110) surfaces. We were not able to study submonolayer coverages on our first phenylphosphonic acid beamtime, because it was difficult to keep the sample clean. However, our benzohydroxamic acid beamtime showed that this is possibly by applications of cryopumps. One important question is whether the transformation of the monodentate to the mixed-bidentate binding mode is reversible. It would be interesting to know if exposure of the samples to air or liquid water would reverse the transition back to a monodentate binding motif. In particular, synchrotron X-ray photoelectron spectroscopy with very high resolution could help to reveal differences in binding motives for different sample preparations.

Our measurements of benzohydroxamic acid on TiO_2 opened up several follow-up questions. Scanning tunneling microscopy in combination with density functional theory calculations would help to narrow down possible answers. Scanning tunneling microscopy would help in identifying the number of different species, such as decomposed species on the surface, and their location. Knowledge on the degree of order on the surface would also be very helpful.

7. Acknowledgement

The acknowledgement is not available in the online version.

8. References

[1] B. Kräutler, *Organometallic Chemistry of B12 Coenzymes*, in: *Metal-Carbon Bonds in Enzymes and Cofactors: Metal Ions in Life Sciences* The Royal Society of Chemistry, Vienna, 2009, pp. 1-51, ISBN: 978-1-84755-915-9.

[2] R. Lemberg, *Porphyrins in Nature*, in: *Fortschritte der Chemie Organischer Naturstoffe / Progress in the Chemistry of Organic Natural Products / Progrés dans la Chimie des Substances Organiques Naturelles*, Springer, Vienna, 1954, ISBN: 978-3-7091-8014-3.

[3] P.R. Rich, A. Maréchal, *8.5 Electron Transfer Chains: Structures, Mechanisms and Energy Coupling*, in: *Comprehensive Biophysics*, Elsevier, Amsterdam, 2012, pp. 72-93, ISBN: 978-0-08-095718-0.

[4] C.C. Wamser, H.-S. Kim, J.-K. Lee, *Solar cells with porphyrin sensitization,* Optical Materials, 21 (2003), pp. 221-224, DOI: https://doi.org/10.1016/S0925-3467(02)00140-4.

[5] W.M. Campbell, K.W. Jolley, P. Wagner, K. Wagner, P.J. Walsh, K.C. Gordon, L. Schmidt-Mende, M.K. Nazeeruddin, Q. Wang, M. Grätzel, D.L. Officer, *Highly Efficient Porphyrin Sensitizers for Dye-Sensitized Solar Cells,* The Journal of Physical Chemistry C, 111 (2007), pp. 11760-11762, DOI: https://doi.org/10.1021/jp0750598.

[6] M.K. Panda, K. Ladomenou, A.G. Coutsolelos, *Porphyrins in bio-inspired transformations: Light-harvesting to solar cell,* Coordination Chemistry Reviews, 256 (2012), pp. 2601-2627, DOI: https://doi.org/10.1016/j.ccr.2012.04.041.

[7] M.G. Walter, A.B. Rudine, C.C. Wamser, *Porphyrins and phthalocyanines in solar photovoltaic cells,* Journal of Porphyrins and Phthalocyanines, 14 (2010), pp. 759-792, DOI: https://doi.org/10.1142/S1088424610002689.

[8] Z. Parsa, S.S. Naghavi, N. Safari, *Designing Push–Pull Porphyrins for Efficient Dye-Sensitized Solar Cells,* The Journal of Physical Chemistry A, 122 (2018), pp. 5870-5877, DOI: https://doi.org/10.1021/acs.jpca.8b03668.

[9] M. Urbani, M. Grätzel, M.K. Nazeeruddin, T. Torres, *Meso-Substituted Porphyrins for Dye-Sensitized Solar Cells,* Chemical Reviews, 114 (2014), pp. 12330-12396, DOI: https://doi.org/10.1021/cr5001964.

[10] R. Ma, P. Guo, H. Cui, X. Zhang, M.K. Nazeeruddin, M. Grätzel, *Substituent Effect on the Meso-Substituted Porphyrins: Theoretical Screening of Sensitizer Candidates for Dye-Sensitized Solar Cells,* The Journal of Physical Chemistry A, 113 (2009), pp. 10119-10124, DOI: https://doi.org/10.1021/jp905412y.

[11] T. Higashino, Y. Kurumisawa, A.B. Alemayehu, R.F. Einrem, D. Sahu, D. Packwood, K. Kato, A. Yamakata, A. Ghosh, H. Imahori, *Heavy Metal Effects on the Photovoltaic Properties of Metallocorroles in Dye-Sensitized Solar Cells,* ACS Applied Energy Materials, 3 (2020), pp. 12460-12467, DOI: https://doi.org/10.1021/acsaem.0c02427.

[12] J.M. Gottfried, *Surface chemistry of porphyrins and phthalocyanines,* Surface Science Reports, 70 (2015), pp. 259-379, DOI: https://doi.org/10.1016/j.surfrep.2015.04.001.

[13] H. Marbach, *Surface-Mediated in Situ Metalation of Porphyrins at the Solid-Vacuum Interface,* Accounts of Chemical Research, 48 (2015), pp. 2649-2658, DOI: https://doi.org/10.1021/acs.accounts.5b00243.

[14] W. Auwärter, A. Weber-Bargioni, S. Brink, A. Riemann, A. Schiffrin, M. Ruben, J.V. Barth, *Controlled Metalation of Self-Assembled Porphyrin Nanoarrays in Two Dimensions,* ChemPhysChem, 8 (2007), pp. 250-254, DOI: https://doi.org/10.1002/cphc.200600675.

[15] F. Buchner, V. Schwald, K. Comanici, H.-P. Steinrück, H. Marbach, *Microscopic Evidence of the Metalation of a Free-Base Porphyrin Monolayer with Iron,* ChemPhysChem, 8 (2007), pp. 241-243, DOI: https://doi.org/10.1002/cphc.200600698.

[16] K. Diller, F. Klappenberger, M. Marschall, K. Hermann, A. Nefedov, C. Wöll, J.V. Barth, *Self-metalation of 2H-tetraphenylporphyrin on Cu(111): An x-ray spectroscopy study,* The Journal of Chemical Physics, 136 (2012), pp. 014705, DOI: https://doi.org/10.1063/1.3674165.

[17] C.M. Doyle, S.A. Krasnikov, N.N. Sergeeva, A.B. Preobrajenski, N.A. Vinogradov, Y.N. Sergeeva, M.O. Senge, A.A. Cafolla, *Evidence for the formation of an intermediate complex in the direct metalation of tetra(4-bromophenyl)-porphyrin on the Cu(111) surface,* Chemical Communications, 47 (2011), pp. 12134-12136, DOI: https://doi.org/10.1039/C1CC15241F.

[18] R. González-Moreno, C. Sánchez-Sánchez, M. Trelka, R. Otero, A. Cossaro, A. Verdini, L. Floreano, M. Ruiz-Bermejo, A. García-Lekue, J.Á. Martín-Gago, C. Rogero, *Following the Metalation Process of Protoporphyrin IX with Metal Substrate Atoms at Room Temperature,* The Journal of Physical Chemistry C, 115 (2011), pp. 6849-6854, DOI: https://doi.org/10.1021/jp200533a.

[19] J.M. Gottfried, K. Flechtner, A. Kretschmann, T. Lukasczyk, H.-P. Steinrück, *Direct Synthesis of a Metalloporphyrin Complex on a Surface,* Journal of the American Chemical Society, 128 (2006), pp. 5644-5645, DOI: https://doi.org/10.1021/ja0610333.

[20] K. Diller, A.C. Papageorgiou, F. Klappenberger, F. Allegretti, J.V. Barth, W. Auwärter, *In vacuo interfacial tetrapyrrole metallation,* Chemical Society Reviews, 45 (2016), pp. 1629-1656, DOI: https://doi.org/10.1039/C5CS00207A.

[21] K. Ladomenou, T.N. Kitsopoulos, G.D. Sharma, A.G. Coutsolelos, *The importance of various anchoring groups attached on porphyrins as potential dyes for DSSC applications,* RSC Advances, 4 (2014), pp. 21379-21404, DOI: https://doi.org/10.1039/C4RA00985A.

[22] K.E. Dalle, J. Warnan, J.J. Leung, B. Reuillard, I.S. Karmel, E. Reisner, *Electro- and Solar-Driven Fuel Synthesis with First Row Transition Metal Complexes,* Chemical reviews, 119 (2019), pp. 2752–2875, DOI: https://doi.org/10.1021/acs.chemrev.8b00392.

[23] K.L. Materna, R.H. Crabtree, G.W. Brudvig, *Anchoring groups for photocatalytic water oxidation on metal oxide surfaces,* Chemical Society reviews, 46 (2017), pp. 6099–6110, DOI: https://doi.org/10.1039/c7cs00314e.

[24] L. Zhang, J.M. Cole, *Anchoring groups for dye-sensitized solar cells,* ACS Applied Materials & Interfaces, 7 (2015), pp. 3427–3455, DOI: https://doi.org/10.1021/am507334m.

[25] B. Puscher, *Charge Carrier Diffusion and Transfer Mechanism in Hybrid Lead Halide Perovskite Materials*, Chemistry and Pharmacy, University of Erlangen-Nürnberg, Erlangen, 2020.

[26] NREL, *Best Research-Cell Efficiency Chart*, National Renewable Energy Laboratory, 2021, URL: https://www.nrel.gov/pv/cell-efficiency.html, Access Date: 28 October 2021.

[27] T. Higashino, S. Nimura, K. Sugiura, Y. Kurumisawa, Y. Tsuji, H. Imahori, *Photovoltaic Properties and Long-Term Durability of Porphyrin-Sensitized Solar Cells with Silicon-Based Anchoring Groups,* ACS Omega, 2 (2017), pp. 6958-6967, DOI: https://doi.org/10.1021/acsomega.7b01290.

[28] M.I. Asghar, K. Miettunen, J. Halme, P. Vahermaa, M. Toivola, K. Aitola, P. Lund, *Review of stability for advanced dye solar cells,* Energy & Environmental Science, 3 (2010), pp. 418-426, DOI: https://doi.org/10.1039/B922801B.

[29] K. Jousten, *Handbuch Vakuumtechnik*, 12th ed., Springer Vieweg, Wiesbaden, 2018, ISBN: 978-3-658-13421-1.

[30] U. Diebold, *The surface science of titanium dioxide,* Surface Science Reports, 48 (2003), pp. 53-229, DOI: https://doi.org/10.1016/S0167-5729(02)00100-0.

[31] M.A. Henderson, *A surface science perspective on TiO_2 photocatalysis,* Surface Science Reports, 66 (2011), pp. 185-297, DOI: https://doi.org/10.1016/j.surfrep.2011.01.001.

[32] J.E. Jupille, G.E. Thornton, *Defects at Oxide Surfaces*, Springer Series in Surface Sciences, Springer, Cham, 2015, ISBN: 978-3-319-14367-5.

[33] T.L. Thompson, J.T. Yates, *Surface Science Studies of the Photoactivation of TiO_2 New Photochemical Processes,* Chemical Reviews, 106 (2006), pp. 4428-4453, DOI: https://doi.org/10.1021/cr050172k.

[34] P.M. Clawin, C.M. Friend, K. Al-Shamery, *Defects in Surface Chemistry—Reductive coupling of Benzaldehyde on Rutile TiO_2(110),* Chemistry – A European Journal, 20 (2014), pp. 7665-7669, DOI: https://doi.org/10.1002/chem.201402102.

[35] Z. Dohnálek, I. Lyubinetsky, R. Rousseau, *Thermally-driven processes on rutile TiO_2(110)-(1×1): A direct view at the atomic scale,* Progress in Surface Science, 85 (2010), pp. 161-205, DOI: https://doi.org/10.1016/j.progsurf.2010.03.001.

[36] Z. Zhang, J.T. Yates, *Defects on TiO_2--Key Pathways to Important Surface Processes*, in: *Defects at Oxide Surfaces*, Springer International Publishing, Cham, 2015, pp. 81-121, ISBN: 978-3-319-14366-8.

[37] Q. Guo, Z. Ma, C. Zhou, Z. Ren, X. Yang, *Single Molecule Photocatalysis on TiO_2 Surfaces,* Chemical Reviews, 119 (2019), pp. 11020-11041, DOI: https://doi.org/10.1021/acs.chemrev.9b00226.

[38] O. Björneholm, M.H. Hansen, A. Hodgson, L.-M. Liu, D.T. Limmer, A. Michaelides, P. Pedevilla, J. Rossmeisl, H. Shen, G. Tocci, E. Tyrode, M.-M. Walz, J. Werner, H. Bluhm, *Water at Interfaces,* Chemical Reviews, 116 (2016), pp. 7698-7726, DOI: https://doi.org/10.1021/acs.chemrev.6b00045.

[39] C. Sun, L.-M. Liu, A. Selloni, G.Q. Lu, S.C. Smith, *Titania-water interactions: a review of theoretical studies,* Journal of Materials Chemistry, 20 (2010), pp. 10319-10334, DOI: https://doi.org/10.1039/C0JM01491E.

[40] C.L. Pang, R. Lindsay, G. Thornton, *Structure of Clean and Adsorbate-Covered Single-Crystal Rutile TiO_2 Surfaces,* Chemical Reviews, 113 (2013), pp. 3887-3948, DOI: https://doi.org/10.1021/cr300409r.

[41] M.A. Henderson, *The interaction of water with solid surfaces: fundamental aspects revisited,* Surface Science Reports, 46 (2002), pp. 1-308, DOI: https://doi.org/10.1016/S0167-5729(01)00020-6.

[42] A. Naldoni, M. Altomare, G. Zoppellaro, N. Liu, Š. Kment, R. Zbořil, P. Schmuki, *Photocatalysis with Reduced TiO_2: From Black TiO_2 to Cocatalyst-Free Hydrogen Production,* ACS Catalysis, 9 (2019), pp. 345-364, DOI: https://doi.org/10.1021/acscatal.8b04068.

[43] U. Diebold, *Structure and properties of TiO_2 surfaces: a brief review,* Applied Physics A, 76 (2003), pp. 681-687, DOI: https://doi.org/10.1007/s00339-002-2004-5.

[44] R.J.D. Tilley, *Color Centers*, in: *Encyclopedia of Color Science and Technology*, Springer Berlin Heidelberg, Berlin, Heidelberg, 2019, pp. 1-8, ISBN: 978-3-642-27851-8.

[45] M. Li, W. Hebenstreit, U. Diebold, A.M. Tyryshkin, M.K. Bowman, G.G. Dunham, M.A. Henderson, *The Influence of the Bulk Reduction State on the Surface Structure and Morphology of Rutile $TiO_2(110)$ Single Crystals,* The Journal of Physical Chemistry B, 104 (2000), pp. 4944-4950, DOI: https://doi.org/10.1021/jp9943272.

[46] V.E. Henrich, G. Dresselhaus, H.J. Zeiger, *Observation of Two-Dimensional Phases Associated with Defect States on the Surface of TiO_2,* Physical Review Letters, 36 (1976), pp. 1335-1339, DOI: https://doi.org/10.1103/PhysRevLett.36.1335.

[47] M. Setvín, M. Wagner, M. Schmid, G.S. Parkinson, U. Diebold, *Surface point defects on bulk oxides: atomically-resolved scanning probe microscopy,* Chemical Society Reviews, 46 (2017), pp. 1772-1784, DOI: https://doi.org/10.1039/C7CS00076F.

[48] X. Mao, X. Lang, Z. Wang, Q. Hao, B. Wen, Z. Ren, D. Dai, C. Zhou, L.-M. Liu, X. Yang, *Band-Gap States of TiO_2(110): Major Contribution from Surface Defects,* The Journal of Physical Chemistry Letters, 4 (2013), pp. 3839-3844, DOI: https://doi.org/10.1021/jz402053p.

[49] Z.-T. Wang, J.C. Garcia, N.A. Deskins, I. Lyubinetsky, *Ability of TiO_2 surface to be fully hydroxylated and fully reduced,* Physical Review B, 92 (2015), pp. 081402, DOI: https://doi.org/10.1103/PhysRevB.92.081402.

[50] P.G. Moses, A. Janotti, C. Franchini, G. Kresse, C.G. Van de Walle, *Donor defects and small polarons on the TiO_2(110) surface,* Journal of Applied Physics, 119 (2016), pp. 181503, DOI: https://doi.org/10.1063/1.4948239.

[51] D. Briggs, J.T. Grant, *Surface Analysis by Auger and X-ray Photoelectron Spectroscopy*, IMP Publications LLP and Surface Spectra Limited UK, 2003, ISBN: 1901019047.

[52] ISO, *ISO18115-1: Surface chemical analysis — Vocabulary: Part 1: General terms and terms used in spectroscopy*, International Organization for Standardization, Geneva, 2013, URL: https://www.iso.org/obp/ui/#iso:std:iso:18115:-1:ed-2:v1:en, Access Date: 28 October 2021.

[53] M.P. Seah, W.A. Dench, *Quantitative electron spectroscopy of surfaces: A standard data base for electron inelastic mean free paths in solids,* Surface and Interface Analysis, 1 (1979), pp. 2-11, DOI: https://doi.org/10.1002/sia.740010103.

[54] A. Jablonski, C.J. Powell, *The electron attenuation length revisited,* Surface Science Reports, 47 (2002), pp. 33-91, DOI: https://doi.org/10.1016/S0167-5729(02)00031-6.

[55] J.F. Watts, J. Wolstenholme, *Electron Spectroscopy*, An Introduction to Surface Analysis by XPS and AES, 2019, pp. 1-18.

[56] J.F. Watts, J. Wolstenholme, *An Introduction to Surface Analysis by XPS and AES*, John Wiley & Sons Ltd., 2019, ISBN: 978-1-1194-1765-1.

[57] R. Jenkins, *Quantitative X-Ray Spectrometry*, 2th ed., Chapman and Hall/CRC, Boca Raton, 1995, ISBN: 978-0-8247-9554-2.

[58] M.D. Röckert, *Spectroscopic Insights in the Metalation and Dehydrogenation of Tetrapyrroles on Well-Defined Metal Substrates*, Chemistry and Pharmacy, University of Erlangen-Nürnberg, Erlangen, 2015.

[59] M. Franke, *Porphyrin Reactions on Oxide Surfaces and in the Liquid Phase & Anhydride Formation on a Silver Surface*, Chemistry and Pharmacy, University of Erlangen-Nürnberg, Erlangen, 2017.

[60] C.J. Powell, *Practical guide for inelastic mean free paths, effective attenuation lengths, mean escape depths, and information depths in x-ray photoelectron spectroscopy,* Journal of Vacuum Science & Technology A, 38 (2020), pp. 023209, DOI: https://doi.org/10.1116/1.5141079.

[61] A. Jablonski, C.J. Powell, *Practical expressions for the mean escape depth, the information depth, and the effective attenuation length in Auger-electron spectroscopy and x-ray photoelectron spectroscopy,* Journal of Vacuum Science & Technology A, 27 (2009), pp. 253-261, DOI: https://doi.org/10.1116/1.3071947.

[62] H. Shinotsuka, B. Da, S. Tanuma, H. Yoshikawa, C.J. Powell, D.R. Penn, *Calculations of electron inelastic mean free paths. XI. Data for liquid water for energies from 50 eV to 30 keV,* Surface and Interface Analysis, 49 (2017), pp. 238-252, DOI: https://doi.org/10.1002/sia.6123.

[63] S. Tanuma, H. Shinotsuka, C.J. Powell, D.R. Penn, *Electron inelastic mean free paths in compounds,* Journal of Surface Analysis, 26 (2019), pp. 106-107, DOI: https://doi.org/10.1384/jsa.26.106.

[64] D. Wechsler, C.C. Fernández, H.-P. Steinrück, O. Lytken, F.J. Williams, *Covalent Anchoring and Interfacial Reactions of Adsorbed Porphyrins on Rutile TiO_2(110),* The Journal of Physical Chemistry C, 122 (2018), pp. 4480-4487, DOI: https://doi.org/10.1021/acs.jpcc.7b12717.

[65] F. Buchner, K. Flechtner, Y. Bai, E. Zillner, I. Kellner, H.-P. Steinrück, H. Marbach, J.M. Gottfried, *Coordination of Iron Atoms by Tetraphenylporphyrin Monolayers and Multilayers on Ag(111) and Formation of Iron-Tetraphenylporphyrin,* The Journal of Physical Chemistry C, 112 (2008), pp. 15458-15465, DOI: https://doi.org/10.1021/jp8052955.

[66] T. Lukasczyk, K. Flechtner, L.R. Merte, N. Jux, F. Maier, J.M. Gottfried, H.-P. Steinrück, *Interaction of Cobalt(II) Tetraarylporphyrins with a Ag(111) Surface Studied with Photoelectron Spectroscopy,* The Journal of Physical Chemistry C, 111 (2007), pp. 3090-3098, DOI: https://doi.org/10.1021/jp0652345.

[67] W. Auwärter, K. Seufert, F. Klappenberger, J. Reichert, A. Weber-Bargioni, A. Verdini, D. Cvetko, M. Dell'Angela, L. Floreano, A. Cossaro, G. Bavdek, A. Morgante, A.P. Seitsonen, J.V. Barth, *Site-specific electronic and geometric interface structure of Co-tetraphenyl-porphyrin layers on Ag(111),* Physical Review B, 81 (2010), pp. 245403, DOI: https://doi.org/10.1103/PhysRevB.81.245403.

[68] M. Röckert, S. Ditze, M. Stark, J. Xiao, H.-P. Steinrück, H. Marbach, O. Lytken, *Abrupt Coverage-Induced Enhancement of the Self-Metalation of Tetraphenylporphyrin with Cu(111),* The Journal of Physical Chemistry C, 118 (2014), pp. 1661-1667, DOI: https://doi.org/10.1021/jp412121b.

[69] R.D. Young, *Surface microtopography,* Physics Today 24 (1971), pp. 42-49, DOI: https://doi.org/10.1063/1.3022432.

[70] R. Young, J. Ward, F. Scire, *The Topografiner: An Instrument for Measuring Surface Microtopography,* Review of Scientific Instruments, 43 (1972), pp. 999-1011, DOI: https://doi.org/10.1063/1.1685846.

[71] H.-J. Güntherodt, R. Wiesendanger, *Scanning Tunneling Microscopy I, General Principles and Applications to Clean and Absorbate-Covered Surfaces*, Springer-Verlag Berlin Heidelberg, 1994, ISBN: 978-3-642-79255-7.

[72] G. Binnig, H. Rohrer, C. Gerber, E. Weibel, *Surface Studies by Scanning Tunneling Microscopy,* Physical Review Letters, 49 (1982), pp. 57-61, DOI: https://doi.org/10.1103/PhysRevLett.49.57.

[73] G. Binnig, H. Rohrer, C. Gerber, E. Weibel, *7x7 Reconstruction on Si(111) Resolved in Real Space,* Physical Review Letters, 50 (1983), pp. 120-123, DOI: https://doi.org/10.1103/PhysRevLett.50.120.

[74] L. Zhang, M. Lepper, M. Stark, D. Lungerich, N. Jux, W. Hieringer, H.-P. Steinrück, H. Marbach, *Self-assembly and coverage dependent thermally induced conformational changes of Ni(II)-meso-tetrakis (4-tert-butylphenyl) benzoporphyrin on Cu(111),* Physical Chemistry Chemical Physics, 17 (2015), pp. 13066-13073, DOI: https://doi.org/10.1039/C5CP01490E.

[75] U. Diebold, J.F. Anderson, K.-O. Ng, D. Vanderbilt, *Evidence for the Tunneling Site on Transition-Metal Oxides: TiO_2(110),* Physical Review Letters, 77 (1996), pp. 1322-1325, DOI: https://doi.org/10.1103/PhysRevLett.77.1322.

[76] S. Wendt, R. Schaub, J. Matthiesen, E.K. Vestergaard, E. Wahlström, M.D. Rasmussen, P. Thostrup, L.M. Molina, E. Lægsgaard, I. Stensgaard, B. Hammer, F. Besenbacher, *Oxygen vacancies on TiO_2(110) and their interaction with H_2O and O_2: A combined high-resolution STM and DFT study,* Surface Science, 598 (2005), pp. 226-245, DOI: https://doi.org/10.1016/j.susc.2005.08.041.

[77] O. Dulub, W. Hebenstreit, U. Diebold, *Imaging Cluster Surfaces with Atomic Resolution: The Strong Metal-Support Interaction State of Pt Supported on TiO_2(110),* Physical Review Letters, 84 (2000), pp. 3646-3649, DOI: https://doi.org/10.1103/PhysRevLett.84.3646.

[78] L. Gross, N. Moll, F. Mohn, A. Curioni, G. Meyer, F. Hanke, M. Persson, *High-Resolution Molecular Orbital Imaging Using a p-Wave STM Tip,* Physical Review Letters, 107 (2011), pp. 086101, DOI: https://doi.org/10.1103/PhysRevLett.107.086101.

[79] P. Jelínek, *High resolution SPM imaging of organic molecules with functionalized tips,* Journal of Physics: Condensed Matter, 29 (2017), pp. 343002, DOI: https://doi.org/10.1088/1361-648x/aa76c7.

[80] I. Swart, T. Sonnleitner, J. Niedenführ, J. Repp, *Controlled Lateral Manipulation of Molecules on Insulating Films by STM,* Nano Letters, 12 (2012), pp. 1070-1074, DOI: https://doi.org/10.1021/nl204322r.

[81] G.J. Simpson, V. García-López, A. Daniel Boese, J.M. Tour, L. Grill, *How to control single-molecule rotation,* Nature Communications, 10 (2019), pp. 4631, DOI: https://doi.org/10.1038/s41467-019-12605-8.

[82] D. Fujita, *Scanning Tunneling Microscopy and Spectroscopy for Nanofunctionality Characterization*, in: *Nanomaterial Characterization*, 2016, pp. 231-252, ISBN: 9781118753460.

[83] J. Tersoff, D.R. Hamann, *Theory of the scanning tunneling microscope,* Physical Review B, 31 (1985), pp. 805-813, DOI: https://doi.org/10.1103/PhysRevB.31.805.

[84] W.A. Hofer, A.S. Foster, A.L. Shluger, *Theories of scanning probe microscopes at the atomic scale,* Reviews of Modern Physics, 75 (2003), pp. 1287-1331, DOI: https://doi.org/10.1103/RevModPhys.75.1287.

[85] N.J. DiNardo, *Introduction*, in: *Nanoscale Characterization of Surfaces and Interfaces*, 1994, pp. 6-12, ISBN: 9783527615957.

[86] N.J. DiNardo, *Scanning Tunneling Microscopy (STM)*, in: *Nanoscale Characterization of Surfaces and Interfaces*, 1994, pp. 12-118, ISBN: 9783527615957.

[87] V.V. Tsukruk, S. Singamaneni, *Scanning Probe Microscopy of Soft Matter*, Wiley‐VCH Verlag GmbH & Co. KGaA, 2012, ISBN: 9783527327430 (Print). 9783527639953(Online).

[88] G. Teobaldi, H. Lin, W. Hofer, *Theory of Scanning Tunneling Microscopy and Applications in Catalysis*, in: *Scanning Tunneling Microscopy in Surface Science*, 2009, pp. 97-118, ISBN: 9783527628827.

[89] R. Tantra, *Nanomaterial characterization: An introduction*, John Wiley & Sons Inc, Hoboken, 2016, ISBN: 978-1-118-75393-4.

[90] F. Buchner, K.-G. Warnick, T. Wölfle, A. Görling, H.-P. Steinrück, W. Hieringer, H. Marbach, *Chemical Fingerprints of Large Organic Molecules in Scanning Tunneling Microscopy: Imaging Adsorbate−Substrate Coupling of Metalloporphyrins,* The Journal of Physical Chemistry C, 113 (2009), pp. 16450-16457, DOI: https://doi.org/10.1021/jp904680c.

[91] D. Tománek, S.G. Louie, H.J. Mamin, D.W. Abraham, R.E. Thomson, E. Ganz, J. Clarke, *Theory and observation of highly asymmetric atomic structure in scanning-tunneling-microscopy images of graphite,* Physical Review B, 35 (1987), pp. 7790-7793, DOI: https://doi.org/10.1103/PhysRevB.35.7790.

[92] L. Gragnaniello, S. Agnoli, G. Parteder, A. Barolo, F. Bondino, F. Allegretti, S. Surnev, G. Granozzi, F.P. Netzer, *Cobalt oxide nanolayers on Pd(100): The thickness-dependent structural evolution,* Surface Science, 604 (2010), pp. 2002-2011, DOI: https://doi.org/10.1016/j.susc.2010.08.012.

[93] C.J. Chen, *Introduction to Scanning Tunneling Microscopy*, Oxford University Press, 2007, ISBN: 9780199211500.

[94] R. Young, J. Ward, F. Scire, *Observation of Metal-Vacuum-Metal Tunneling, Field Emission, and the Transition Region,* Physical Review Letters, 27 (1971), pp. 922-924, DOI: https://doi.org/10.1103/PhysRevLett.27.922.

[95] I. Horcas, R. Fernández, J.M. Gómez-Rodríguez, J. Colchero, J. Gómez-Herrero, A.M. Baro, *WSXM: A software for scanning probe microscopy and a tool for nanotechnology,* Review of Scientific Instruments, 78 (2007), pp. 013705, DOI: https://doi.org/10.1063/1.2432410.

[96] A. Bianconi, *Surface X-ray absorption spectroscopy: Surface EXAFS and surface XANES,* Applications of Surface Science, 6 (1980), pp. 392-418, DOI: https://doi.org/10.1016/0378-5963(80)90024-0.

[97] J. Rivnay, S.C.B. Mannsfeld, C.E. Miller, A. Salleo, M.F. Toney, *Quantitative Determination of Organic Semiconductor Microstructure from the Molecular to Device Scale,* Chemical Reviews, 112 (2012), pp. 5488-5519, DOI: https://doi.org/10.1021/cr3001109.

[98] J. Stöhr, *NEXAFS Spectroscopy*, Springer, Berlin, Heidelberg, 1992, ISBN: 978-3-662-02853-7.

[99] O. Dhez, H. Ade, S.G. Urquhart, *Calibrated NEXAFS spectra of some common polymers,* Journal of Electron Spectroscopy and Related Phenomena, 128 (2003), pp. 85-96, DOI: https://doi.org/10.1016/S0368-2048(02)00237-2.

[100] S.G. Urquhart, H. Ade, *Trends in the Carbonyl Core (C 1s, O 1s) → π* C=O Transition in the Near-Edge X-ray Absorption Fine Structure Spectra of Organic Molecules,* The Journal of Physical Chemistry B, 106 (2002), pp. 8531-8538, DOI: https://doi.org/10.1021/jp0255379.

[101] B. Watts, L. Thomsen, P.C. Dastoor, *Methods in carbon K-edge NEXAFS: Experiment and analysis,* Journal of Electron Spectroscopy and Related Phenomena, 151 (2006), pp. 105-120, DOI: https://doi.org/10.1016/j.elspec.2005.11.006.

[102] T.P. Brennan, J.T. Tanskanen, J.R. Bakke, W.H. Nguyen, D. Nordlund, M.F. Toney, M.D. McGehee, A. Sellinger, S.F. Bent, *Dynamical Orientation of Large Molecules on Oxide Surfaces and its Implications for Dye-Sensitized Solar Cells,* Chemistry of Materials, 25 (2013), pp. 4354-4363, DOI: https://doi.org/10.1021/cm402609k.

[103] B. Watts, S. Swaraj, D. Nordlund, J. Lüning, H. Ade, *Calibrated NEXAFS spectra of common conjugated polymers,* The Journal of Chemical Physics, 134 (2011), pp. 024702, DOI: 10.1063/1.3506636.

[104] P.L. Cook, X. Liu, W. Yang, F.J. Himpsel, *X-ray absorption spectroscopy of biomimetic dye molecules for solar cells,* The Journal of Chemical Physics, 131 (2009), pp. 194701, DOI: 10.1063/1.3257621.

[105] A. Schöll, Y. Zou, T. Schmidt, R. Fink, E. Umbach, *Energy calibration and intensity normalization in high-resolution NEXAFS spectroscopy,* Journal of Electron Spectroscopy and Related Phenomena, 129 (2003), pp. 1-8, DOI: https://doi.org/10.1016/S0368-2048(03)00016-1.

[106] M.M. Nahid, E. Gann, L. Thomsen, C.R. McNeill, *NEXAFS spectroscopy of conjugated polymers,* European Polymer Journal, 81 (2016), pp. 532-554, DOI: https://doi.org/10.1016/j.eurpolymj.2016.01.017.

[107] O. Lytken, D. Wechsler, H.-P. Steinrück, *Removing photoemission features from Auger-yield NEXAFS spectra,* Journal of Electron Spectroscopy and Related Phenomena, 218 (2017), pp. 35-39, DOI: https://doi.org/10.1016/j.elspec.2017.05.012.

[108] F. Buchner, J. Xiao, E. Zillner, M. Chen, M. Röckert, S. Ditze, M. Stark, H.-P. Steinrück, J.M. Gottfried, H. Marbach, *Diffusion, Rotation, and Surface Chemical Bond of Individual 2H-Tetraphenylporphyrin Molecules on Cu(111),* The Journal of Physical Chemistry C, 115 (2011), pp. 24172-24177, DOI: https://doi.org/10.1021/jp206675u.

[109] F. Buchner, E. Zillner, M. Röckert, S. Gläßel, H.-P. Steinrück, H. Marbach, *Substrate-Mediated Phase Separation of Two Porphyrin Derivatives on Cu(111),* Chemistry – A European Journal, 17 (2011), pp. 10226-10229, DOI: https://doi.org/10.1002/chem.201100462.

[110] S. Ditze, M. Röckert, F. Buchner, E. Zillner, M. Stark, H.-P. Steinrück, H. Marbach, *Towards the engineering of molecular nanostructures: local anchoring and functionalization of porphyrins on model-templates,* Nanotechnology, 24 (2013), pp. 115305, DOI: https://doi.org/10.1088/0957-4484/24/11/115305.

[111] M. Röckert, M. Franke, Q. Tariq, S. Ditze, M. Stark, P. Uffinger, D. Wechsler, U. Singh, J. Xiao, H. Marbach, H.-P. Steinrück, O. Lytken, *Coverage- and Temperature-Dependent Metalation and Dehydrogenation of Tetraphenylporphyrin on Cu(111),* Chemistry – A European Journal, 20 (2014), pp. 8948-8953, DOI: https://doi.org/10.1002/chem.201402420.

[112] M. Röckert, M. Franke, Q. Tariq, D. Lungerich, N. Jux, M. Stark, A. Kaftan, S. Ditze, H. Marbach, M. Laurin, J. Libuda, H.-P. Steinrück, O. Lytken, *Insights in Reaction Mechanistics: Isotopic Exchange during the Metalation of Deuterated Tetraphenyl-21,23D-porphyrin on Cu(111),* The Journal of Physical Chemistry C, 118 (2014), pp. 26729-26736, DOI: https://doi.org/10.1021/jp507303h.

[113] J. Xiao, S. Ditze, M. Chen, F. Buchner, M. Stark, M. Drost, H.-P. Steinrück, J.M. Gottfried, H. Marbach, *Temperature-Dependent Chemical and Structural Transformations from 2H-tetraphenylporphyrin to Copper(II)-Tetraphenylporphyrin on Cu(111),* The Journal of Physical Chemistry C, 116 (2012), pp. 12275-12282, DOI: https://doi.org/10.1021/jp301757h.

[114] M. Pivetta, G.E. Pacchioni, E. Fernandes, H. Brune, *Temperature-dependent self-assembly of NC–Ph5–CN molecules on Cu(111),* The Journal of Chemical Physics, 142 (2015), pp. 101928, DOI: https://doi.org/10.1063/1.4909518.

[115] L.-A. Fendt, M. Stöhr, N. Wintjes, M. Enache, T.A. Jung, F. Diederich, *Modification of Supramolecular Binding Motifs Induced By Substrate Registry: Formation of Self-Assembled Macrocycles and Chain-Like Patterns,* Chemistry – A European Journal, 15 (2009), pp. 11139-11150, DOI: https://doi.org/10.1002/chem.200901502.

[116] F. Bischoff, Y. He, K. Seufert, D. Stassen, D. Bonifazi, J.V. Barth, W. Auwärter, *Tailoring Large Pores of Porphyrin Networks on Ag(111) by Metal–Organic Coordination,* Chemistry – A European Journal, 22 (2016), pp. 15298-15306, DOI: https://doi.org/10.1002/chem.201602154.

[117] R. Decker, U. Schlickum, F. Klappenberger, G. Zoppellaro, S. Klyatskaya, M. Ruben, J.V. Barth, H. Brune, *Using metal-organic templates to steer the growth of Fe and Co nanoclusters,* Applied Physics Letters, 93 (2008), pp. 243102, DOI: https://doi.org/10.1063/1.3040328.

[118] U. Schlickum, R. Decker, F. Klappenberger, G. Zoppellaro, S. Klyatskaya, M. Ruben, I. Silanes, A. Arnau, K. Kern, H. Brune, J.V. Barth, *Metal−Organic Honeycomb Nanomeshes with Tunable Cavity Size,* Nano Letters, 7 (2007), pp. 3813-3817, DOI: https://doi.org/10.1021/nl072466m.

[119] M. Lepper, T. Schmitt, M. Gurrath, M. Raschmann, L. Zhang, M. Stark, H. Hölzel, N. Jux, B. Meyer, M.A. Schneider, H.-P. Steinrück, H. Marbach, *Adsorption Behavior of a Cyano-Functionalized Porphyrin on Cu(111) and Ag(111): From Molecular Wires to Ordered Supramolecular Two-Dimensional Aggregates,* The Journal of Physical Chemistry C, 121 (2017), pp. 26361-26371, DOI: https://doi.org/10.1021/acs.jpcc.7b08382.

[120] J.C. Moreno-López, D.J. Mowbray, A. Pérez Paz, R.C. de Campos Ferreira, A. Ceccatto dos Santos, P. Ayala, A. de Siervo, *Roles of Precursor Conformation and Adatoms in Ullmann Coupling: An Inverted Porphyrin on Cu(111),* Chemistry of Materials, 31 (2019), pp. 3009-3017, DOI: https://doi.org/10.1021/acs.chemmater.9b00668.

[121] S. Ditze, M. Stark, M. Drost, F. Buchner, H.-P. Steinrück, H. Marbach, *Activation Energy for the Self-Metalation Reaction of 2H-Tetraphenylporphyrin on Cu(111),* Angewandte Chemie International Edition, 51 (2012), pp. 10898-10901, DOI: https://doi.org/10.1002/anie.201205464.

[122] S. Ditze, *On the dynamics of molecular processes: STM investigations of porphyrins on Cu(111)*, Department Chemistry and Pharmacy, University of Erlangen-Nuremberg, Erlangen, 2014.

[123] M. Lepper, J. Köbl, T. Schmitt, M. Gurrath, A. de Siervo, M.A. Schneider, H.-P. Steinrück, B. Meyer, H. Marbach, W. Hieringer, *"Inverted" porphyrins: a distorted adsorption geometry of free-base porphyrins on Cu(111),* Chemical Communications, 53 (2017), pp. 8207-8210, DOI: https://doi.org/10.1039/C7CC04182A.

[124] F. Albrecht, F. Bischoff, W. Auwärter, J.V. Barth, J. Repp, *Direct Identification and Determination of Conformational Response in Adsorbed Individual Nonplanar Molecular Species Using Noncontact Atomic Force Microscopy,* Nano Letters, 16 (2016), pp. 7703-7709, DOI: https://doi.org/10.1021/acs.nanolett.6b03769.

[125] R. Adhikari, G. Siglreithmaier, M. Gurrath, M. Meusel, J. Kuliga, M. Lepper, H. Hölzel, N. Jux, B. Meyer, H.-P. Steinrück, H. Marbach, *Formation of Highly Ordered Molecular Porous 2D Networks from Cyano-Functionalized Porphyrins on Cu(111),* Chemistry, 26 (2020), pp. 13408-13418, DOI: https://doi.org/10.1002/chem.202001980.

[126] R. Adhikari, J. Kuliga, M. Ruppel, N. Jux, H. Marbach, H.-P. Steinrück, *Self-Assembled 2D-Coordination Kagome, Quadratic, and Close-Packed Hexagonal Lattices Formed from a Cyano-Functionalized Benzoporphyrin on Cu(111),* The Journal of Physical Chemistry C, 125 (2021), pp. 7204-7212, DOI: 10.1021/acs.jpcc.1c00746.

[127] A. Ceccatto dos Santos, R.C. de Campos Ferreira, J.C. Moreno-López, L. Barreto, M. Lepper, R. Landers, H.-P. Steinrück, H. Marbach, A. de Siervo, *Cyano-Functionalized Porphyrins on Cu(111) from One-Dimensional Wires to Two-Dimensional Molecular Frameworks: On the Role of Co-Deposited Metal Atoms,* Chemistry of Materials, 32 (2020), pp. 2114-2122, DOI: https://doi.org/10.1021/acs.chemmater.9b05256.

[128] J. Kuliga, R.C. de Campos Ferreirra, R. Adhikari, S. Massicot, M. Lepper, H. Hölzel, N. Jux, H. Marbach, A. de Siervo, H.-P. Steinrück, *Metalation of 2HTCNPP on Ag(111) with Zn: Evidence for the Sitting atop Complex at Room Temperature,* Chemphyschem : a European journal of chemical physics and physical chemistry, 22 (2021), pp. 396-403, DOI: https://doi.org/10.1002/cphc.202000883.

[129] J. Schneider, M. Franke, M. Gurrath, M. Röckert, T. Berger, J. Bernardi, B. Meyer, H.-P. Steinrück, O. Lytken, O. Diwald, *Porphyrin Metalation at MgO Surfaces: A Spectroscopic and Quantum Mechanical Study on Complementary Model Systems,* Chemistry – A European Journal, 22 (2016), pp. 1744-1749, DOI: https://doi.org/10.1002/chem.201503661.

[130] G. Di Filippo, A. Classen, R. Pöschel, T. Fauster, *Interaction of free-base tetraphenylporphyrin with magnesium oxide: Influence of MgO morphology on metalation,* The Journal of Chemical Physics, 146 (2017), pp. 064702, DOI: https://doi.org/10.1063/1.4975229.

[131] D. Wechsler, C.C. Fernández, Q. Tariq, N. Tsud, K.C. Prince, F.J. Williams, H.-P. Steinrück, O. Lytken, *Interfacial Reactions of Tetraphenylporphyrin with Cobalt-Oxide Thin Films,* Chemistry – A European Journal, 25 (2019), pp. 13197-13201, DOI: https://doi.org/10.1002/chem.201902680.

[132] D.A. Duncan, P.S. Deimel, A. Wiengarten, M. Paszkiewicz, P. Casado Aguilar, R.G. Acres, F. Klappenberger, W. Auwärter, A.P. Seitsonen, J.V. Barth, F. Allegretti, *Bottom-Up Fabrication of a Metal-Supported Oxo–Metal Porphyrin,* The Journal of Physical Chemistry C, 123 (2019), pp. 31011-31025, DOI: https://doi.org/10.1021/acs.jpcc.9b08661.

[133] H. Nagatani, H. Watarai, *Two-Phase Stopped-Flow Measurement of the Protonation of Tetraphenylporphyrin at the Liquid−Liquid Interface,* Analytical Chemistry, 68 (1996), pp. 1250-1253, DOI: https://doi.org/10.1021/ac9506342.

[134] G. Lovat, D. Forrer, M. Abadia, M. Dominguez, M. Casarin, C. Rogero, A. Vittadini, L. Floreano, *Hydrogen capture by porphyrins at the TiO_2(110) surface,* Physical Chemistry Chemical Physics, 17 (2015), pp. 30119-30124, DOI: https://doi.org/10.1039/C5CP05437K.

[135] L.G. Teugels, L.G. Avila-Bront, S.J. Sibener, *Chiral Domains Achieved by Surface Adsorption of Achiral Nickel Tetraphenyl- or Octaethylporphyrin on Smooth and Locally Kinked Au(111),* The Journal of Physical Chemistry C, 115 (2011), pp. 2826-2834, DOI: https://doi.org/10.1021/jp1108398.

[136] A. Weber-Bargioni, W. Auwärter, F. Klappenberger, J. Reichert, S. Lefrançois, T. Strunskus, C. Wöll, A. Schiffrin, Y. Pennec, J.V. Barth, *Visualizing the Frontier Orbitals of*

a Conformationally Adapted Metalloporphyrin, ChemPhysChem, 9 (2008), pp. 89-94, DOI: https://doi.org/10.1002/cphc.200700600.

[137] C. Lun Pang, R. Lindsay, G. Thornton, *Chemical reactions on rutile TiO_2(110),* Chemical Society Reviews, 37 (2008), pp. 2328-2353, DOI: https://doi.org/10.1039/B719085A.

[138] G. Lovat, D. Forrer, M. Abadia, M. Dominguez, M. Casarin, C. Rogero, A. Vittadini, L. Floreano, *On-Surface Synthesis of a Pure and Long-Range-Ordered Titanium(IV)-Porphyrin Contact Layer on Titanium Dioxide,* The Journal of Physical Chemistry C, 121 (2017), pp. 13738-13746, DOI: https://doi.org/10.1021/acs.jpcc.7b03157.

[139] G. Lovat, D. Forrer, M. Abadia, M. Dominguez, M. Casarin, C. Rogero, A. Vittadini, L. Floreano, *Very high temperature tiling of tetraphenylporphyrin on rutile TiO_2(110),* Nanoscale, 9 (2017), pp. 11694-11704, DOI: https://doi.org/10.1039/C7NR04093H.

[140] R. Boissezon, J. Muller, V. Beaugeard, S. Monge, J.-J. Robin, *Organophosphonates as anchoring agents onto metal oxide-based materials: synthesis and applications,* RSC Advances, 4 (2014), pp. 35690-35707, DOI: https://doi.org/10.1039/C4RA05414H.

[141] J. Keth, T. Johann, H. Frey, *Hydroxamic Acid: An Underrated Moiety? Marrying Bioinorganic Chemistry and Polymer Science,* Biomacromolecules, 21 (2020), pp. 2546–2556, DOI: https://doi.org/10.1021/acs.biomac.0c00449.

[142] C. Koenigsmann, T.S. Ripolles, B.J. Brennan, C.F.A. Negre, M. Koepf, A.C. Durrell, R.L. Milot, J.A. Torre, R.H. Crabtree, V.S. Batista, G.W. Brudvig, J. Bisquert, C.A. Schmuttenmaer, *Substitution of a hydroxamic acid anchor into the MK-2 dye for enhanced photovoltaic performance and water stability in a DSSC,* Physical chemistry chemical physics 16 (2014), pp. 16629–16641, DOI: https://doi.org/10.1039/c4cp02405b.

[143] W.R. McNamara, R.L. Milot, H.-e. Song, R.C. Snoeberger III, V.S. Batista, C.A. Schmuttenmaer, G.W. Brudvig, R.H. Crabtree, *Water-stable, hydroxamate anchors for functionalization of TiO_2 surfaces with ultrafast interfacial electron transfer,* Energy & Environmental Science, 3 (2010), pp. 917, DOI: https://doi.org/10.1039/c001065k.

[144] W.R. McNamara, R.C. Snoeberger III, G. Li, C. Richter, L.J. Allen, R.L. Milot, C.A. Schmuttenmaer, R.H. Crabtree, G.W. Brudvig, V.S. Batista, *Hydroxamate anchors for water-stable attachment to TiO_2 nanoparticles,* Energy & Environmental Science, 2 (2009), pp. 1173, DOI: https://doi.org/10.1039/b910241h.

[145] C.C. Fernández, D. Wechsler, T.C.R. Rocha, H.-P. Steinrück, O. Lytken, F.J. Williams, *Adsorption of Phosphonic-Acid-Functionalized Porphyrin Molecules on TiO_2(110),* The Journal of Physical Chemistry C, 123 (2019), pp. 10974-10980, DOI: https://doi.org/10.1021/acs.jpcc.9b01019.

[146] E.S. Gawalt, G. Lu, S.L. Bernasek, J. Schwartz, *Enhanced Bonding of Alkanephosphonic Acids to Oxidized Titanium Using Surface-Bound Alkoxyzirconium Complex Interfaces,* Langmuir, 15 (1999), pp. 8929-8933, DOI: https://doi.org/10.1021/la990906m.

[147] M. Gnauck, E. Jaehne, T. Blaettler, S. Tosatti, M. Textor, H.-J.P. Adler, *Carboxy-Terminated Oligo(ethylene glycol)−Alkane Phosphate: Synthesis and Self-Assembly on Titanium Oxide Surfaces,* Langmuir, 23 (2007), pp. 377-381, DOI: https://doi.org/10.1021/la0606648.

[148] N. Tsud, M. Yoshitake, *Vacuum vapour deposition of phenylphosphonic acid on amorphous alumina,* Surface Science, 601 (2007), pp. 3060-3066, DOI: https://doi.org/10.1016/j.susc.2007.05.007.

[149] N. Adden, L.J. Gamble, D.G. Castner, A. Hoffmann, G. Gross, H. Menzel, *Phosphonic Acid Monolayers for Binding of Bioactive Molecules to Titanium Surfaces,* Langmuir, 22 (2006), pp. 8197-8204, DOI: https://doi.org/10.1021/la060754c.

[150] S. Tosatti, R. Michel, M. Textor, N.D. Spencer, *Self-Assembled Monolayers of Dodecyl and Hydroxy-dodecyl Phosphates on Both Smooth and Rough Titanium and Titanium Oxide Surfaces,* Langmuir, 18 (2002), pp. 3537-3548, DOI: https://doi.org/10.1021/la011459p.

[151] M. Wagstaffe, A.G. Thomas, M.J. Jackman, M. Torres-Molina, K.L. Syres, K. Handrup, *An Experimental Investigation of the Adsorption of a Phosphonic Acid on the Anatase TiO_2(101) Surface,* The Journal of Physical Chemistry C, 120 (2016), pp. 1693-1700, DOI: https://doi.org/10.1021/acs.jpcc.5b11258.

[152] Y. Du, N.G. Petrik, N.A. Deskins, Z. Wang, M.A. Henderson, G.A. Kimmel, I. Lyubinetsky, *Hydrogen reactivity on highly-hydroxylated TiO_2(110) surfaces prepared via carboxylic acid adsorption and photolysis,* Physical Chemistry Chemical Physics, 14 (2012), pp. 3066-3074, DOI: https://doi.org/10.1039/C1CP22515D

[153] M.B. Hugenschmidt, L. Gamble, C.T. Campbell, *The interaction of H_2O with a TiO_2(110) surface,* Surface Science, 302 (1994), pp. 329-340, DOI: https://doi.org/10.1016/0039-6028(94)90837-0.

[154] J.M. White, J. Szanyi, M.A. Henderson, *The Photon-Driven Hydrophilicity of Titania: A Model Study Using TiO_2(110) and Adsorbed Trimethyl Acetate,* The Journal of Physical Chemistry B, 107 (2003), pp. 9029-9033, DOI: https://doi.org/10.1021/jp0345046.

[155] C.L. Pang, M. Watkins, G. Cabailh, S. Ferrero, L.T. Ngo, Q. Chen, D.S. Humphrey, A.L. Shluger, G. Thornton, *Bonding of Methyl Phosphonate to TiO_2(110),* The Journal of Physical Chemistry C, 114 (2010), pp. 16983-16988, DOI: https://doi.org/10.1021/jp1018923.

[156] E.S. Skibinski, W.J.I. DeBenedetti, M.A. Hines, *Solution Deposition of Phenylphosphinic Acid Leads to Highly Ordered, Covalently Bound Monolayers on TiO_2(110) Without Annealing,* The Journal of Physical Chemistry C, 121 (2017), pp. 14213-14221, DOI: https://doi.org/10.1021/acs.jpcc.7b04167.

[157] R. Luschtinetz, J. Frenzel, T. Milek, G. Seifert, *Adsorption of Phosphonic Acid at the TiO_2 Anatase (101) and Rutile (110) Surfaces,* The Journal of Physical Chemistry C, 113 (2009), pp. 5730-5740, DOI: https://doi.org/10.1021/jp8110343.

[158] B. Lindberg, A. Berndtsson, R. Nilsson, R. Nyholm, O. Exner, L. Fernholt, G. Gundersen, C.J. Nielsen, B.N. Cyvin, S.J. Cyvin, *An ESCA Investigation of Ambident Ions and Tautomerism. N-Cyanobenzamides and Benzohydroxamic Acids,* Acta Chemica Scandinavica, 32a (1978), pp. 353–359, DOI: https://doi.org/10.3891/acta.chem.scand.32a-0353.

[159] G. Beamson, D. Briggs, *High Resolution XPS of Organic Polymers: The Scienta ESCA300 Database* Journal of Chemical Education, 1993, ISBN: 0-471-93592-1.

[160] D. Briggs, G. Beamson, *Primary and secondary oxygen-induced C1s binding energy shifts in x-ray photoelectron spectroscopy of polymers,* Analytical Chemistry, 64 (1992), pp. 1729–1736, DOI: https://doi.org/10.1021/ac00039a018.

[161] U. Gelius, P.F. Hedén, J. Hedman, B.J. Lindberg, R. Manne, R. Nordberg, C. Nordling, K. Siegbahn, *Molecular Spectroscopy by Means of ESCA III. Carbon compounds,* Physica Scripta, 2 (1970), pp. 70–80, DOI: https://doi.org/10.1088/0031-8949/2/1-2/014.

[162] O.O. Kapitanova, E.Y. Kataev, D.Y. Usachov, A.P. Sirotina, A.I. Belova, H. Sezen, M. Amati, M. Al-Hada, L. Gregoratti, A. Barinov, H.D. Cho, T.W. Kang, G.N. Panin, D. Vyalikh, D.M. Itkis, L.V. Yashina, *Laterally Selective Oxidation of Large-Scale Graphene with Atomic Oxygen,* The Journal of Physical Chemistry C, 121 (2017), pp. 27915–27922, DOI: https://doi.org/10.1021/acs.jpcc.7b07840.

[163] A. Schöll, Y. Zou, M. Jung, T. Schmidt, R. Fink, E. Umbach, *Line shapes and satellites in high-resolution x-ray photoelectron spectra of large pi-conjugated organic molecules,* The Journal of Chemical Physics, 121 (2004), pp. 10260–10267, DOI: https://doi.org/10.1063/1.1807812.

[164] M. Batzill, E.H. Morales, U. Diebold, *Surface studies of nitrogen implanted TiO_2,* Chemical Physics, 339 (2007), pp. 36-43, DOI: https://doi.org/10.1016/j.chemphys.2007.07.037.

[165] D. Jaeger, J. Patscheider, *A complete and self-consistent evaluation of XPS spectra of TiN,* Journal of Electron Spectroscopy and Related Phenomena, 185 (2012), pp. 523–534, DOI: https://doi.org/10.1016/j.elspec.2012.10.011.

9. Description of the Contribution to P1 - P4

[P1] **Controlling the Self-Metalation Rate of Tetraphenylporphyrins on Cu(111) via Cyano Functionalization.** M. Lepper, J. Köbl, L. Zhang, M. Meusel, H. Hölzel, D. Lungerich, N. Jux, A. de Siervo, B. Meyer, H.-P. Steinrück, H. Marbach**,** In: *Angew. Chem. Int. Ed.* **2018**, *57*, 10074. DOI: 10.1002/anie.201803601.

Contribution: data acquisition of the STM data was done by M. Lepper, J. Köbl, M. Meusel and L. Zhang, data evaluation and interpretation was done by M. Lepper and J. Köbl with support of the co-authors.

[P2] **Hungry Porphyrins: Protonation and Self-Metalation of Tetraphenylporphyrin on TiO_2(110) – (1 × 1).** J. Köbl, T. Wang, C. Wang, M. Drost, F. Tu, Q. Xu, H. Ju, D. Wechsler, M. Franke, H. Pan, H. Marbach, H.-P. Steinrück, J. Zhu, O. Lytken, In: *ChemistrySelect* **2016**, *1*, 6103. DOI: 10.1002/slct.201601398.

Contribution: data acquisition of all XPS data was done by J. Köbl with the support of Wang Tao during the Master's Thesis of Julia Köbl, the STM data was acquired and evaluated by M. Drost and F. Tu., additional measurements, further data analysis and interpretation, preparation of figures, and writing of the manuscript was done by J. Köbl with support of the co-authors during the doctoral thesis of J. Köbl.

[P3] **Adsorption of phenylphosphonic acid on rutile TiO_2(110).** J. Köbl, D. Wechsler, E. Y. Kataev, F. J. Williams, N. Tsud, S. Franchi, H.-P. Steinrück, O. Lytken, In: Surface Science, **2020,** 698, 121612. DOI: 10.1016/j.susc.2020.121612.

Contribution: data acquisition was done by J. Köbl, D. Wechsler, E. Y. Kataev and O. Lytken at the synchrotron facility Elettra-Sincrotrone Trieste with support of the beamline scientists N. Tsud and S. Franchi, data evaluation and interpretation, preparation of figures, and writing of the manuscript was done by J. Köbl based on discussions with the co-authors .

[P4] **Benzohydroxamic Acid on Rutile TiO_2(110) - (1 x 1)– A Comparison of Ultrahigh-Vacuum Evaporation with Deposition from Solution**. J. Köbl, C.C. Fernández, L.-M. Augustin, E.Y. Kataev, S. Franchi, N. Tsud, C. Pistonesi, M.E. Pronsato, N. Jux, O. Lytken, F.J. Williams, H.-P. Steinrück, Benzohydroxamic Acid on Rutile TiO_2(110)-(1×1)– A Comparison of Ultrahigh-Vacuum Evaporation with Deposition from Solution, In: Surface Science, **2021**, 121955. DOI: 10.1016/j.susc.2021.121955.

Contribution: data acquisition of the vacuum-deposited molecules on TiO_2(110) was done by J. Köbl, L.-M- Augustine, E. Y. Kataev and O. Lytken at the synchrotron facility Elettra-Sincrotrone Trieste with support of the beamline scientists N. Tsud and S. Franchi, data acquisition of the XP spectra of the powder samples were done by J. Köbl at PHI Quantera II Scanning XPS Microprobe of the Helmholtz Institute Erlangen-Nürnberg (HI ERN), data analysis and interpretation, preparation of figures 1, 2, 3, 5, 6 and 7 was done by J. Köbl with support of C. C. Fernández, writing of the manuscript was done by J. Köbl with support of C. C. Fernández, E. Y. Kataev, N. Jux, O. Lytken and H.-P. Steinrück; the manuscript part related to the results and discussion of the DFT calculations were written by C. Pistonesi, M. E. Pronsato and F. J. Williams.

10. Appendix P1 - P4

[P1] M. Lepper, **J. Köbl**, L. Zhang, M. Meusel, H. Hölzel, D. Lungerich, N. Jux, A. de Siervo, B. Meyer, H.-P. Steinrück, H. Marbach, Controlling the Self-Metalation Rate of Tetraphenylporphyrins on Cu(111) via Cyano Functionalization, In: Angew. Chem. Int. Ed. 2018, 57, 10074. DOI: 10.1002/anie.201803601.

[P2] **J. Köbl**, T. Wang, C. Wang, M. Drost, F. Tu, Q. Xu, H. Ju, D. Wechsler, M. Franke, H. Pan, H. Marbach, H.-P. Steinrück, J. Zhu, O. Lytken, Hungry Porphyrins: Protonation and Self-Metalation of Tetraphenylporphyrin on TiO_2(110) - 1 × 1, In: ChemistrySelect, 2016, 1, 6103-6105. DOI: 10.1002/slct.201601398.

[P3] **J. Köbl**, D. Wechsler, E.Y. Kataev, F.J. Williams, N. Tsud, S. Franchi, H.-P. Steinrück, O. Lytken, Adsorption of phenylphosphonic acid on rutile TiO_2(110), In: Surface Science, 2020, 698, 121612. DOI: 10.1016/j.susc.2020.121612.

J. Köbl, D. Wechsler, E.Y. Kataev, F.J. Williams, N. Tsud, S. Franchi, H.-P. Steinrück, O. Lytken, CORRIGENDUM: Adsorption of phenylphosphonic acid on rutile TiO_2(110), In: Surface Science, 2022, 717, 122004. DOI: 10.1016/j.susc.2021.122004.

[P4] **J. Köbl**, C.C. Fernández, L.-M. Augustin, E.Y. Kataev, S. Franchi, N. Tsud, C. Pistonesi, M.E. Pronsato, N. Jux, O. Lytken, F.J. Williams, H.-P. Steinrück, Benzohydroxamic Acid on Rutile TiO_2(110) - (1 × 1)– A Comparison of Ultrahigh-Vacuum Evaporation with Deposition from Solution, Surface Science, 2021, 716, 121955. DOI: 10.1016/j.susc.2021.121955.